PFC/RR-82-23 DOE/ET-51013-50

FED-R2: CONCEPT AND MAGNET DESIGN OF A LOW COST FED

J.E.C. Williams, H. Becker, D. Blackfield
E. Bobrov, L. Bromberg, D.R. Cohn,
N. Diatchenko and R. LeClaire

M.I.T. Plasma Fusion Center
Cambridge, MA 02139

December 1982

Table of Contents

LIST OF FIGURES

LIST OF TABLES

1.1 INTRODUCTION AND SUMMARY

In this report we describe the use of high performance resistive magnet technology to develop a design for a compact, low cost version of the fusion engineering device FED. We refer to this design as FED-R2, for FED-resistive magnet design 2 to distinguish it from the larger resistive magnet design for FED which uses demountable coils (FED-R1) [1].

The main objectives of FED-R2 are:

- To demonstrate reliable, quasi-steady state (long pulse, high duty factor) operation with $Q_p \approx 5$.
- To demonstrate $Q_p > 5$ operation for a limited number of pulses.
- To provide high neutron flux for irradiation of nuclear test modules with a total area greater than 20m^2.
- To utilize steady-state RF current drive if this option appears promising.

Based upon the costing codes at the Fusion Engineering Design Center and upon TFTR costs, the estimated direct costs of FED-R2 would be on the range 380-460M, a factor of about 2 below that of the baseline FED design.

1.2 TF Magnet Design

The toroidal field (TF) magnet uses Bitter plates which are water cooled [2]. Advantages of Bitter plate type construction include:

Stiffness of the magnets against both in-plane and out-of-plane loads.

- Longer insulation life under irradiation (planar insulators can be used).
- Minimization of resistive power requirements due to large conductor volume.

20 cm of inboard shielding are used to reduce the neutron flux to the magnet to levels on the order of 10^{13}nt/cm^2 sec. With an expected insulation lifetime of $\sim 10^{20}$nt/cm^2, 10^7 seconds of operation at 1MW/m^2 should be possible [3].

1.3 Major Parameters and Machine Performance

The major parameters of FED-R2 are given in Table 1. Two levels of performance are given. Nominal operation provides a neutral wall loading of 1MW/m^2. High power operation could provide a wall loading of 4MW/m^2 and gives a margin of safety in achieving ignition. According to the INTOR scaling law the margin of ignition (margin of ignition = $(n\tau_E)_{INTOR}/(n\tau_E)_{IGNITION}$) at T = 15 keV is 0.5 (corresponding to $Q_p = 5$) for nominal operation and 2 for high power operation.

The TF magnet power requirement for nominal operation is 120 MW and the equilibrium field (EF) magnet requirement is about 30 MW. Assuming \$0.1/kW-hr for electricity costs, the cost for 150 MW of power required for 3×10^7 s (1×10^7 s of DT plus 2×10^7 s of hydrogen nominal operation) is about \$150 M (\$15M per year for 10 years operation with a duty cylce of 10%).

For nominal operation the equivalent (von Mises) membrane stress in the TF magnet is 100 MPa. The RF heating power is 30 MW.

1.4 Nuclear Testing and Maintenance

FED-R2 would accommodate approximately 22 m^2 of total area of nuclear test modules. After heating and pumping requirements are taken into account, approximately 8 m^2 of port area is available for test modules which can be directly removed from the tokamak. In addition, approximately 14 m^2 of test module area could be accessed by translating the modules toroidally and then removing them through a port.

Figure 1.1 shows a side view of FED-R2. Figure 1.2 shows an isometric view of FED-R2. There are 16 ports, each with a clear area of 1m high $\times$ 0.6m wide. The port construction is illustrated in Figure 1.1 and 1.2. The saddle type ports are formed by extending the port plates in major radius and then cranking them toroidally, without disturbing the turns adjacent to the ports. There are 16 modules, separated by closure flanges that extend from the vacuum boundary.

The FED-R2 tokamak is completely modularized to facilitate assembly and maintenance. There are sixteen sectors consisting of TF magnet, blanket and shield and first wall.

1.5 Key Design Issues

Key issues in the proposed design include the following:

(1) Maintenance - In the modular design considered here the vacuum joint in the plasma vessel is either accessible on the outside of the TF coils or is a weldless seal. This allows easy removal of a small section of TF magnet and nuclear island for maintenance since no girth bands obstruct the outside of the TF coil, unlike Alcator [4] and Zephyr [5].

(2) Test Module Accessibility - The blanket modules are accessible through 13 ports in the outside of the TF coil. Three ports are dedicated to pumping , heating and fueling of the plasma.

(3) Life - The life of the magnet system is essentially determined by that of the TF coils in the throat region. The design of the TF coil is based on both static and fatigue properties of cold worked copper plate and on the survivability of polyimide-glass insulators (an organic insulator with good resistance to radiation damage) throughout the magnet.

(4) Support of Magnetic Forces - Because girth bands are absent from the TF coil, transmission of shear between copper conducting plates and steel reinforcement is by insulated keys, instead of bonding and friction as in designs of other systems [4,5]. Bonding of copper and steel to insulation is used in the present design only for purposes of assembly.

(5) Cooling - to minimize erosion and corrosion in the TF magnet the water flows in tubes embedded in the faces of the plates. The cooling channels are distributed so as to equalize average temperature rise in the plates and to minimize "hot spot" temperature rise.

(6) Fabrication - In the throat of the TF coil 1/4 hard cold rolled copper acts alone to provide the required strength. Because of limitations in the size of cold-rolled copper plate, each TF coil plate requires several weldments. These have been designed to circumvent the strength loss at the weld. The keys which transmit shear forces between copper and steel are of hard copper coated with polyimide-glass insulators. The assembly of the plates, insulators and wedges of a module uses epoxy resin filled with chopped glass fibers to ensure integrity of the module.

REFERENCES

[1] JASSBY, D.L. and Fusion Design Center, Oak Ridge.

[2] BITTER, F., "Water Cooled Magnets", in *High Magnetic Fields, Proceedings fo the International Conference on High Magnetic Fields (1961)*, M.I.T. Press, Cambridge, Ma (1962).

[3] BECKER, H., M.I.T. Plasma Fusion Cener, private communication.

[4] WEGGEL, C., HAMBURGER, W., MONTGOMERY, B. and PIERCE, N., "The ALCATOR-C Magnetic Coil Systems", in *Proceedings of the 6th Symposium on Engineering Problems of Fusion Research*, 1975, p.54.

[5] WILLIAMS, J.E.C., BECKER, H.D., BOBROV, E.S., BROMBERG, L., COHN, D.R., DAVIN, J.M. and EREZ, E., "Conceptual Design of a Bitter Magnet Toroidal Field System for the ZEPHYR Ignition Test Reactor", MIT Plasma Fusion Center Report PFC/RR-81-24(1981)

[6] COHN D.R., BROMBERG, L., WILLIAMS, J.E.C., BECKER, H., LECLAIRE, R. and YANG, T., "Near Term Tokamak Reactor Designs with High Performance Resistive Magnets," presented at the IAEA Third Technical Committee and Workshop on Fusion Reactor Design and Technology, Tokyo, Japan, October (1981), MIT Plasma Fusion Center, Report PFC/CP-81-29.

TABLE 1.1

Major Parameters of FED-R2

major radius (m)	2.64	
minor radius (m)	0.63	
average beta: (q = 2.5, elongation = 1.5)	0.047	
weight of TF magnet (tonnes)	1600	
weight of module (tonnes)	100	
inboard shield thickness (m)	0.2	
outboard blanket thickness (m)	0.4	
	Nominal Op.	**High Power Op.**
mag. field on axis	5.1	7.2
wall loading (MW/m^2)	1	4
fusion power (MW)	110	440
margin of ignition (INTOR scaling)	0.5	2
average density ($10^{20}m^{-3}$)	2.0	4.0
plasma current (MA)	3.3	4.6
TFplus EF magnet power	150	300

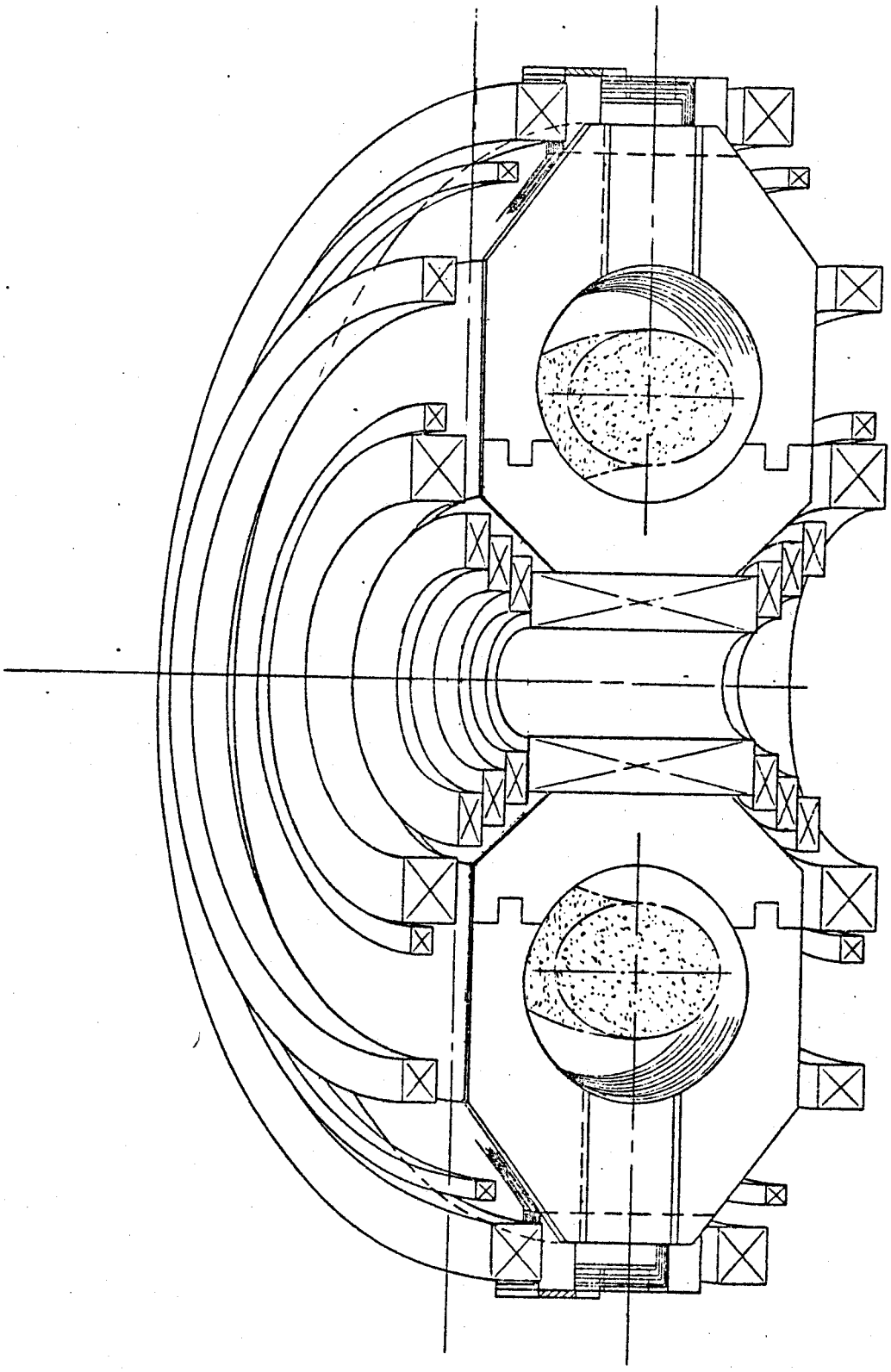

Figure 1.1Elevation View of FED-R2

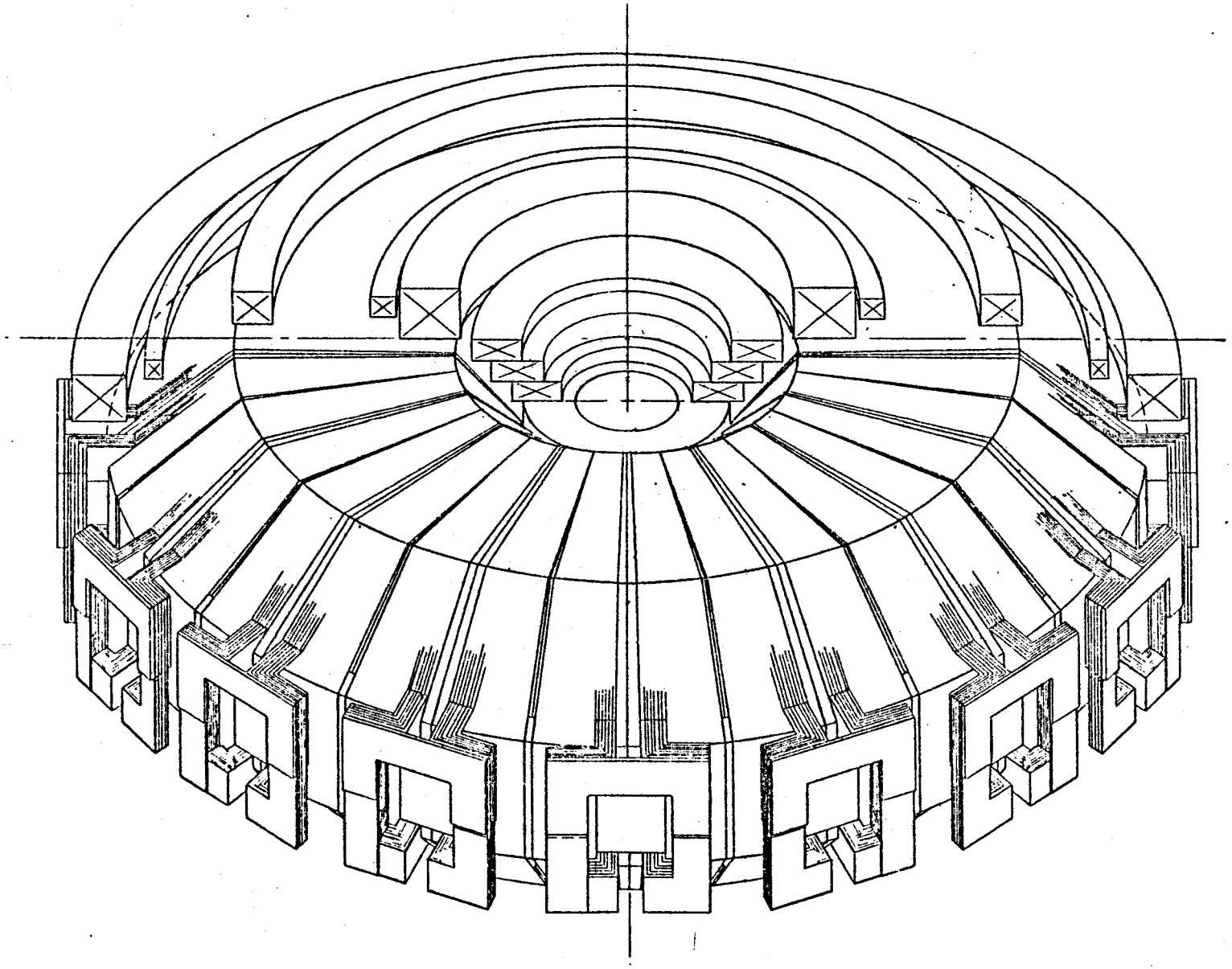

Figure1.2 Isometric View of FED-R2

2.1 PARAMETRIC ANALYSIS - CHOICE OF ILLUSTRATIVE DESIGN

In this section, parametric scans are performed to illustrate the different tradeoffs.

FED-R2 is a neutron-applications reactor. Its main goal is that of producing copious amounts of neutrons for sufficiently long periods of time to allow the testing of certain nuclear systems. A further goal, for short pulses and for a limited number of pulses, is to obtain plasma parameters close to those of future test and commercial reactors, as presently envisaged. In the parametric scans, we have chosen the neutron wall loading to be $1 MW/m^2$ for FED-R2 normal (or base case) operation, and $4 MW/m^2$ for the high performance operation.

The high performance operation has a burn pulse length of 100 seconds, limited by the OH transformer. The pulse length in the base case has also been assumed to be 100 seconds, although it can be longer if the stresses in the OH transformer are increased to the levels of the high performance case, which has larger OH flux requirements.

The peak von Mises stresses in the throat of the magnet in the high performance case are $\sigma_{TF} = 196$ MPa. The stresses in the ohmic heating central transformer are roughly equal to the stresses in the throat of the TF magnet. For the high performance operation the numbers of pulses of the ohmic transformer and of the toroidal field coil are the same. For the base case operation, the number of pulses in the ohmic transformer is much larger than that of the toroidal field. However, in the base case the stresses are smaller by a factor of 2 and fatigue through pulsed operation will not then lead to failure (in this case the failure mechanism is related to the lifetime under neutron irradiation of the insulation in the throat of the magnet).

The plasma elongation has been chosen to be $\kappa = b/a = 1.5$ and the plasma safety factor $q = 2.5$ at the plasma edge and $q = 0.9 - 1$ at the plasma center. For these conditions, it is assumed that the value of the average toroidal beta (β_T) is determined by

$$\beta_T = \frac{0.2}{A}$$

where $A = R/a$ is the plasma aspect ratio and where β_T is the ratio of the average plasma pressure to the magnetic field pressure,

$$\beta_T = \frac{nkT}{B^2/2\mu_o}$$

and B is the toroidal field on the plasma axis. The plasma triangularity resulting from the poloidal field system is $0.05 \leq \delta \leq 0.2$, and is determined in the section for the equilibrium field system of the illustrative design (section 3.3.3).

The parameters of the equilibrium field system are calculated using the method described in section 3.3. The same parameters that optimize the vertical field system (section 3.3.2) are assumed. In this section it is assumed that the OH transformer is double swung (the magnetic field in the OH transformer is partially reversed).

The distance between the toroidal field coil and the plasma in the midplane in the throat of the magnet, δ_i is assumed to be $\delta_i = 0.40$ m. This allows for .20 m of high performance shielding in the inboard of the magnet, plus 0.10 m for first wall and 0.10 m for the plasma scrape-off region. On the outboard side of the plasma, the distance between the plasma and the toroidal field coil is $\delta_o = 0.6$ m. The larger distance allows for ~0.30 - 0.40 m of blanket/shield test modules located between the toroidal field coil and the first wall. The space available for testing is described later in section 3.2.

The lifetime of the machine is determined by the survivability of the insulation in the inboard side of the magnet. The lifetime of the magnet is discussed further in section 6.

The assumptions in the parametric code are shown in Table 2.1. Table 2.2 shows the results of the parametric scan vs. aspect ratio. The margin of ignition, MI, is defined as the ratio between the plasma $n\tau_E$ product and the $(n\tau_E)$ product required for ignition at an average temperature of 7.5 keV,

$$MI = \frac{(n\tau_E)_{\text{plasma}}}{(n\tau_E)_{\text{ignition}}}$$

It is assumed that the energy confinement for the electrons is given by the empirical scaling law

$$\tau_{E_e} = 3.8 \times 10^{-19} n a^2$$

where n is the average plasma density in cm^{-3}, a is the minor radius in cm and τ_{E_e} is in seconds. In Table 2.2, I is the plasma current, P_f is the total fusion power, W_{TF} is the weight of the TF coil, P_{TF} is the resistive power of the TF coil, E_{TF} is the stored energy in the EF coil, P_{EF} is the resistive power of the EF coils, E_{EF} is the stored energy in the EF coils, MA_{EF} is the Ampere turns of the EF coils and W_{EF} is the weight of the EF coils. τ is the shear stresses in the outer leg of the TF coil that resist the torsion of the Bitter magnet due to the interaction between the poloidal field and the current in the TF coil.

The margin of ignition is then

$$MI = \frac{(n\tau_E)_{\text{empirical}}}{(n\tau_E)_{\text{ignition}}} \sim (\beta_T a B^2)^2$$

at fixed temperature. From transport calculations it has been determined that the value of $(\beta_T a B^2)^2$ at ignition is $(\beta_T a B^2)^2_{ign} = 1.3\ \text{m}^2\text{T}^4$ for parabolic density and temperature profiles. Therefore,

$$MI = \frac{(\beta_T a B^2)^2}{(\beta_T a B^2)^2_{\text{ignition}}} = \frac{(\beta_T a B^2)^2}{1.3}$$

where a is in m and B_T is in T. MI is a measure of how close the plasma is to ignition according to the empirical scaling law or, if $MI > 1$, of the margin of safety to achieve ignition.

From Table 2.2, the margin of ignition, for a fixed wall loading of $P_{wall} = 4$ MW/m^2, is decreasing with increasing aspect ratio A. The reason for this is that for the empirical scaling law, the wall loading is determined by

$$P_{wall} \sim \frac{n^2 R a^2}{Ra} \sim \frac{n^2 a^2}{a} \sim \frac{(n\tau)_{emp}}{a} \sim \frac{MI}{a}$$

where R is the plasma major radius. Therefore, for smaller minor radius a, (larger aspect ratio), the margin of ignition MI, has decreased. The fusion power decreases with increasing aspect ratio, as

$$P_f \sim n^2 R a^2 \sim (MI)R$$

and the major radius R remains approximately constant while MI decreases.

Figure 2.1 shows the margin of safety MI, the plasma current I, the magnetic field on axis B, the plasma major radius R and the fusion power P_f as functions of the aspect ratio. The plasma major radius remains approximately constant because of the constraint on the stresses in the throat of the magnet: as the aspect ratio increases, the throat cross sectional area increases sufficiently to balance the increased loads due to the increased magnetic field necessary to keep P_{wall} constant.

Figure 2.2 shows the parameters of the toroidal field coil P_{TF} (resistive power), E_{TF} (stored energy in the toroidal coil), and W_{TF} (weight of toroidal field coil) as a function of the aspect ratio. For $A > 4$, the resistive power and the weight of the toroidal field coil are relatively constant. The stored energy in the toroidal field coil increases substantially with increasing aspect ratio.

Figure 2.3 shows the parameters of the equilibrium field system E_{EF} (stored energy), P_{EF} (resistive power), MA (Ampere turns) and W_{EF} (weight of the coils of the EF system) as a function of the aspect ratio.

The parameters of the vertical system are relatively flat with aspect ratio, with a broad minimum around $A = 4.5$.

The nuclear characteristics of the machine designs, shown in Table 2.2 and Figures 2.1-2.3 are approximately constant, as the neutron wall loading and the radial builds of the shield and/or blankets have been kept fixed.

For the illustrative design, the case with aspect ratio $A \approx 4.2$ has been chosen. The optimum is broad, and the choice results in a compromise between increased energy in the toroidal field coil at the expense of decreased margin of ignition, MI.

There are some parameters that need to be determined. These are the full height of the magnet, h the radial thickness of the outer leg, t_{out}, and the ratio of steel reinforcement to copper in the outboard legs of the magnet, f.

Table 2.3 shows the parameters of the toroidal field magnet and equilibrium field systems as the height of the magnet is varied. It is assumed that the thickness of the outer leg is $t_{out} = 1.5$ m and the ratio of steel to copper is $f = 0.5$. As the height is increased, the bending stresses in the throat of the magnet decrease somewhat. More importantly, the resistive power of the TF magnet decreases at the expense of larger equilibrium field system requirements and larger stored energy in the toroidal field magnet. A compromise height is 3.7 m.

Table 2.4 shows the parameters of the toroidal and EF systems as the thickness of the outer leg, t_{out}, is varied. The stresses in the throat vary slightly. The weight of the magnet increases with $t_{\rm out}$, while the resistive power P_{TF} decreases slowly. As discussed in section 3.2 on ripple, the larger $t_{\rm out}$ the smaller the ripple. However, the ripple is already acceptable for $t_{\rm out} \geq 1.2$ m. $t_{\rm out}$ is then determined by the turn-to-turn connectors required. As discussed in section 3.1, $t_{\rm out}$ is ≈ 1.5 m.

Finally, the ratio f of steel to copper in the outboard region of the magnet needs to be determined. Table 2.5 shows the parameters of the TF magnet as f varies. For $f \leq 0.5$, the resistive power is a slowly decreasing function of f, as the contribution to the total resistive power from the outboard region of the magnet decreases with decreasing f.

Figure 2.4 shows the poloidal flux for the high performance case. Note that there is a significant triangularity due to the location of the shaping coil close to the main axis of the machine. Table 2.6 shows the plasma parameters derived from the equilibrium (described in section 3.3.2.).

Finally, Table 2.7 summarizes the main parameters of the TF and equilibrium system of the illustrative design.

TABLE 2.1

Constrains for the Parametric Scans

	base case	high performance
P_{wall} (MW/m^2)	1	4
$\beta_T A$	0.2	0.2
$\kappa = b/a$	1.5	1.5
burn pulse length (s)	100	100
$\sigma_{TF,vonmises}$ (MPa)	100	200
σ_{OH} (MPa)	100	200
δ_i (m)	0.40	0.40
δ_o (m)	0.6	0.6
number of pulses	3×10^5	10^3

TABLE 2.2

Parametric Scan vs Aspect Ratio

for $P_{wall} = 4$ MW/m^2

A	3.15	3.55	4.19	5.17	6.78
R (m)	3.15	2.84	2.64	2.59	2.71
a (m)	1.00	0.80	0.63	0.50	0.40
B (T)	5.54	6.21	7.16	8.43	10.2
I (MA)	7.67	6.04	4.57	3.39	2.44
$(\beta a B^2)^2$ m^{2}T^4	3.78	3.02	2.38	1.89	1.51
P_f (GW)	0.762	0.549	0.402	0.313	0.262
W_{TF} (ktonnes)	2.45	1.89	1.52	1.35	1.34
P_{TF} (MW)	238.	230.	238.	271.	352.
E_{TF} (GJ)	3.56	3.38	3.66	4.61	7.21
plate size	4.76×4.95	4.12× 4.65	3.61×4.35	3.25×4.24	3.03×4.24
τ (MPa)	17.9	20.16	23.8	29.4	38.5
E_{EF} (GJ)	0.501	0.39	0.334	0.347	0.536
P_{EF} (MW)	109.	91.3	81.4	82.6	108.
MA_{EF} (MA)	15.9	14.3	13.3	13.4	16.4
W_{EF} (tonnes)	238.	208.	178.	177.	216

TABLE 2.3

TF and EF System Parameters vs TF coil height, h

h (m)	3.36	3.61	3.95
P_{TF} (MW)	265.	238.	215.
E_{TF} (GJ)	3.3	3.6	4.1
W_{TF} (ktonnes)	1.38	1.52	1.71
τ (MPa)	22.1	23.8	26.4
E_{EF} (GJ)	0.297	0.334	0.387
P_{EF} (MW)	74.8	81.4	90.8
W_{EF} (tonnes)	168.	179.	193.
MA_{EF} (MA-turns)	12.2	13.3	14.8

TABLE 2.4

TF and EF System Parameters vs TF outer leg thickness, t_{out}

t_{out} (m)	1.0	1.5	1.75
P_{TF} (MW)	243.	238.	234.
E_{TF} (GJ)	3.4	3.6	3.8
W_{TF} (ktonnes)	1.26	1.52	1.69
τ (MPa)	35.7	23.8	20.4
E_{EF} (GJ)	299.	334.	357.
P_{EF} (MW)	77.1	81.4	84.2
W_{EF} (tonnes)	165.	179.	187.
MA_{EF} (MA-turns)	13.	13.3	13.5

TABLE 2.5

TF System Parameters vs Steel to Copper ratio

in the outboard leg of the TF Magnet, f

f	P_{TF} (MW)
1.0	266.
0.5	238.
0.33	227.
0.18	218.
0.11	214.

TABLE 2.6

Plasma Parameters Derived from Equilibrium

A	4.2
$\kappa = b/a$	1.49
δ (triangularity)	0.21
I_p (MA)	4.4
β_T (%)	4.79
q (axis)	0.92
q (edge)	2.7

Table 2.7

FED-R2 MAIN PLASMA PARAMETERS

FIELD ON AXIS (T)	7.1	5.1
MAJOR RADIUS (m)	2.64	2.64
MINOR RADIUS (m)	0.63	0.63
SCRAPE-OFF LAYER (m)	0.08	0.08
PLASMA ELONGATION (m)	1.5	1.5
PLASMA TRIANGULARITY	0.2	0.2
ASPECT RATIO	4.19	4.19
PLASMA TEMPERATURE (keV)	12	12
D-T ION DENSITY (m^{-3})	3.9×10^{20}	$2. \times 10^{20}$
SAFETY FACTOR	2.5	2.5
PLASMA CURRENT (MA)	4.6	3.4
EFFECTIVE CHARGE	1.2	1.2
PEAK-TO-AVERAGE RIPPLE AT EDGE (%)	0.8	0.8
TOTAL BETA (%)	4.8	4.8
D-T FUSION POWER (MW)	400	100
FUSION POWER GAIN	5-∞	5
NEUTRON WALL LOADING (MW/m^2)	4	1
PLASMA HEATING		
RF POWER (MW)	30	30
MODE	$2\omega_{cd}$	$2\,\omega_{ct}$
FREQUENCY (MHZ)	72	77
BULK SHIELD		
INBOARD SHIELD THICKNESS (m)	0.2	0.2
OUTBOARD BLANKET/SHIELD THICKNESS (m)	0.4	0.40

FED-R2 PARAMETERS (continued)

TF COIL		
PLATE SIZE (m^2)	3.7×4.35	3.7×4.35
NUMBER OF TF PLATES	384	384
NUMBER OF MODULES	16	16
MAXIMUM TF FIELD (T)	11.2	7.9
MAXIMUM CURRENT DENSITY (kA/cm^2)	1.61	1.14
RESISTIVE LOSSES (MW)	238	120
TF POWER (START-UP) (MW)	400	200
TF STORED ENERGY (MJ)	3.7	1.8
TF WEIGHT (ktonnes)	1.5	1.5
TOTAL CURRENT (MA)	95	67.3
COIL CURRENT (kA)	250	176
CHARGE TIME (s)	30	30
PF COILS		
EF COIL A-TURNS (MAT)	12.2	8.6
OH SOLENOID A-TURNS (MAT)	47	33
TOTAL PF A-TURNS (MAT)	60	42
V-s FROM EF COILS (Wb)	11.5	8.2
V-s FROM OH COILS (Wb)	34.4	24
TOTAL V-s FROM PF (Wb)	45.8	32
FIELD (OH SOLENOID) (T)	14.6	10.3
CURRENT RISE TIME (s)	1	1
CURRENT DENSITY (EF COILS) (ka/cm^2)	~1.2	0.85
CURRENT DENSITY (OH COILS) (ka/cm^2)	0.48	0.34
PEAK RESISTIVE POWER (EF COIL) (MW)	80	40
PEAK RESISTIVE POWER (OH COIL) (MW)	65	33

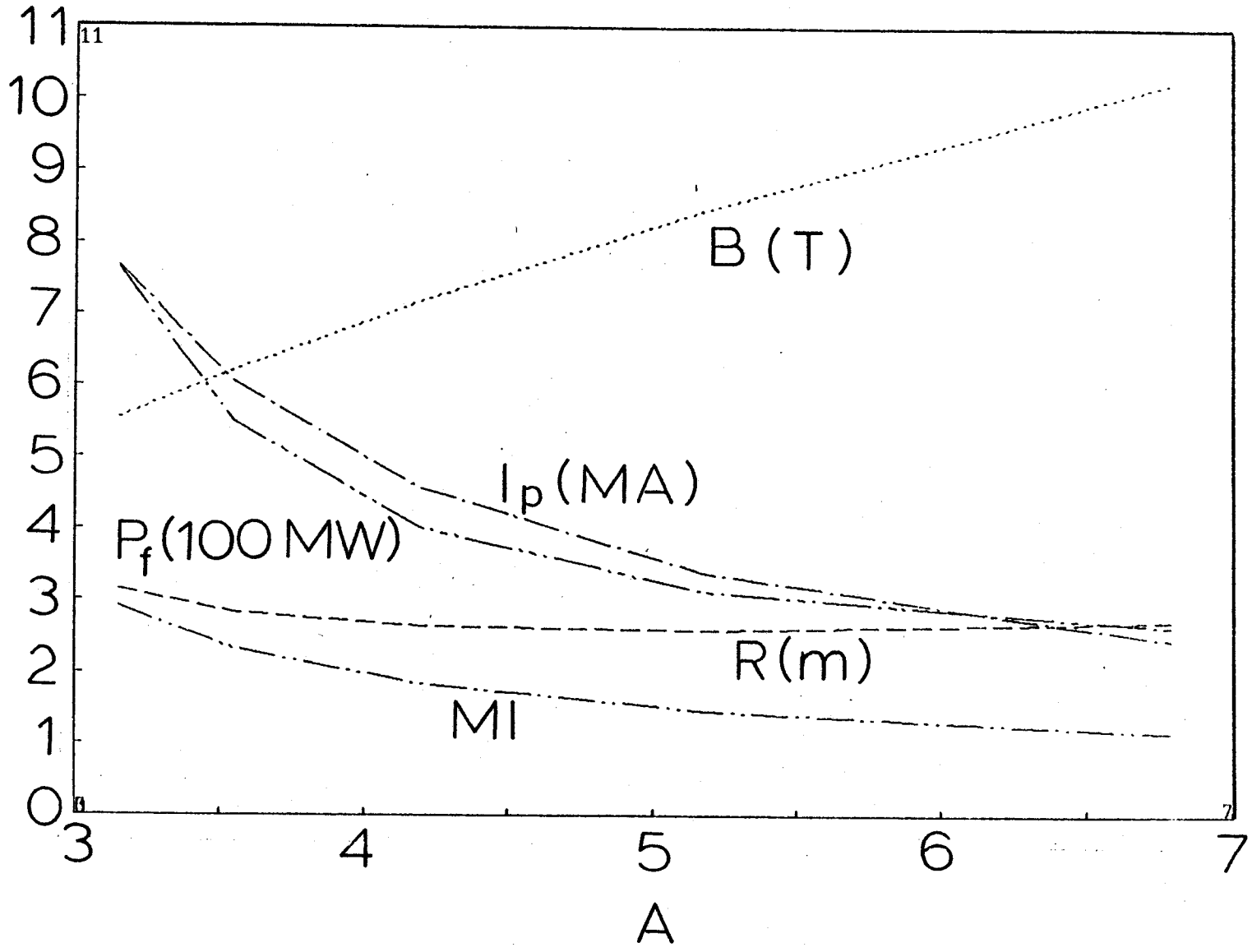

Figure 2.1 Plasma Characteristics vs Aspect Ratio for $P_{wall} = 4$ MW/m^2.

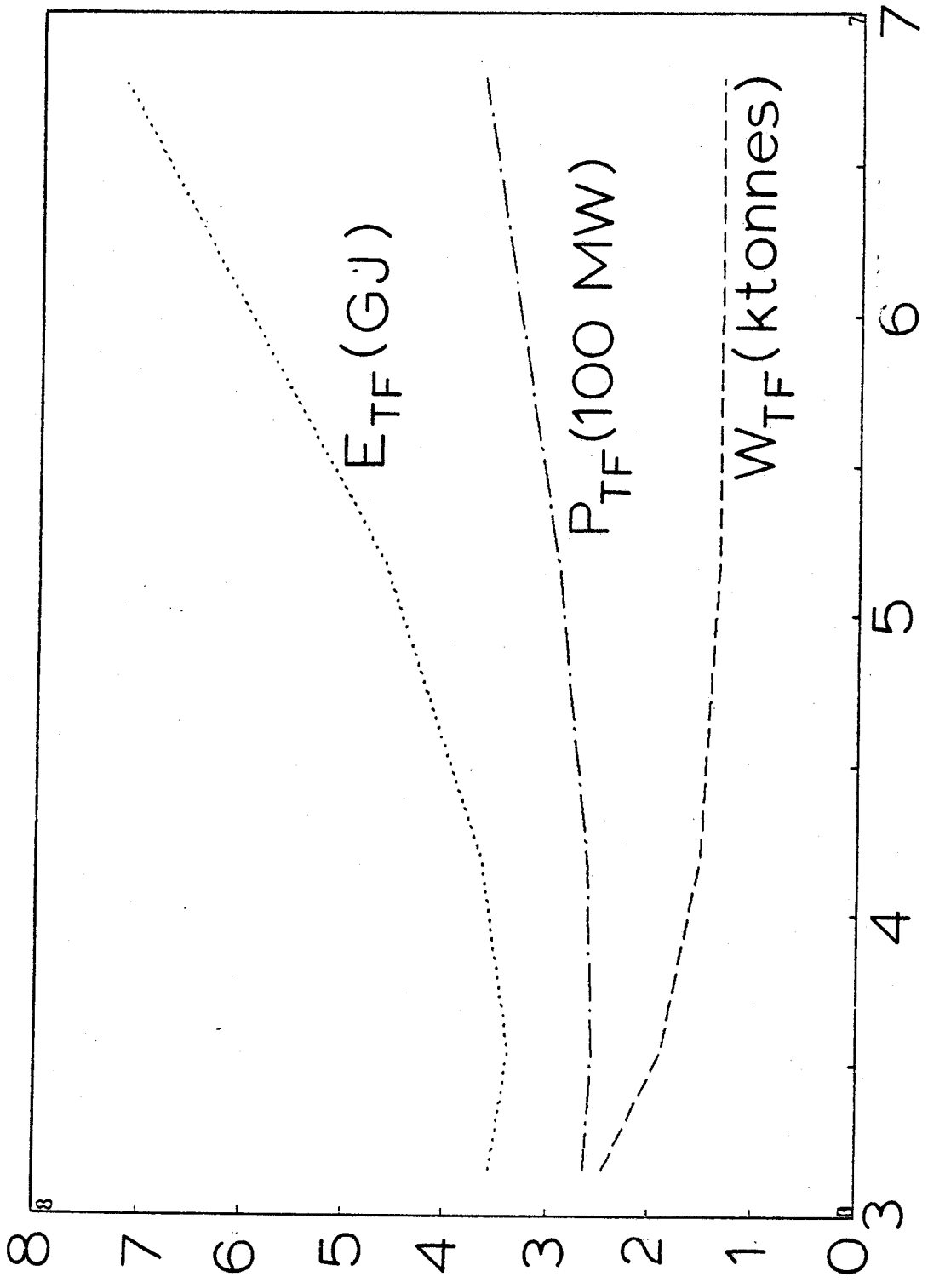

Figure 2.2 Characteristics of the TF System vs Aspect Ratio for $P_{wall} = 4$ MW/m^2.

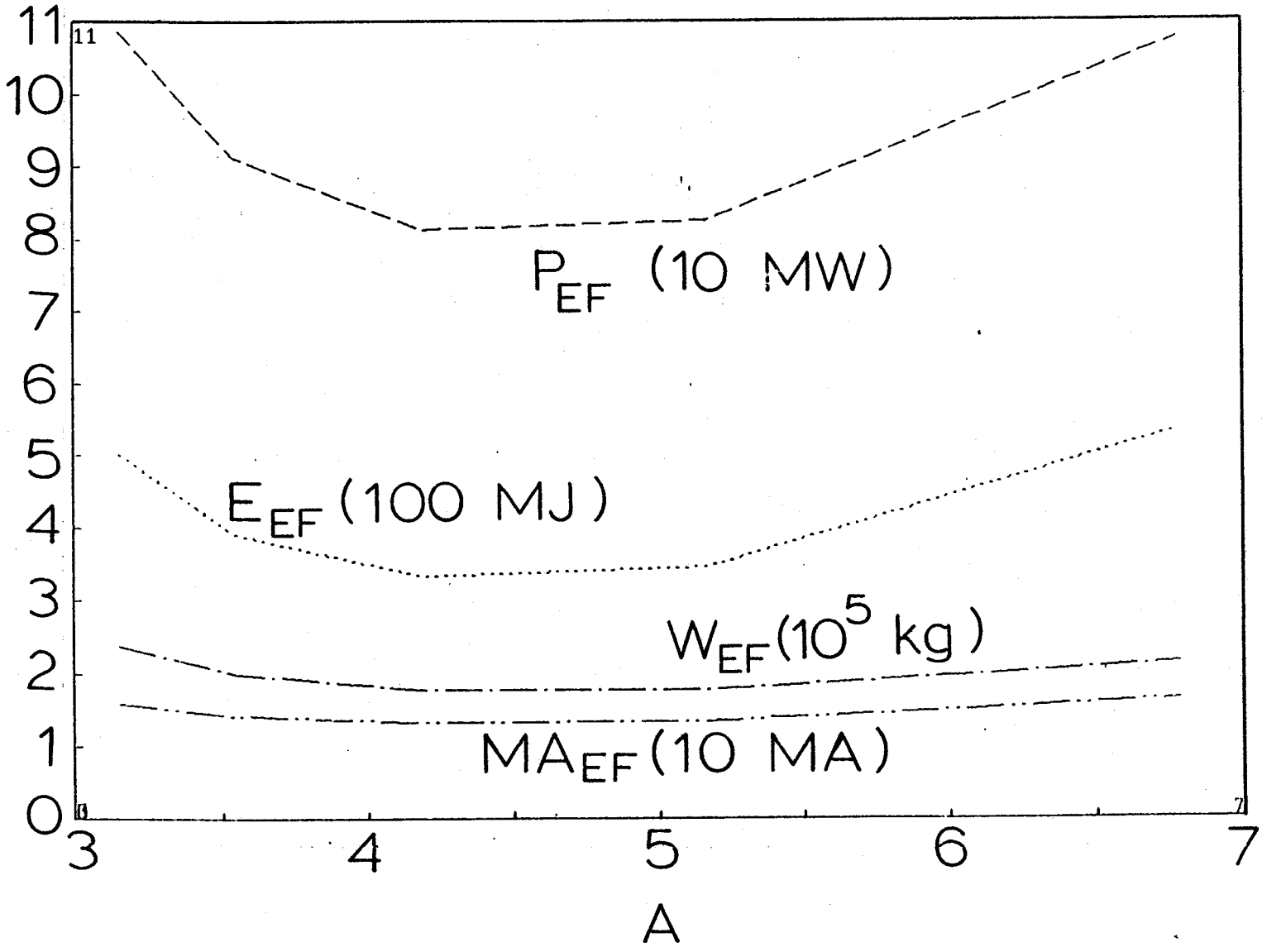

Figure 2.3 Characteristics of the EF System vs Aspect Ratio for $P_{wall} = 4\,\mathrm{MW/m^2}$.

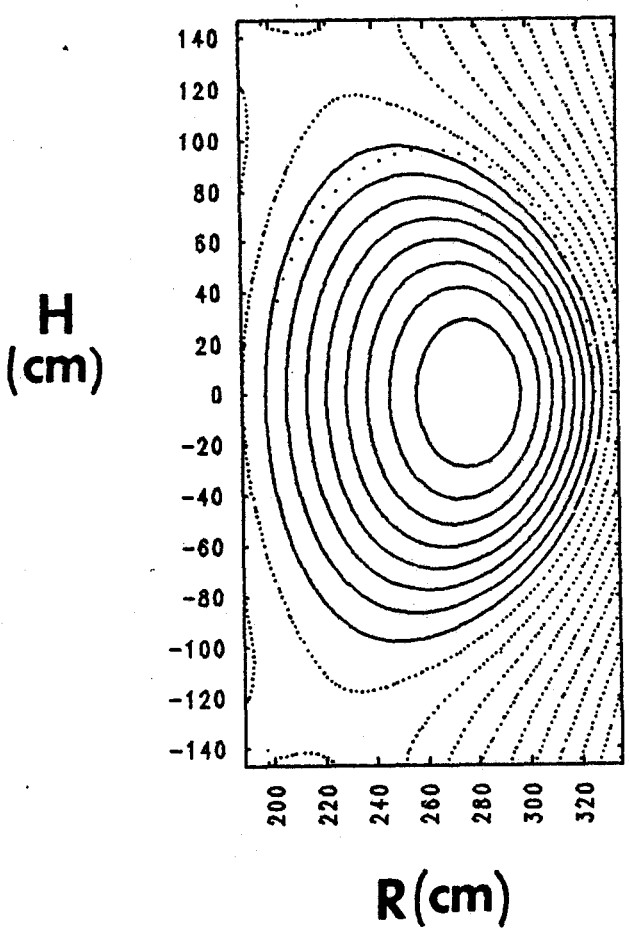

Figure 2.4 Plasma Poloidal Flux for the High Peformance Case

3. CONCEPTUAL DESIGN

3.1 Toroidal Field Coil

3.1.1 General Arrangement

The toroidal field coil is the key magnetic component in a tokamak device. It is subjected to the largest stresses (generally) and receives the highest radiation fluence of all magnetic components. Furthermore, the coil must accommodate ports for test modules, plasma heating and pumping without producing significant field ripple, and it must support the vacuum chamber against normal and disruption loads.

The Bitter plate magnet (as used for instance in Alcator A [1] and C [2] as proposed for TORFA [3], the AFTR series[4] and ZEPHYR [5]) satisfies a number of requirements better than does a wound coil. Bending from in-plane forces is resisted in the plane of greatest strength. Insulation selected for radiation resistance rather than flexibility can be used because all insulation is planar. Compared with a tape wound coil, lower power consumption results from the greater volume of conductor. Low ripple results from the absence of gaps between coils except locally around ports. No external structure is required to react twisting moments. The coil is constructed from a large number of identical units leading to the use of quantity manufacturing techniques.

A Bitter plate magnet has a few disadvantages compared to a wound coil. The operating current is high and the voltage is low. Access to the nuclear island is poorer. The principal parameters of the TF coil are given in Table 3.1.1.

3.1.2 The Basic Turn

The form of Bitter plate coil proposed for the present TF magnet is shown in Fig. 3.1.1. The basic unit of the magnet is a turn consisting of a copper plate, a steel reinforcing wedge, two insulating sheets and an interconnector.

The cold-rolled copper plate is fabricated from three pieces, as shown in Fig. 3.1.2. The throat section is machined to a taper with water cooling channels machined into one face. The upper and lower pieces are machined parallel-faced. These pieces are electron-beam welded (EBW) to the throat section. The upper and lower copper pieces are machined to receive keys which project either side of the plate (see Figure 3.1.3). Cooling channels are also machined in one face of the outer parts of the copper plate.

The complete copper plate is asymmetric because one face of the tapered throat section is aligned with one face of the parallel-faced pieces. The plane face of the complete plate mates to the flange at the end of each half module.

The steel reinforcement performs several functions. It transmits the vertical force in the outer limbs of the copper plates. It supports the keys that resist torsional and interplate stress. It provides support for the blanket and other components within the TF coil. In the center of each half module it furnishes extra turn spacing to improve the homogeneity of the toroidal field. The steel is flush with the copper at the outer edges but extends beyond it toward the plasma to support the blanket and first wall assembly.

The proposed insulation is polyimide-glass reinforcement in 1 mm thick sheets. Under essentially isostatic pressure the effective radiation life of such insulation is greater than 10^{11} rads, (approximately 10^{20} neutrons cm^{-2}) total fluence. Outside the throat region, radiation induced damage to the insulation diminishes radially away from the plasma.

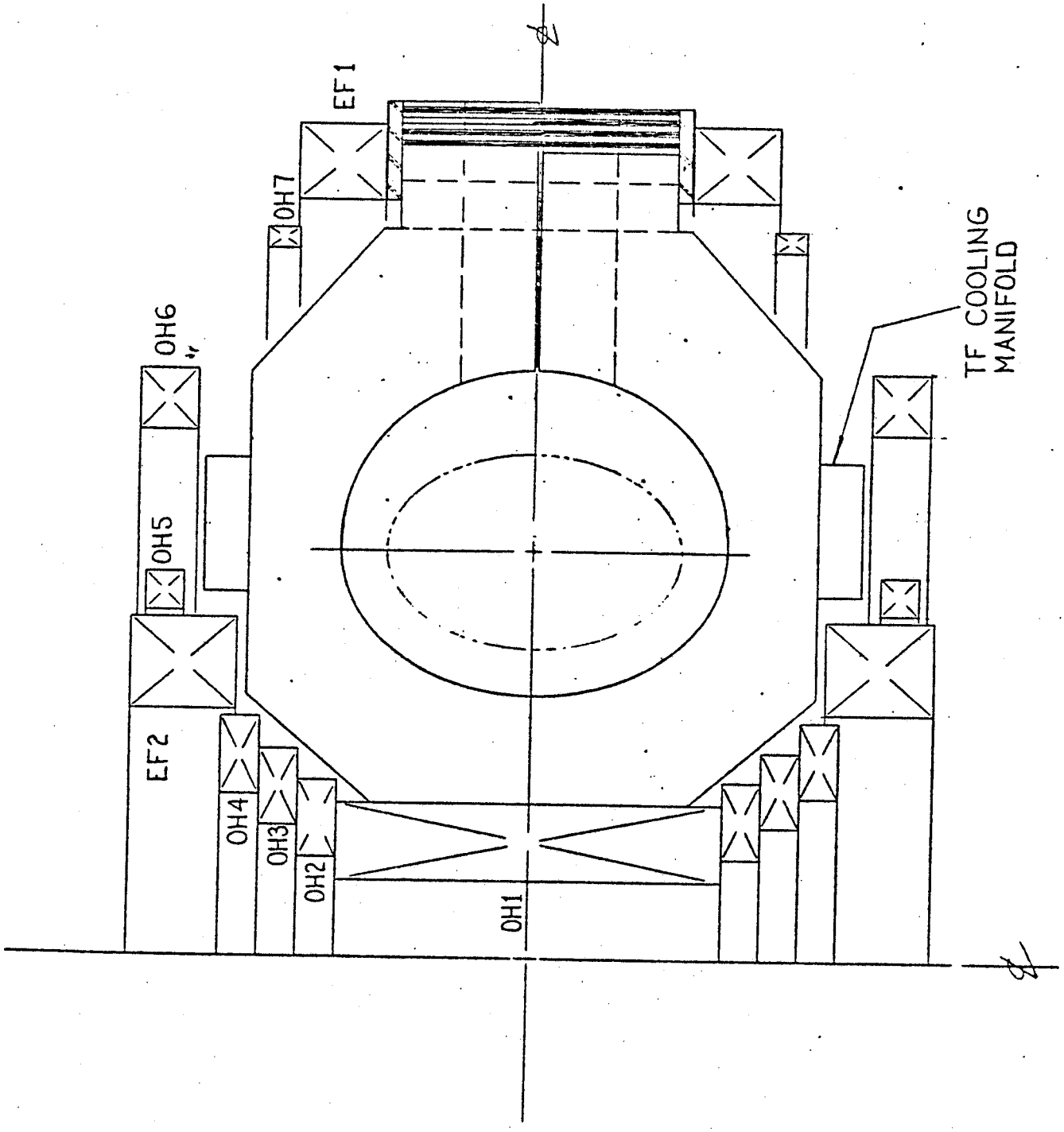

Figure 3.1.1 Basic Shapes of TF, EF and OH Coils

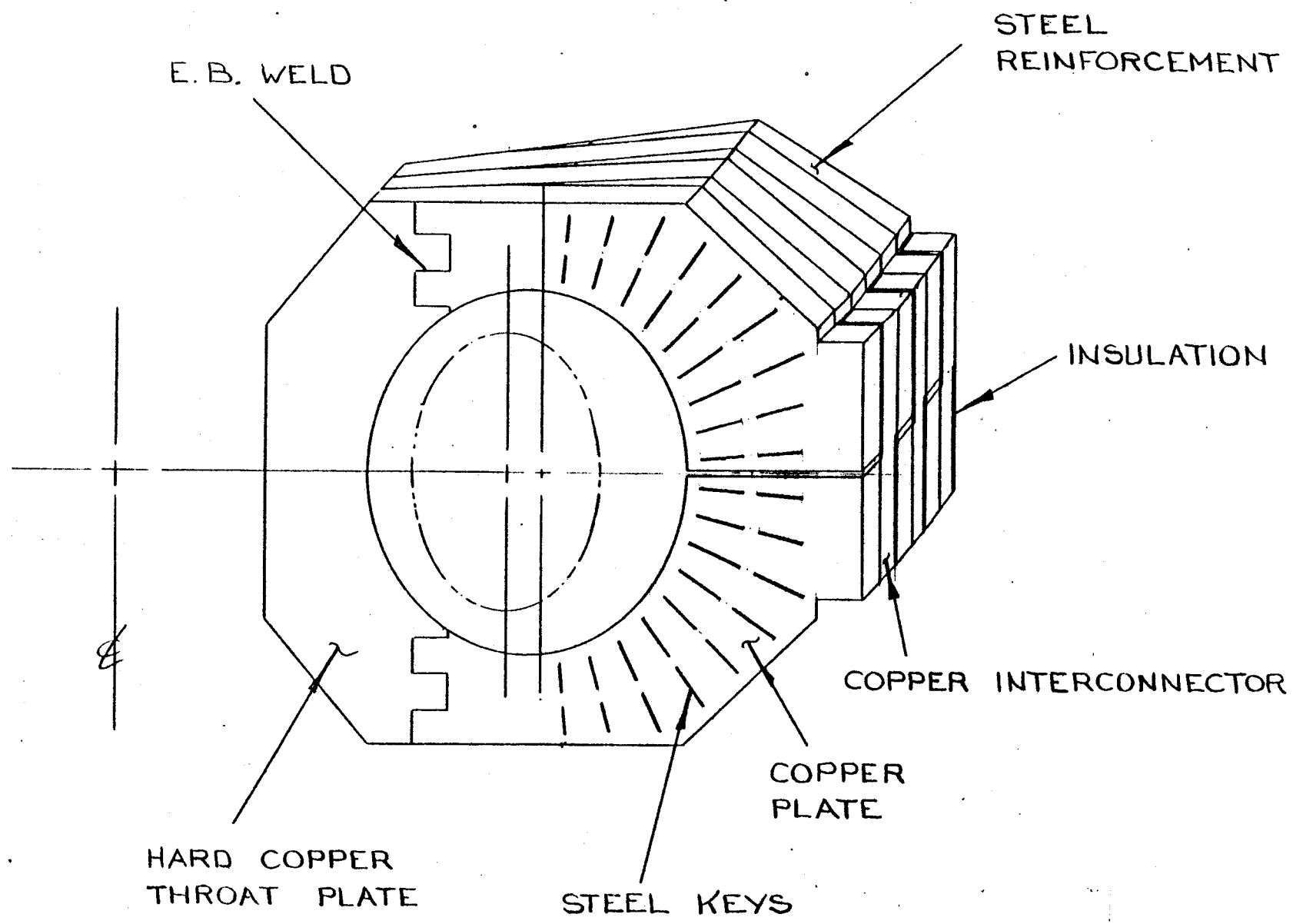

Figure 3.1.2 Three-Piece Copper Plate Construction Showing EB Weld Line to Reduce Stresses

Each turn has two sheets of insulation of shape as shown in Fig. 3.1.1. The keys are fully insulated from the steel which is therefore everywhere at ground potential. The insulation extends beyond the plates to ensure that shorts do not occur at exposed edges.

The corners of the plates are "cropped" as shown in Figs. 3.1.1 and 3.1.2. This has the advantage of allowing both the induction and vertical field coils to be placed close to the plasma. It increases the induction flux (or decreases the throat diameter) and decreases the poloidal currents.

3.1.3 Flanges

At the junction between modules there is a closure flange and mid-way between the closure flanges lies a port flange. The closure flange is in two halves which are welded around their outer periphery to close the vacuum vessel. The copper plates adjacent to the closure and port flanges are fully insulated from them but also keyed to them as to the steel reinforcement wedges (see Fig. 3.1.3). The two halves of each closure flange are keyed internally so as to transmit torsional shear. (If the port flange is fabricated in two halves then these also must be keyed internally.)

At the port opening the copper plates are folded to provide current paths around the sides of the ports. (Fig. 3.1.4). Figure 3.1.5 shows an elevation view of the machine with the port geometry and the relative location of the equilibrium field coils. At the ports the steel reinforcement is discontinuous, stopping just above and below the port opening. The vertical forces in the copper plates are transmitted to those truncated steel plates as elsewhere. Here, however, the steel must be vertically constrained by different methods because it is discontinuous. The vertical loads are transmitted by shear through adjacent copper and steel via the keys until the accumulated load is taken by unbroken steel reinforcement. This produces a high stress in the reinforce-

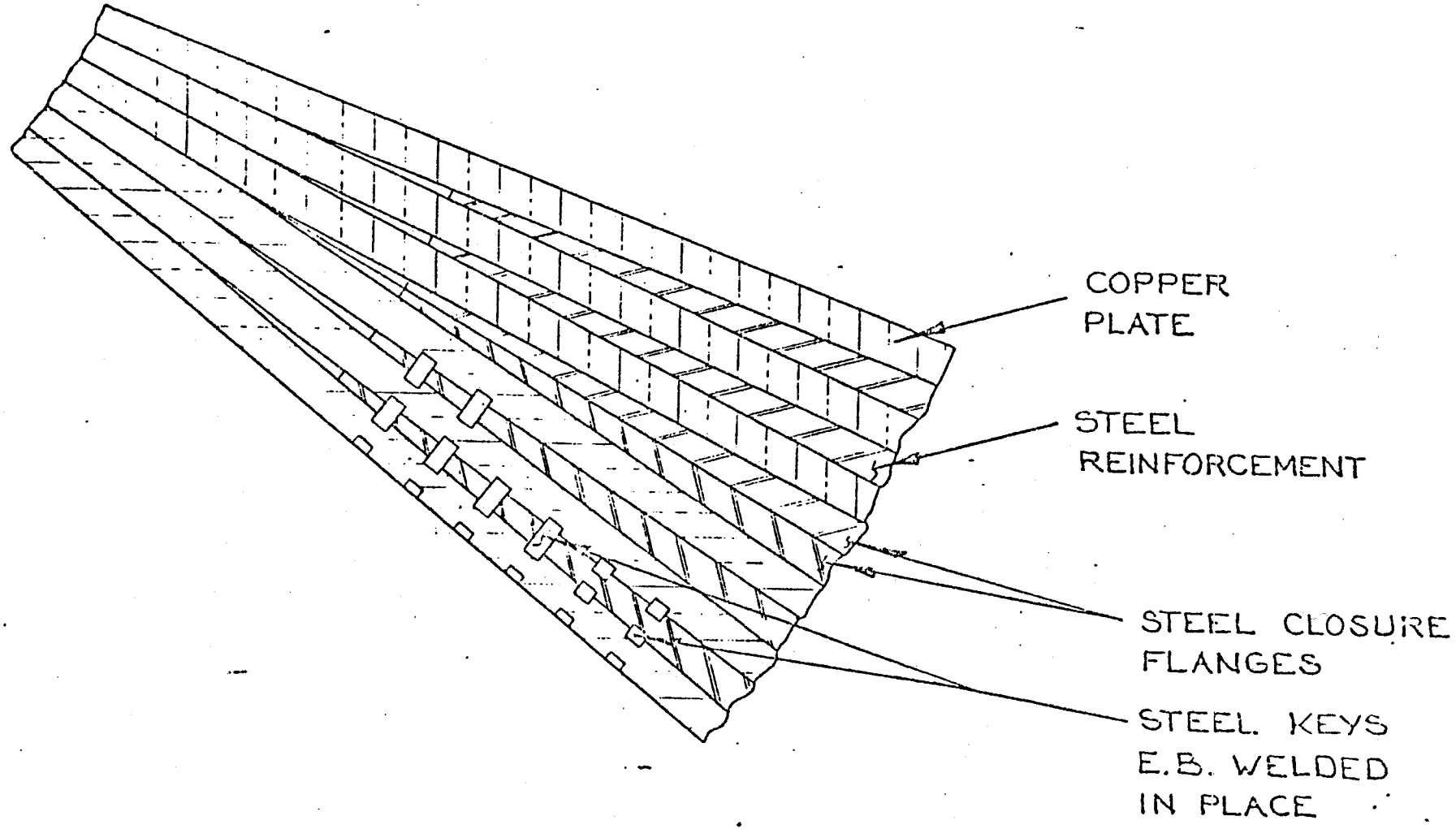

Figure 3.1.3 Components of the Basic TF Turn

ment immediately adjacent to the ports. That stress is alleviated by the radial extension of the reinforcing steel so that it is supported by the EF coils. Those coils (described below) have a large cross-section. Consequently, they are stiff enough to help support the local vertical loads in the outer leg of the TF coil (see Fig. 3.1.6).

The various discontinuities in the TF coil contribute to the ripple in that field. The principal factors causing ripple are: the 2.68° flanges of which there are 32; the 1.2 m $\times$ 0.8 m port openings which force the current to flow locally at a larger radius and which add to the ripple caused by 16 of the flanges. Ripple is reduced by the periodicity of the discontinuities. Thus 32 flanges of a given angle cause less ripple than 16. For this reason at the center of each half module, mid-way between a closure and a port flange, the sense of the copper plates is reversed by using a double steel reinforcement piece (see Figure 3.1.3). This effectively increases the periodicity of the flanges to a 64 fold symmetry. The ripple is estimated in section 3.2.

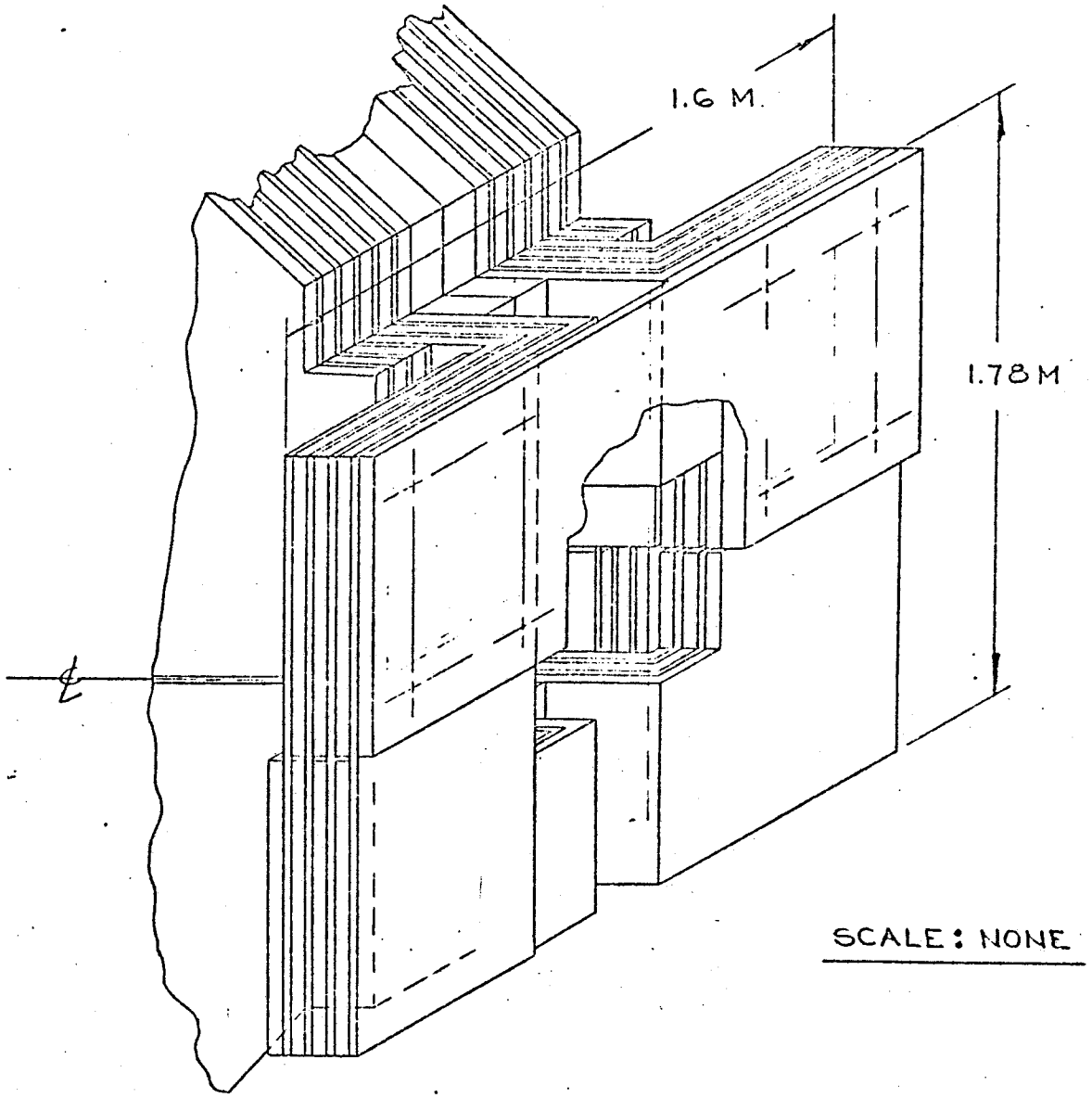

Figure 3.1.4 Copper TF Plates Folded Around a Port Opening

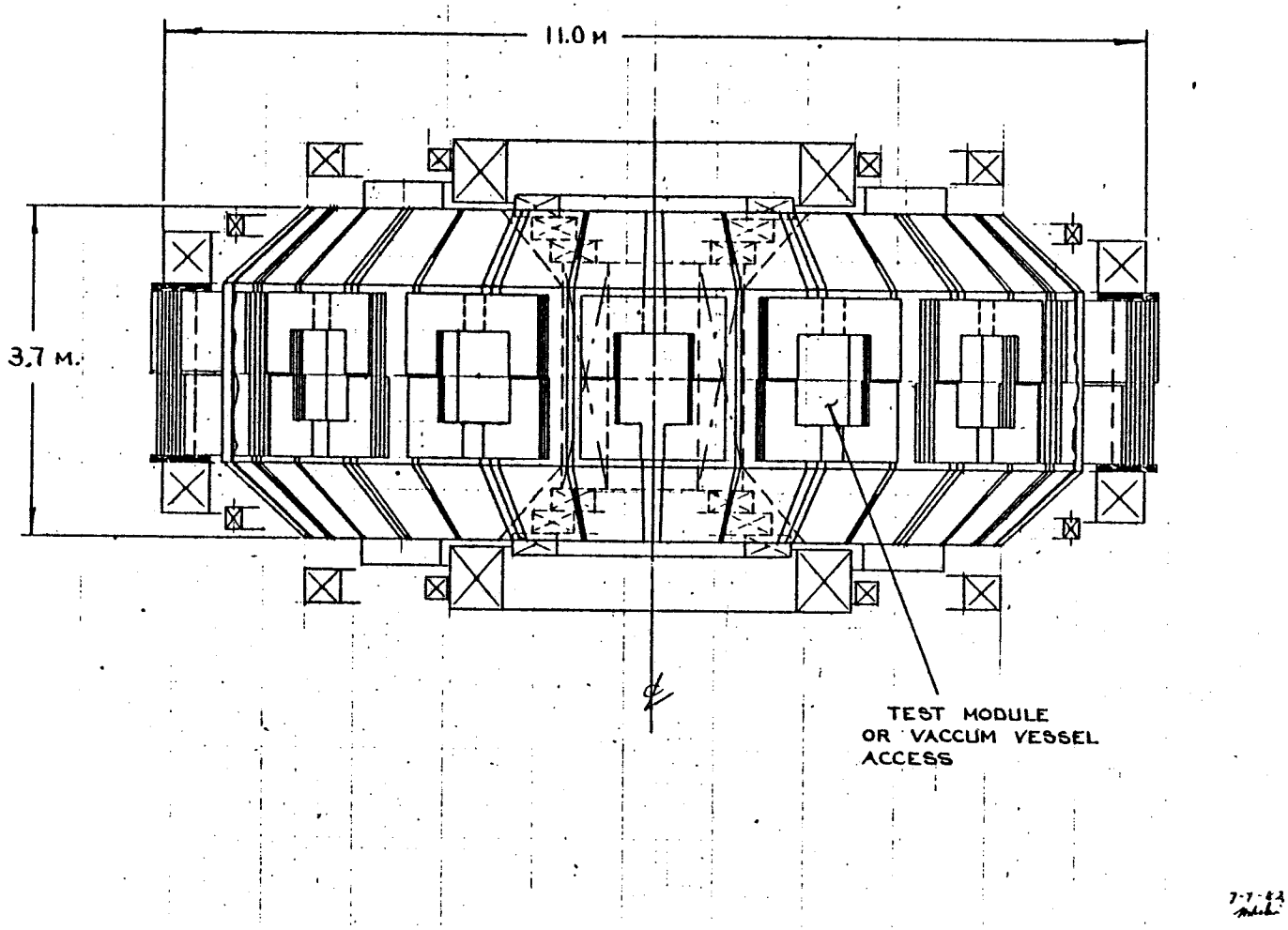

Figure 3.1.5 Elevation View of FED-R2

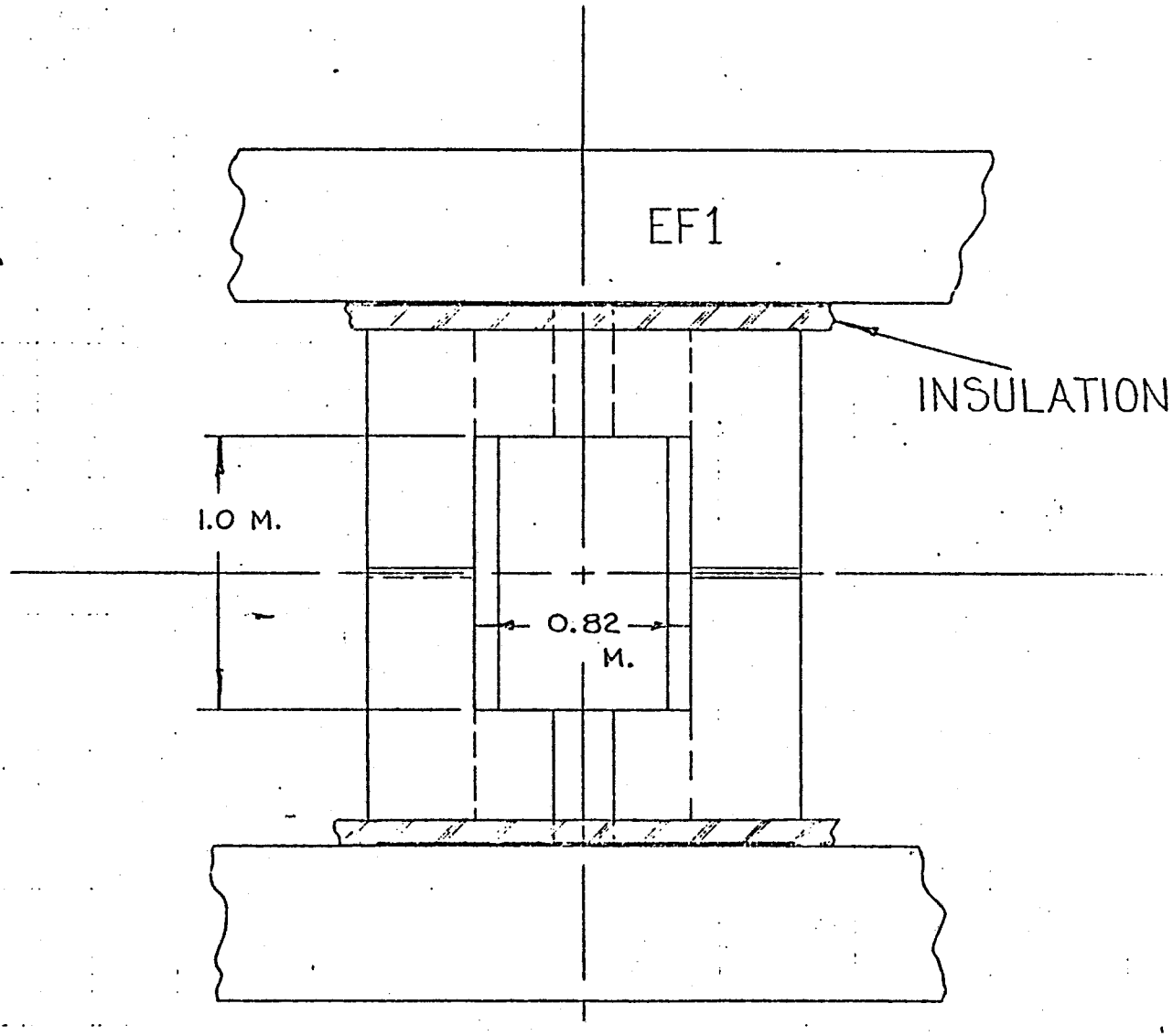

Figure 3.1.6 Partial Support of TF Port Conductors by EF Coil

TABLE 3.1.1

Toroidal Field Coil Parameters

Number of turns	384	
Number of modules	16	
Flange angle (32 flanges)	2.68°	
Fraction of TF periphery occupied by active turns	0.7618	(at 4.85 m radius)
Thickness of copper at 4.85 m (outer periphery)	3.017 cm	
Thickness of steel reinforcement at 4.85 m	2.829	
Radius at which steel reinforcement starts	2.5 m	
Overall height	3.7 m	
Number of cooling channels in throat	50	
Cooling channel equivalent diameter	5 mm	

3.2 Access to Plasma and Test Regions

Access to the plasma is provided by two means: large horizontal ports (used for diagnostics, auxiliary heating or for neutron applications) and smaller vertical ports, used mainly for diagnostics. The smaller ports as presently envisaged would be located in the mid-module stainless-steel flanges. They would be similar to the diagnostics ports in the ZEPHYR design[5]. The main purpose of these ports is to provide a small amount of vertical access for diagnostics.

The large horizontal ports are part of the 16 mid-module flanges. They provide access either to the plasma (3 ports) or to the blanket region (13 ports).

The plasma access is through a duct with a minimum aperture of approximately 1.0×0.6 m^2 (the opening in the TF magnet plate is 1.2×0.8 m^2). The ducts are perpendicular to the plasma surface.

Access to the blanket test region is through the TF magnet openings which measure 1 m high by 0.6 m wide. Space for test modules exists in 13 of the 16 modules. The width of the test space per port is approximately 1.8 m. This can be occupied by three 0.6 m wide units, which are inserted through the ports and then moved sideways on rails into their test position.

The large aperture required for horizontal access results in significant distortion of the current-carrying elements. The ripple in the toroidal field needs therefore to be calculated. This is done in the next section.

3.2.1 Toroidal Field Ripple

There are three types of ripple in the toroidal field in Bitter-type machines: the ripple due to the discrete toroidal field plates, that due to the flanges between modules, and the ripple due to the large apertures required for access to the toroidal bore.

The first type of ripple, that due to the discrete nature of the coils, is very small in BITTER designs due to the large number of plates. The effect of such ripple in plasma transport is therefore negligible.

The second type of ripple is due to the flanges. These flanges are necessary to allow modules to be joined together, and form the vacuum seal for the first wall. Furthermore, these flanges also allow vertical access to the plasma. This access is limited, but should be large enough to permit vertical diagnostics.

The ripple due to the flanges is large in the region near the flanges and decreases rapidly toward the mirror axis of the machine.

Figure 3.2.1 shows the ripple in the plasma region due to the lack of $16 - 1°$ regions in an otherwise perfect torus. The 16 regions represent the 16 closure flanges present in the design. The ripple shown in Figure 3.2.1 is defined as

$$\delta = \frac{B_\phi(r,\theta,\phi) - \overline{B_\phi}(r,\theta)}{\overline{B_\phi}(r,\theta)}$$

where $B_\phi(r,\theta,\phi)$ is the toroidal field at location (r,θ,ϕ) and

$$\overline{B_\phi}(r,\theta) = \frac{1}{2\pi}\int_o^{2\pi} d\phi B_\phi(r,\theta,\phi)$$

where ϕ is the toroidal angle. Figure 3.2.1 shows contours of constant ripple at the mid-location of a flange.

In order to calculate the ripple shown in Figure 3.2.1, a typical TF coil is simulated by a set of 4 closed current-carrying filaments. The current-carrying filaments are made of a large number of straight filaments, such that one ends where the next one starts. The location of the filaments is such that they approximate uniform current density in the conductor that is being simulated. As FED-R2 is a steady-state machine and because it is cooled in such a way that temperatures in poloidal sections is approximately constant, the uniform

current density across a poloidal sector is appropiate.

The largest toroidal ripple due to the flange occurs in the top and bottom of the plasma. The structure of the ripple in the toroidal field is sinusoidal throughout most of the plasma region. This is shown in Figure 3.2.2. This figure shows contours of constant toroidal field ripple in the midplane of the machine. Shown is a sector region. The minor radius is in the coordinate and the toroidal angle of 1/32 of the machine is in the ordinate. $\phi = 0$ represents the mid-location of the flange, and $\phi = \frac{\pi}{16}$ is half-way between flanges. As long as the angle subtended by the flange is not very large, the toroidal field ripple approximately scales linearly with this angle.

The flanges in FED-R2 would not be exactly as described by the constant angle approximation. However, the numbers indicate that for an edge ripple of $\leq$ 1% on the edge of the plasma, the angle subtended by the flange has to be $\leq 6°$. This corresponds to a flange thickness at the location of the plasma major radius of 0.3m. It should be noted that the further reinforcement at the center of the a half module and the additional flange at the center of the port would increase the periodicity of the perturbation creating the ripple and therefore reduce the ripple further.

3.2.2 Port Ripple

The largest contribution to the toroidal field ripple comes from the access ports. Although the structure around the ports varies, depending on whether the port allows access to the plasma vacuum or not, the shape of the conductors around these two types of ports is identical. Therefore, for ripple calculations, it is assumed that there are 16 identical ports, with a geometry schematically depicted in Figure 3.2.3. The ripple calculations in this case are done using filamentary elements that represent the conductor shape around the port, and conductors that represents the current that has been removed from what, in the absence of the port, would be an ideal

torus. Figure 3.2.3 shows the filamentary elements used to represent the port. The ripple calculations include 16 ports, plus the ideal torus. The ripple can therefore be calculated very fast, without involving in the calculations the unperturbed conductor (which is included in the result in the form of an ideal 1/R variation).

Figure 3.2.4 shows contours of constant toroidal field ripple in the location at the port. The toroidal field ripple is approximately constant at constant major radius and varies with distance from the port. The largest toroidal field ripple is ~0.008% at the outer edge of the plasma.

The toroidal field ripple on the midplane of the machine is shown in Figure 3.2.5. The location of the port is at $\phi = 0$. The ripple decreases very fast away from the plasma edge, and is ~.05% at the location of the plasma center.

Although the opening is substantial, the ripple has been kept low because:

- The distance between the port and the plasma is relatively large to allow for shielding and/or blanket test modules.
- There are 16 ports, increasing the symmetry and the gradient of the ripple away from the port.
- The current removed to make room for the port has been located as close to the plasma as physically possible.
- The width of the outer leg is large, removing the centroid of the current in the unperturbed turns away from the plasma.

The port size is thus not determined by the toroidal field ripple limitations, but by structural and engineering considerations.

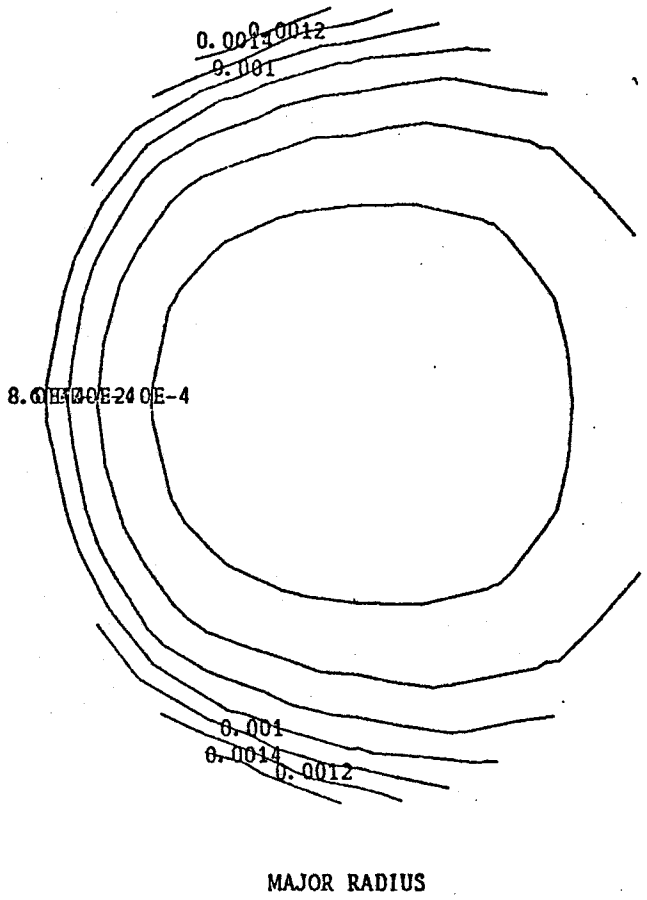

Figure 3.2.1 Contours of Constant Toroidal Field Ripple due to 16 Equally Spaced 1° Flanges. The Ripple is Measured in the Cross Section Through the Middle of the Flange.

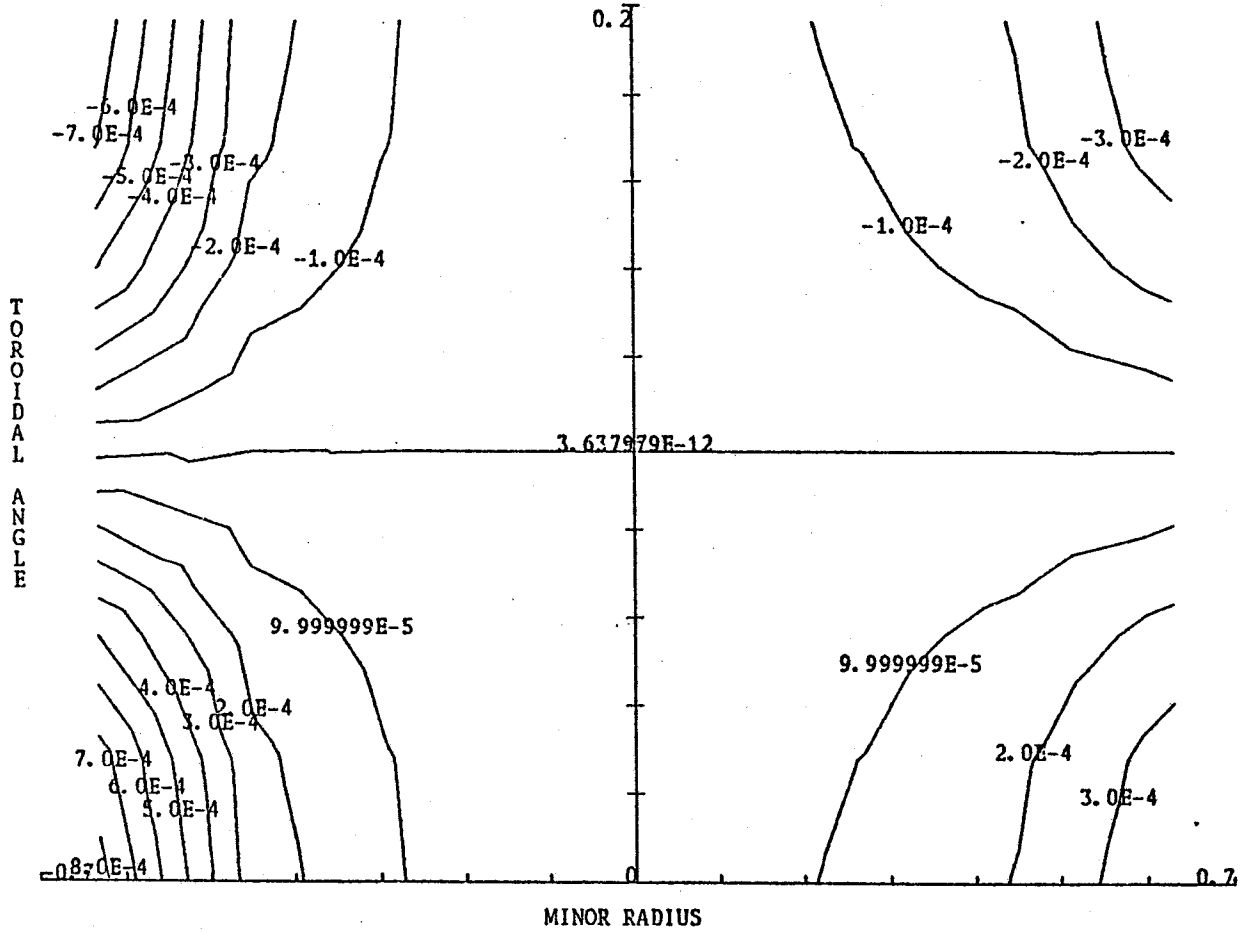

Figure 3.2.2 Contours of Constant Toroidal Field Ripple due to 16 Equally Spaced 1° Flanges. The Ripple is Measured in the Midplane of the Machine. $\phi = 0$ Corresponds to the Location of the Flange, and $\phi = \pi/16$ Corresponds to the Mid Location Between Flanges. The Ordinate Represents the Major Radius Location.

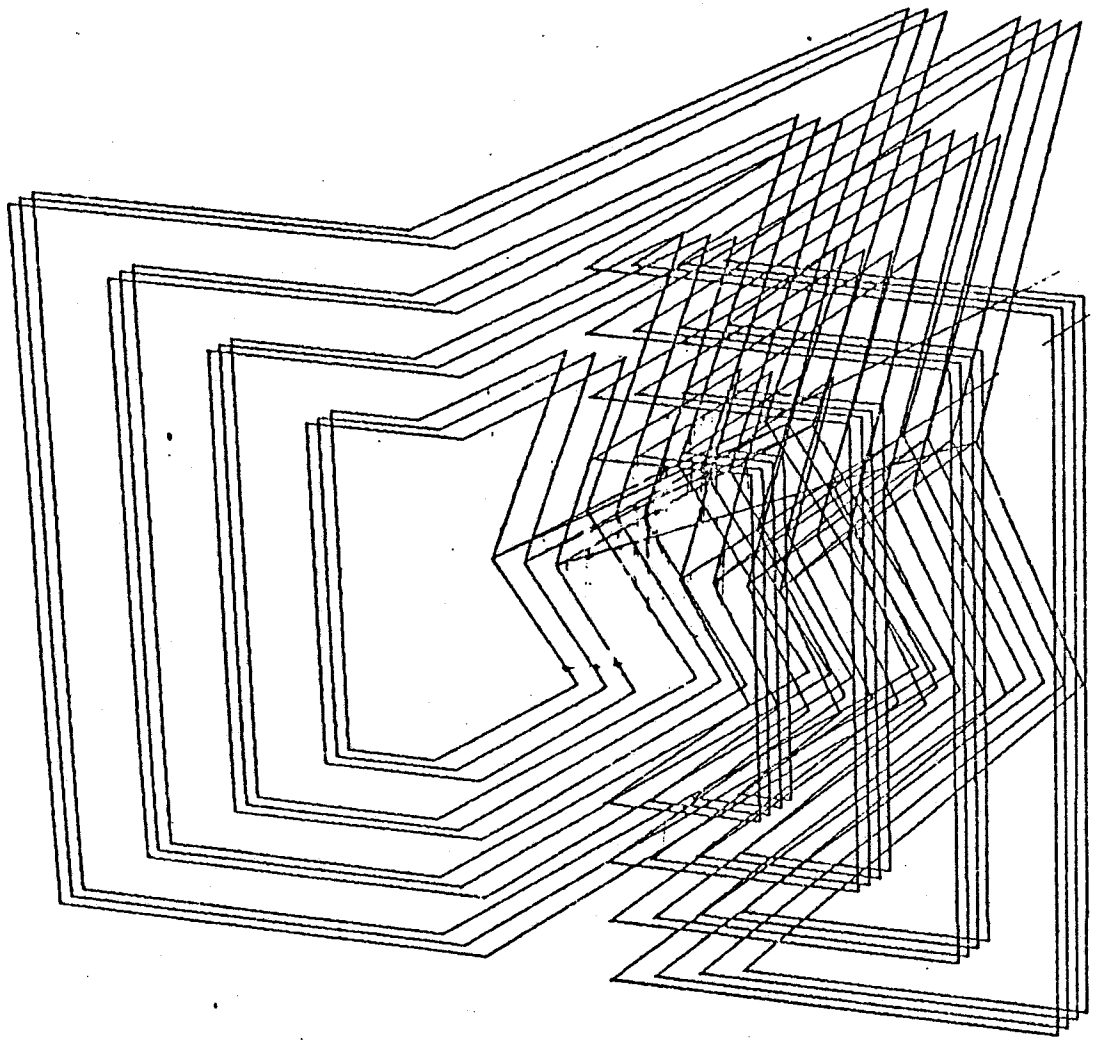

Figure 3.2.3 Schematic Diagram of the Filaments used to Stimulate the Port.

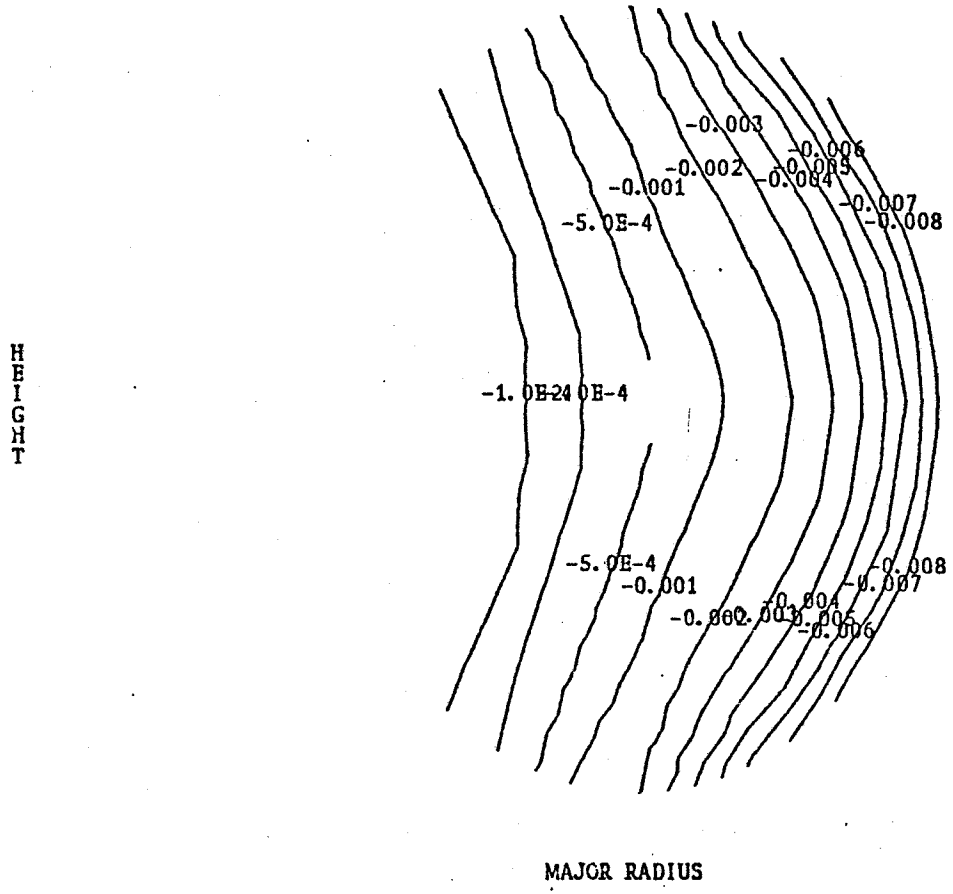

Figure 3.2.4 Ripple due to the Main port. The ripple is Calculated in the Cross Section were it is the Largest (Close to the Middle of the Port). It Does not Correspond to the Middle of the Port due to Port Asymetry.

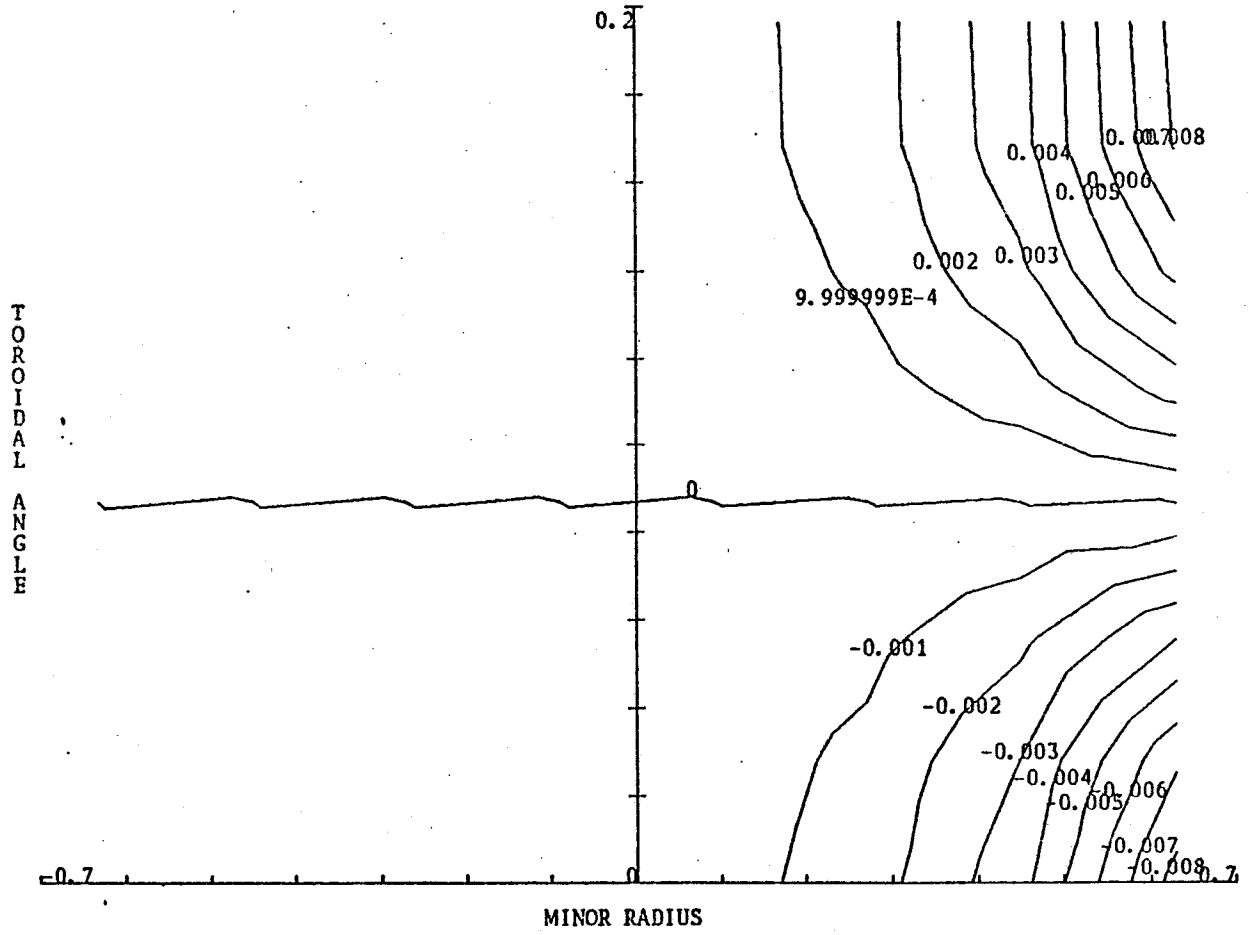

Figure 3.2.5 Ripple due to the Main port, Calculated in the Midplane of the Device. $\phi = 0$ Corresponds to the Middle of the Port and $\phi = \pi/16$ to the Point Half Way between Ports.

3.3 Equilibrium Field System

In this section, the vertical field system is described. The optimization of the EF system for a resistive coil reactor is described in section 3.3.1. Parametric studies are performed around a specific toroidal field coil envelope. An illustrative design is presented in Section 3.3.2.

There are significant differences between the poloidal field system in a superconducting FED and in FED-R2. The main differences are:

- The equilibrium field coils can be located much closer to the plasma in reactors with resistive coils than in reactors with superconducting coils because of:
- Reduced shielding between toroidal field coil and plasma
- Reduced shielding and thermal barriers between EF coils and TF coils
- Smaller ripple, which means reduced that the outer leg of the TF coil (and therefore, the main EF coil) can be located closer the plasma
- Less height for the TF coil, which implies that the shaping coils can be closer to the plasma.
- There is a region in space close to the main axis of the machine that is readily available in resistive magnets but not so in superconducting ones. This region is ideal for the location of shaping coils in order to elongate and provide large triangularization to the plasma.

Because the TF coils require considerable power dissipation, then, as long as the requirements for the EF coils are a small fraction of those of the TF resistive coil, the attractiveness of superconducting EF systems is reduced.

In this section the EF system for a resistive coil reactor is described. However, detailed comparisons between the EF system of a resistive coil reactor and that of a superconducting coil reactor are not made.

3.3.1 Parametric Studies for the EF System

In this section, an optimization of the vertical field system for a specific TF design is performed. The geometry of the TF coil used in the optimization studies of the EF system are shown in Figure 3.3.1.

Because the equilibrium field requirements are larger for the case of $P_{wall} = 4\text{MW/m}^2$, it has been used for the parametric optimization study.

The optimization study has been performed as follows: for a given set of plasma parameters and a boundary for the TF coil, the optimum coil location is determined. When that location is determined, the current densities in the coils are varied. The design point for the illustrative parameters is then chosen.

It would in principle be possible to calculate the vertical field system using an equilibrium field coil for each particular case.[6] This procedure would be tedious and time consuming. The approach that has been used relies on a fit to the requirements of the vertical field system derived from a small, but carefully chosen set of runs of the equilibrium field system. A fit to the results is then performed, and a check is performed on a few cases. The fits are easy to use and allow the possibility of doing fast scans over large regions of available space.[7]

There are four parameters of interest in performing the optimization study of the EF system. These are:

- Resistive losses during the plasma burn
- Energy stored at peak current
- Mass of the coils
- Ampere turns.

Figures 3.3.2 through 3.3.5 show the resistive loses, at peak conditions for $P_{wall} = 4\text{MW/m}^2$, the stored energy at peak field, the weight of the coils and the number of MA-turns for the TF coil outer envelope shown in Figure 3.3.1. These Figures show contours of constant resistive power, stored energy, weight and MA-turns

of the vertical field system as the locations of the main and shaping EF coils are varied. The coordinate ℓ_1 represents the lowest point of the main EF coil, and the ordinate represents the point of minimum major radius of the shaping coil (see Figure 3.3.1). It is assumed that the current density in the main equilibrium field coil is $j_1 = 1.0 \times 10^7$ A/m^2 and in the shaping coil is $J_2 = 1.5 \times 10^7$ A/m^2. In Figures 3.3.2 through 3.3.5 it is assumed that the major radius of the main coil, R_1 and the height of the shaping coil R_2 are such that the clearance between the TF coil and the poloidal field coils is 0.1 m. The coil locations are then self-consistently determined from ℓ_1 and ℓ_2 and the current density in the coils.

As can be seen from the figures, the optimum location of the coils is such that ℓ_1 is as small as possible, that is, the main equilibrium coil should be as close as possible to the midplane. The parameters of the system do not depend strongly on the location of the shaping coil. ℓ_1 is determined from access considerations: the coil should clear the ports in the TF coil. From engineering considerations (described in the structures section), the clearance should be $\sim$ 0.5 m. As the port half height is 0.5 m, then the height of the lowest point of the main EF coil is $\ell_1 = 1.0$ m. The location of the shaping coil is such that it clears the inner corner, that is, $\ell_2 \sim R_a$ (where $R_a = R - a - \delta_i$). Reducing ℓ_2 has the advantage of giving the plasma a significant amount of triangularity without increasing the requirements of the EF system considerably. Access to this area without having to place the coils inside the toroidal field system is one of the advantages of resistive versus superconducting magnets.

Next, the optimum current density in each coil is determined. Figures 3.3.6 through 3.3.9 show contours of constant peak resistive power, peak stored energy, weight and number of MA-turns as functions of the current densities in the main EF coil (j_1) and in the shaping coil (j_2). The optimum in this case is not as clear:

as the resistive power decreases, the stored energy increases. The point $j_1 \sim j_2 \sim 1.2 \times 10^7$ MA/m^2 has been chosen as a compromise.

3.3.2 Illustrative Design

There are two pairs of EF coils, a "dipole" pair (main equilibrium coils) located just outside the outer edge of the TF coil and a "quadrupole" pair (shaping coils) located just above and below the TF coil. The dipole pair produce a field which generates a radially inward force on the plasma and the quadrupole pair generates a force on the plasma to elongate it in the vertical direction. The position, dimensions, currents and forces on these coils are shown in Fig. 3.3.10. The parameters of the coils are given in Table 3.3.1.

The coils are wound from hollow copper conductor of 7.2 cm square section with 3 mm of insulation around the outside of each conductor (Figure 3.3.11). The cooling channel consists of four holes each 1.8 cm in diameter. The thermal and mechanical loads in the conductor are modest, for all the EF coils; high conductivity copper has therefore been assumed.

Support of the dipole EF coil is from the steel reinforcement plates of the TF coil to which they are attached by quick release toggle clamps (for ease of disassembly). The dipole coil provides a small part of the support for the copper TF plates in the region of the ports where the steel TF reinforcement is discontinuous. Because of the high forces between EF2 and OH7 coils and between EF1 and OH5 coils, these pairs are structurally joined as units.

The hydraulic arrangement of the EF coils is designed to minimize pumping power and erosion, to the extent compatible with simple coil construction.

The quadrupole coil, EF1, consists of 9 pancakes each with 8 turns (Figure 3.3.12). Of these 72 turns, only 66 carry the full current of 50 kA. The remaining 6 are used to trim the field with a small current. The cooling water flows inwards through the turns of each pancake, thus having 9 flow paths in parallel. Manifolds at the outside and inside distribute the water. The dipole coil, EF2, is treated similarly to EF1. Eight pancake coils

each of seven turns provide 56 turns of which 55 carry 50 kA and one carries a trim current of 10 kA.

The waveforms of the currents in the main and shaping equilibrium field coils are shown in Figure 3.3.13. It is assumed that at $t = 0$ a full size circular plasma is created. At $t = 5s$, the plasma is enlarged to full elongation. Finally, heating is applied ($t = 11s$). The burn-time last for 100 s at which time the plasma is brought down in a sequence reversing the initiation sequence. Note that the current in the shaping coil reverses direction as the plasma is elongated.

TABLE 3.3.1

EF Coil Specifications

Parameter (referred to one coil of pair except where noted)	EF1 Quadrupole	EF2 Dipole
Amp turns, MA	-3.3	2.76
Coordinates of center, m	R = 1.84 Z = 2.12	R = 5.17 Z = 1.30
Cooling channel dia., cm	4 × 1.8	4 × 1.8
Operating current, kA	50.0	50.0
Conductor size, cm	7.2 × 7.2	7.2 × 7.2
Overall size incl. insulation, cm	7.8 × 7.8	7.8 × 7.8
Number of turns	65	55
Conductor array	8 h. × 9 v.	7 h. × 8 v.
Trim current, kAt		+10.0
Peak dissipation power MW	8.87	20.86
Water velocity, ms^{-1}	20	20
Heat transfer coefficient $W\,cm^{-2}C^{-1}$	5.34	5.34

TABLE 3.3.1 (continued)

Parameter (referred to one coil of pair except where noted)	EF1 Quadrupole	EF2 Dipole
Copper surface temp. rise, C	22.8	22.8
Water flow, m^3s^{-1}	.184	.1628
Water bulk temp. rise, C	12.0	32.0
Pumping power, kW	128	112
Axial force, MN		-10.67
Total radial force, MN		+34.88
Hoop stress in cm, MPa		25.7
Weight, tonnes	30.9	66.25
Stored energy	203 MJ	total system
Resistive power	59.5 MW	total system
Pumping power	0.48 MW	total system

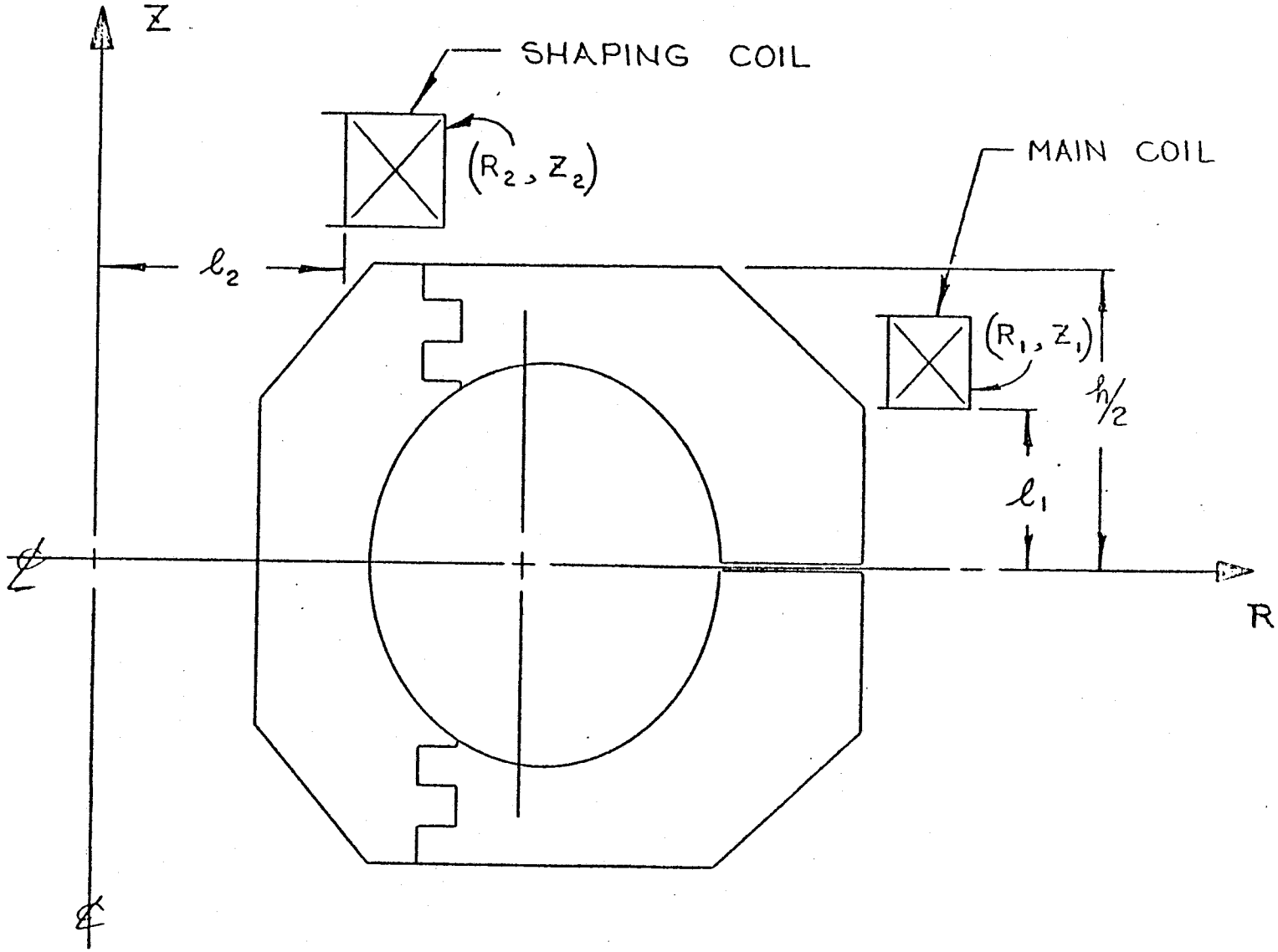

Figure 3.3.1 Positions of EF Coils

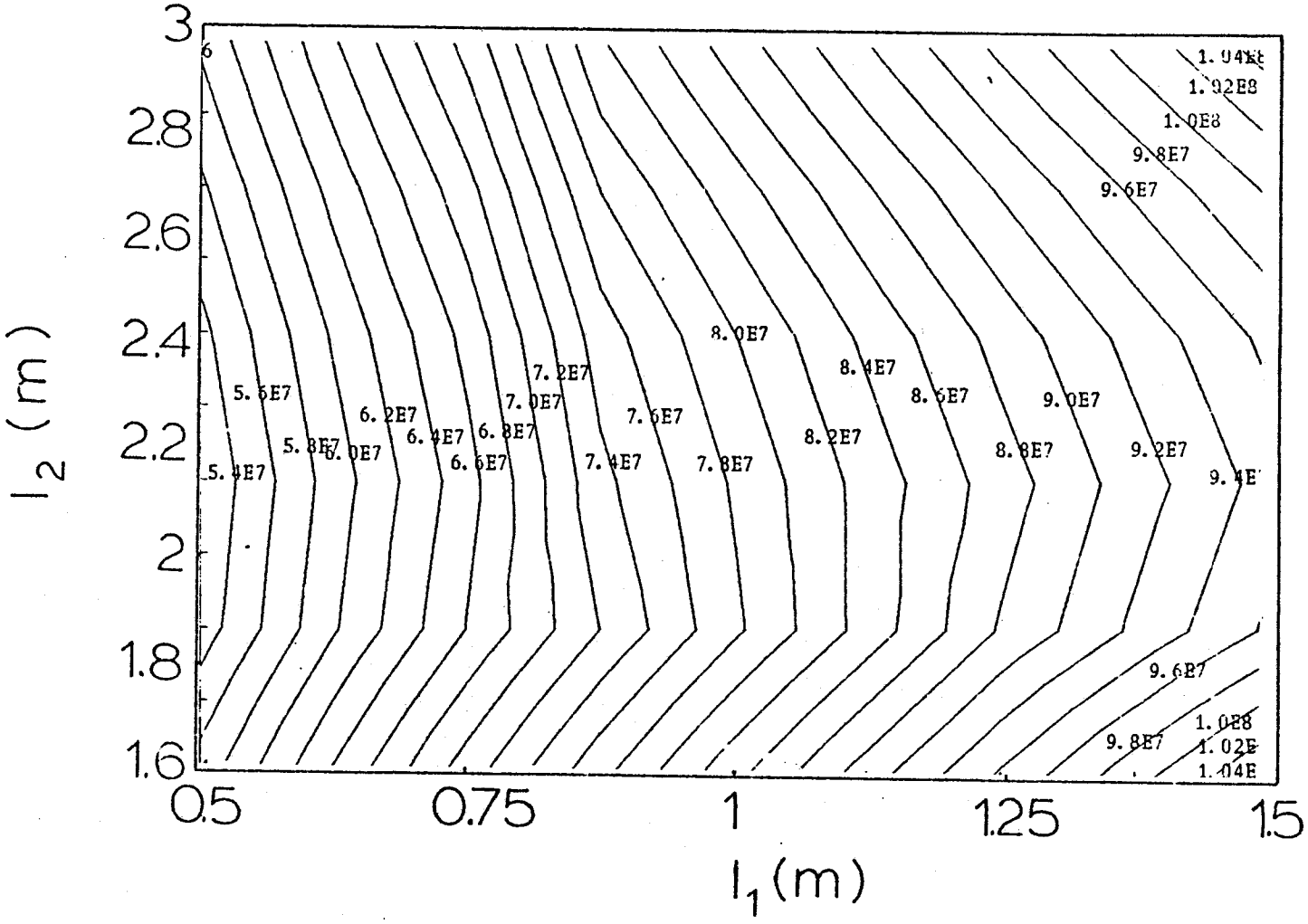

Figure 3.3.2 Contours of Constant Power Dissipated as a Function of the Location of the Main and Shaping Equilibrium Field Coils.

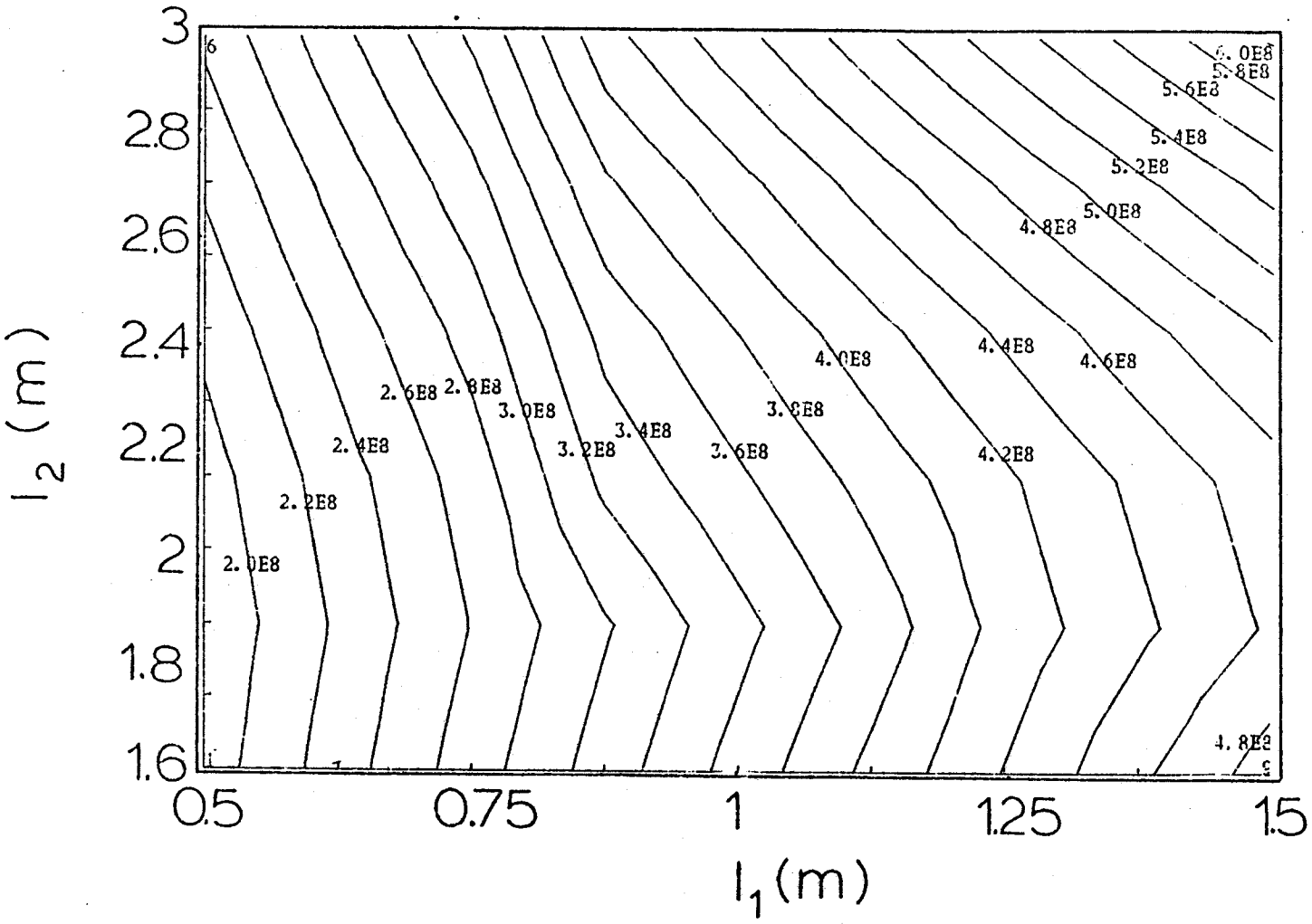

Figure 3.3.3 Contours of Constant Stored Energy in the EF System as a Function of the Location of the Main and Shaping Equilibrium Field Coils.

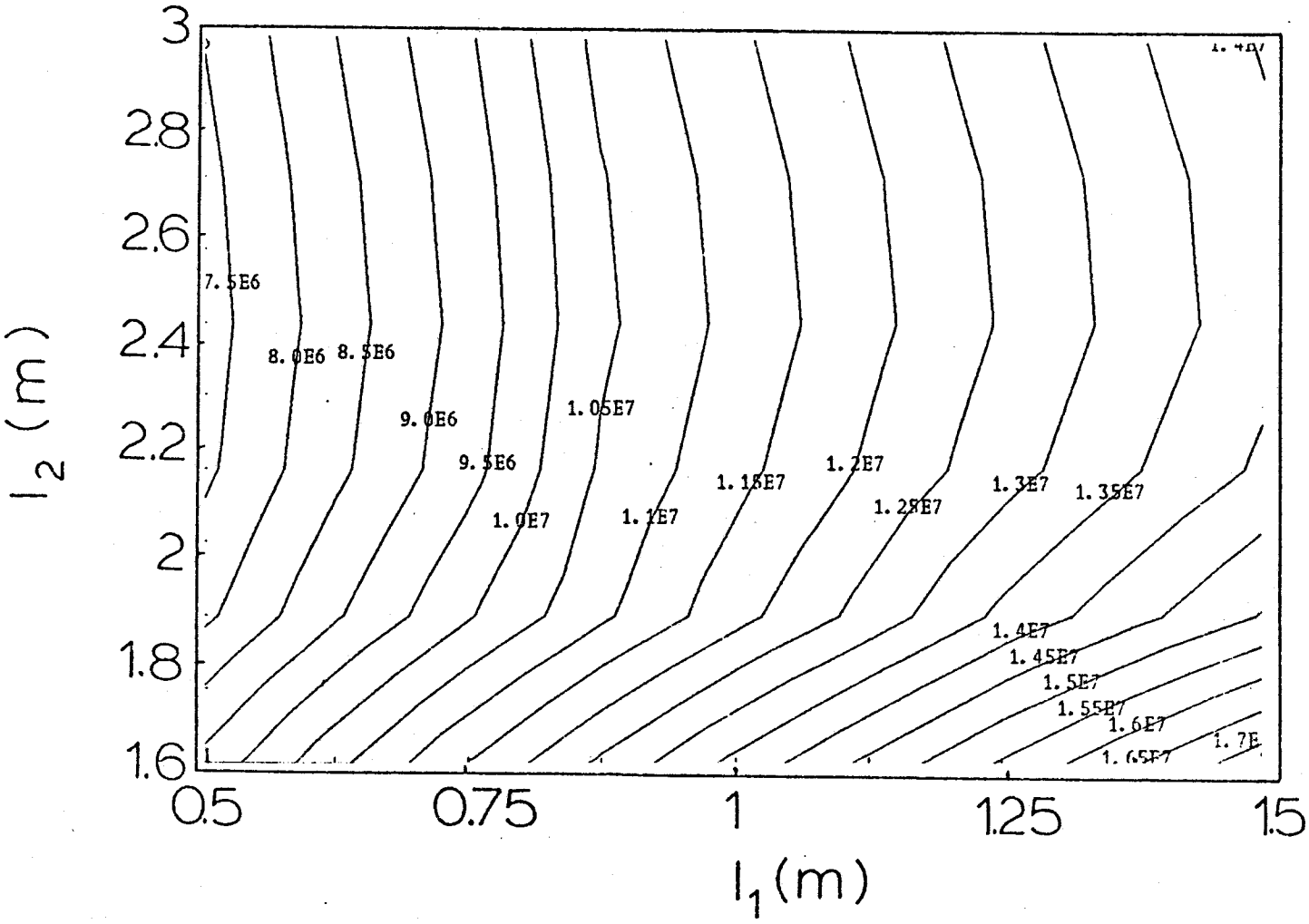

Figure 3.3.4 Contours of Constant Ampere turns as a Function of the Location of the Main and Shaping Equilibrium Field Coils.

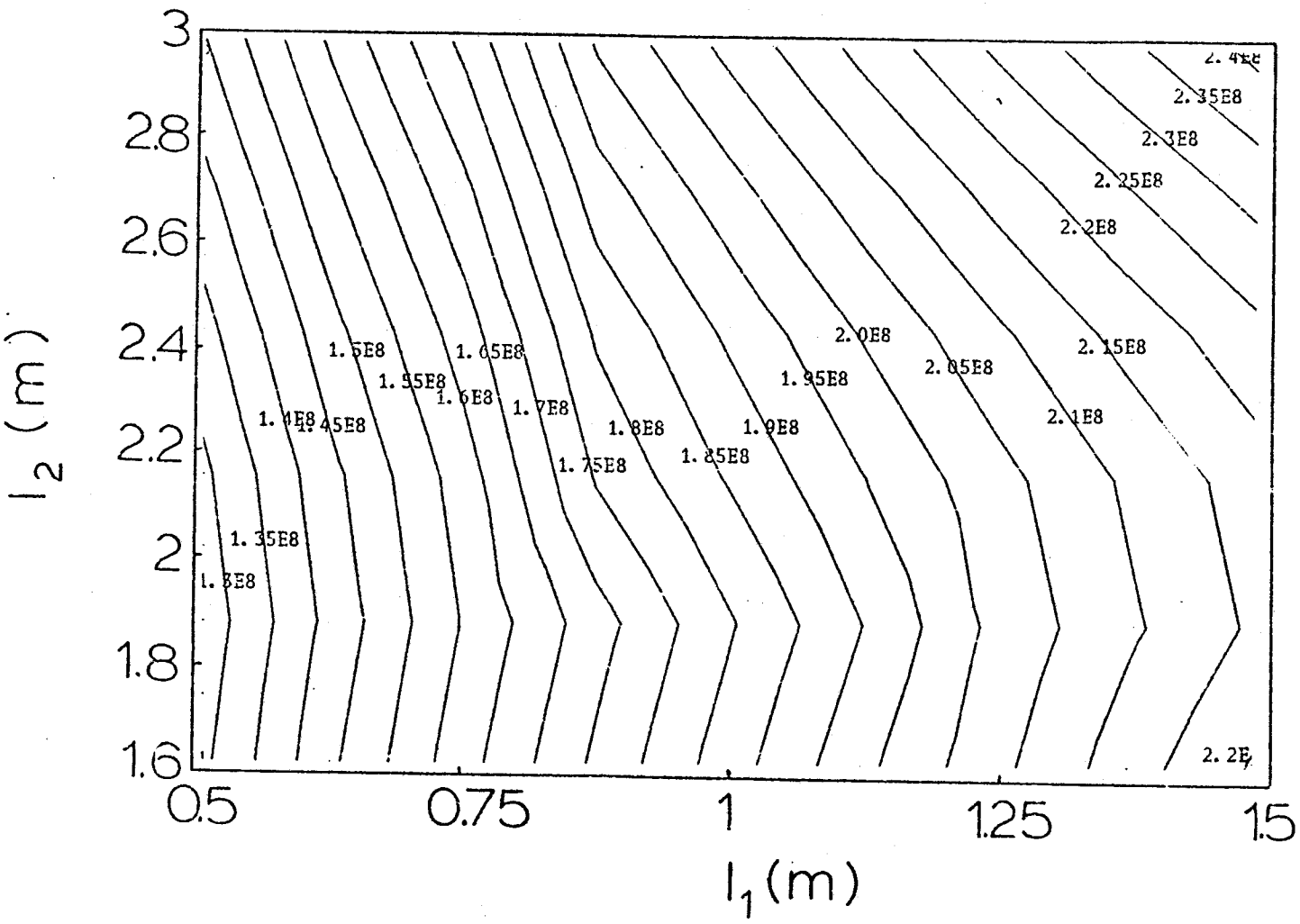

Figure 3.3.5 Contours of Constant Weight of the EF System as a Function of the Location of the Main and Shaping Equilibrium Field Coils.

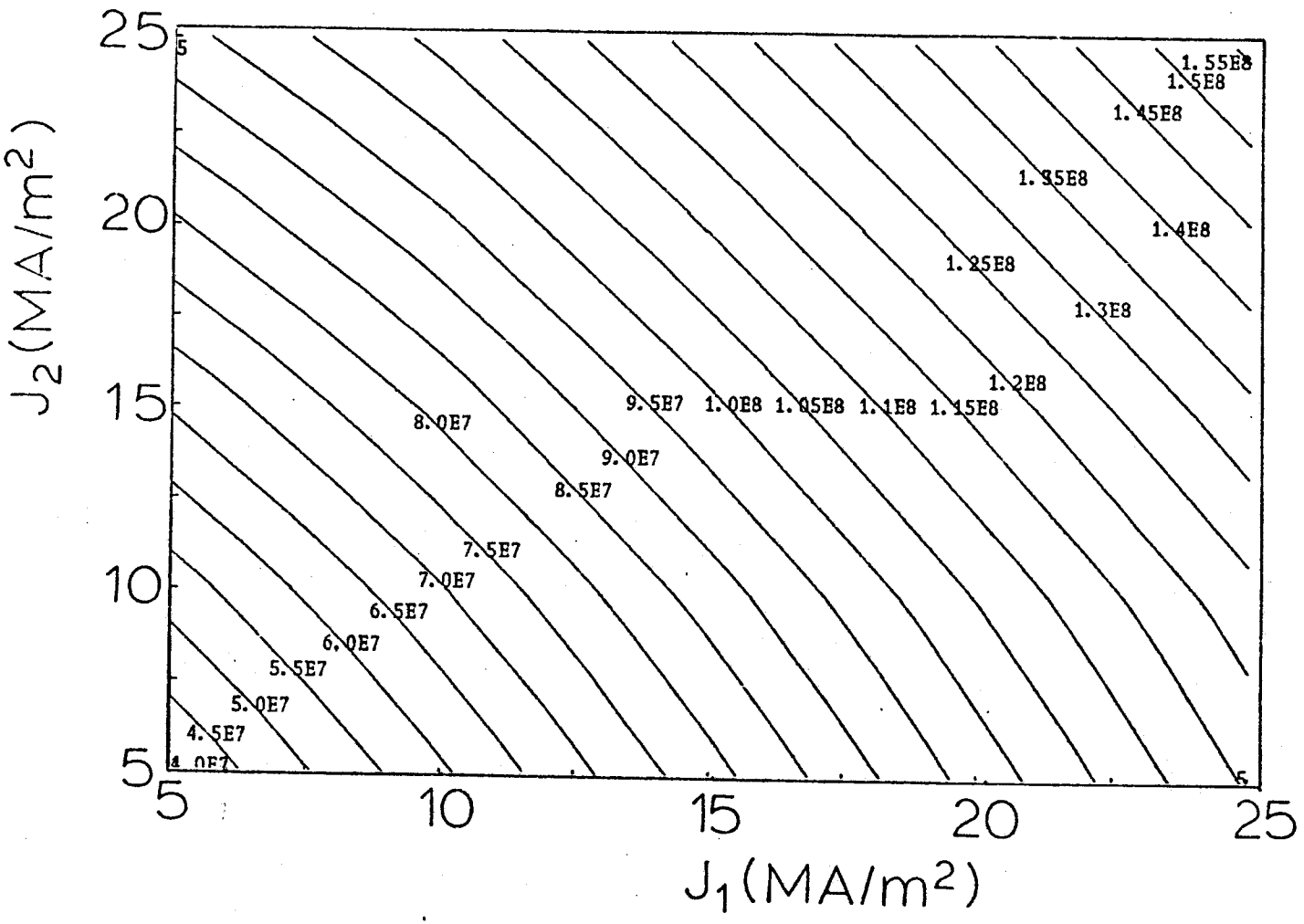

Figure 3.3.6 Contours of Constant Power Dissipated as a Function of the current density in the main (j_1) and shaping (j_2) equilibrium field coils.

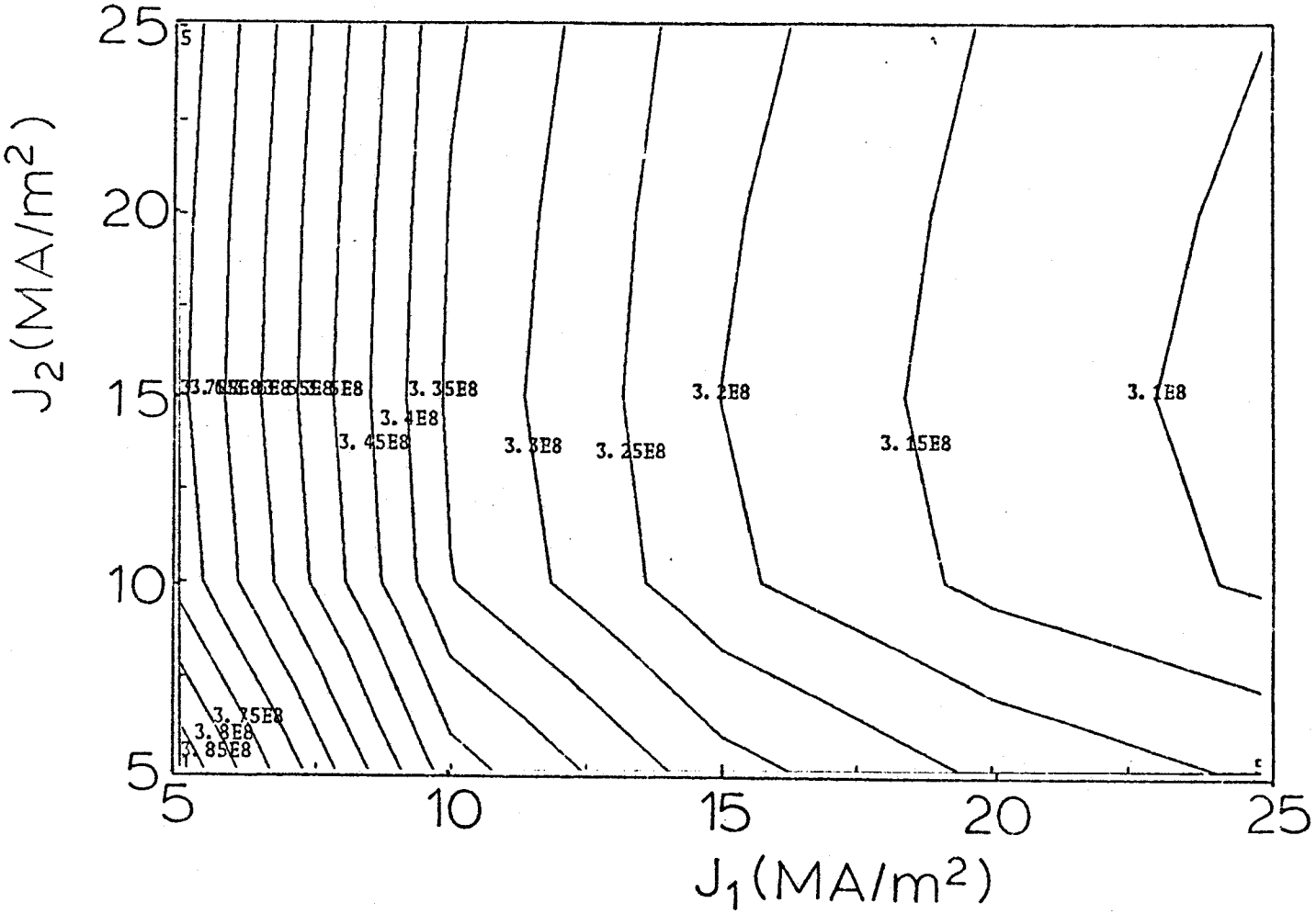

Figure 3.3.7 Contours of Constant Stored Energy in the EF System as a Function of the current density in the main (j_1) and shaping (j_2) equilibrium field coils.

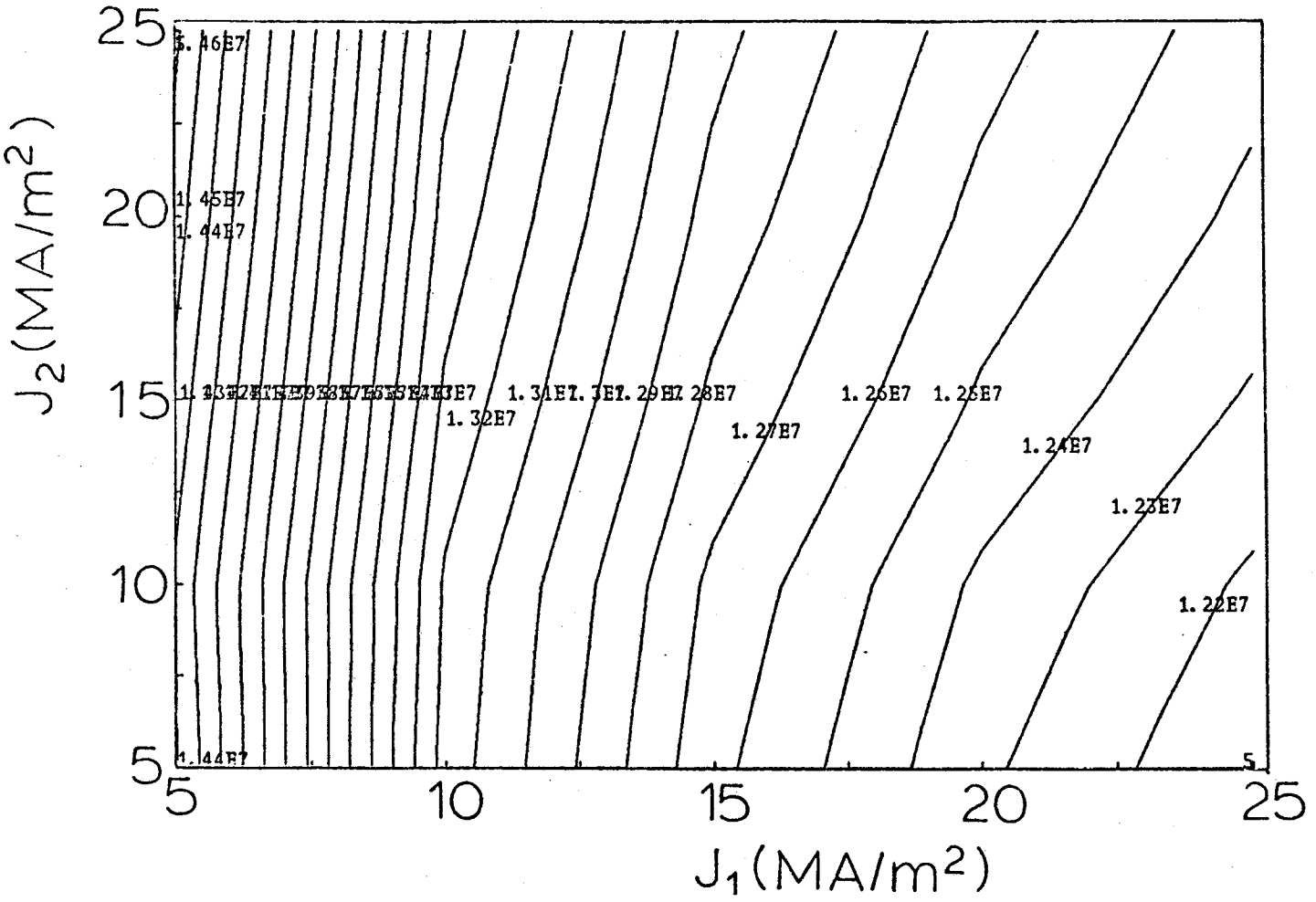

Figure 3.3.3 Contours of Constant Ampere turns as a Function of the current density in the main (j_1) and shaping (j_2) equilibrium field coils.

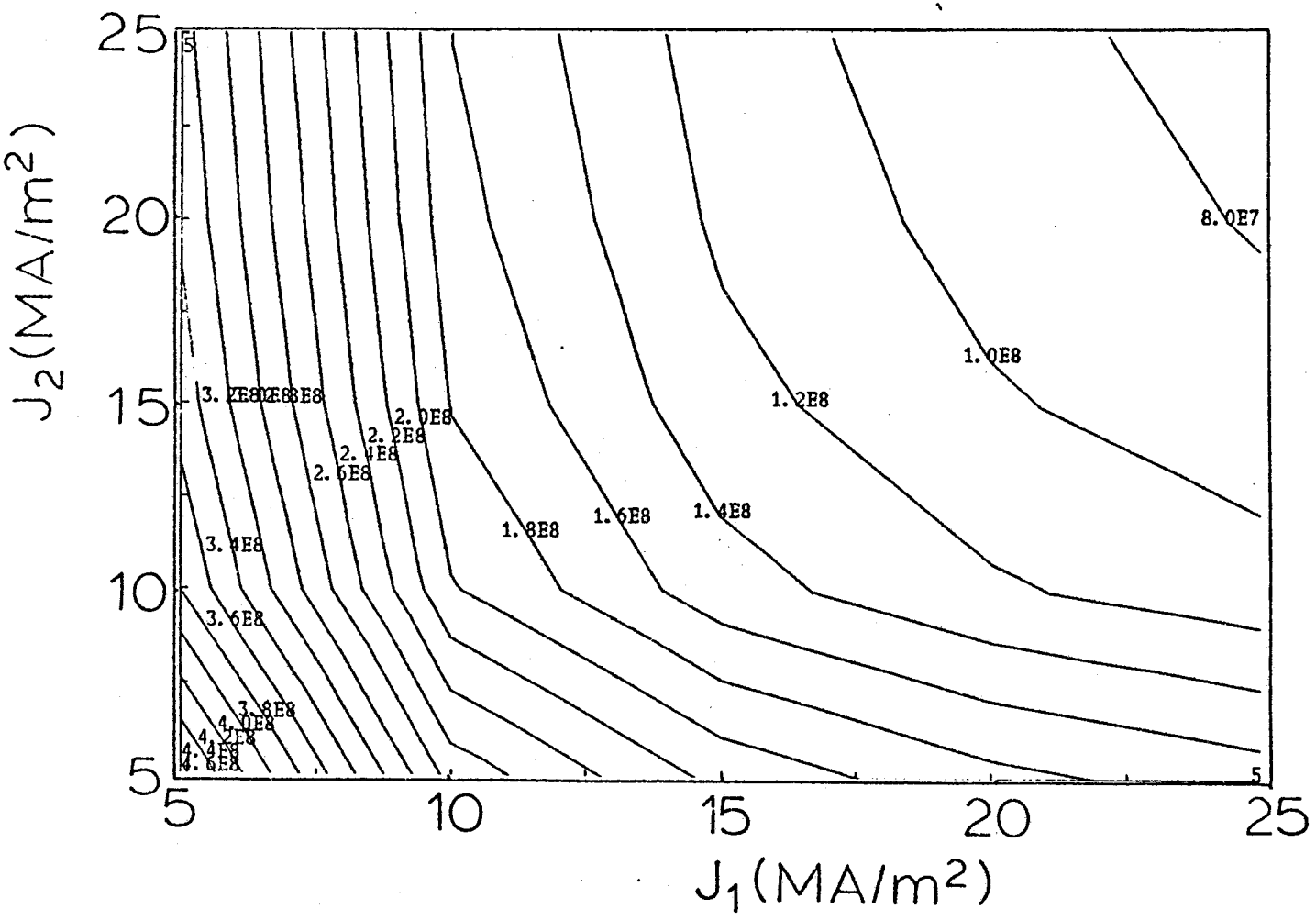

Figure 3.3.9 Contours of Constant Weight of the EF System as a Function of the current density in the main (j_1) and shaping (j_2) equilibrium field coils.

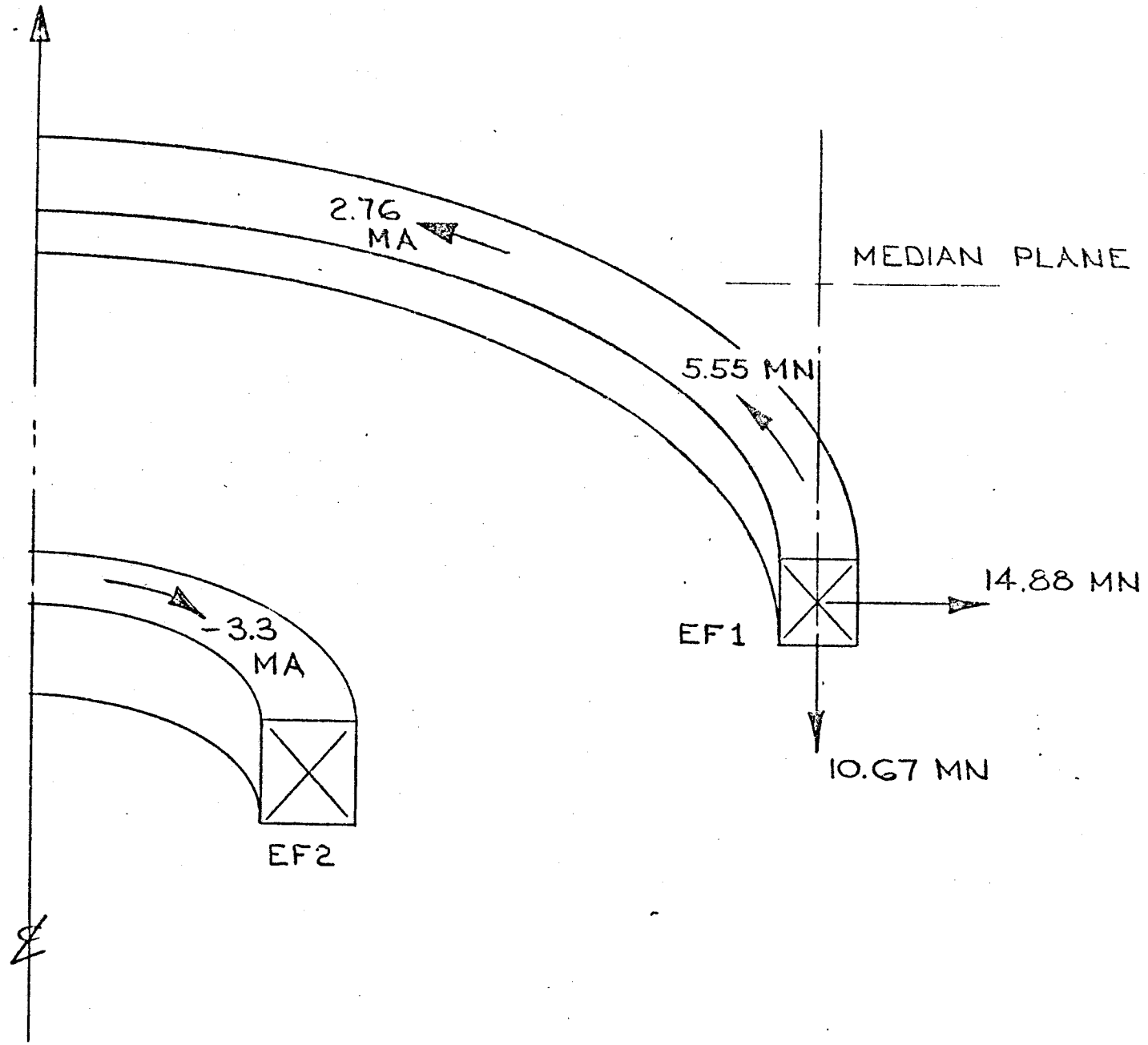

Figure 3.3.10 Currents and Forces in the EF Coils (shown are the coil below the median plane)

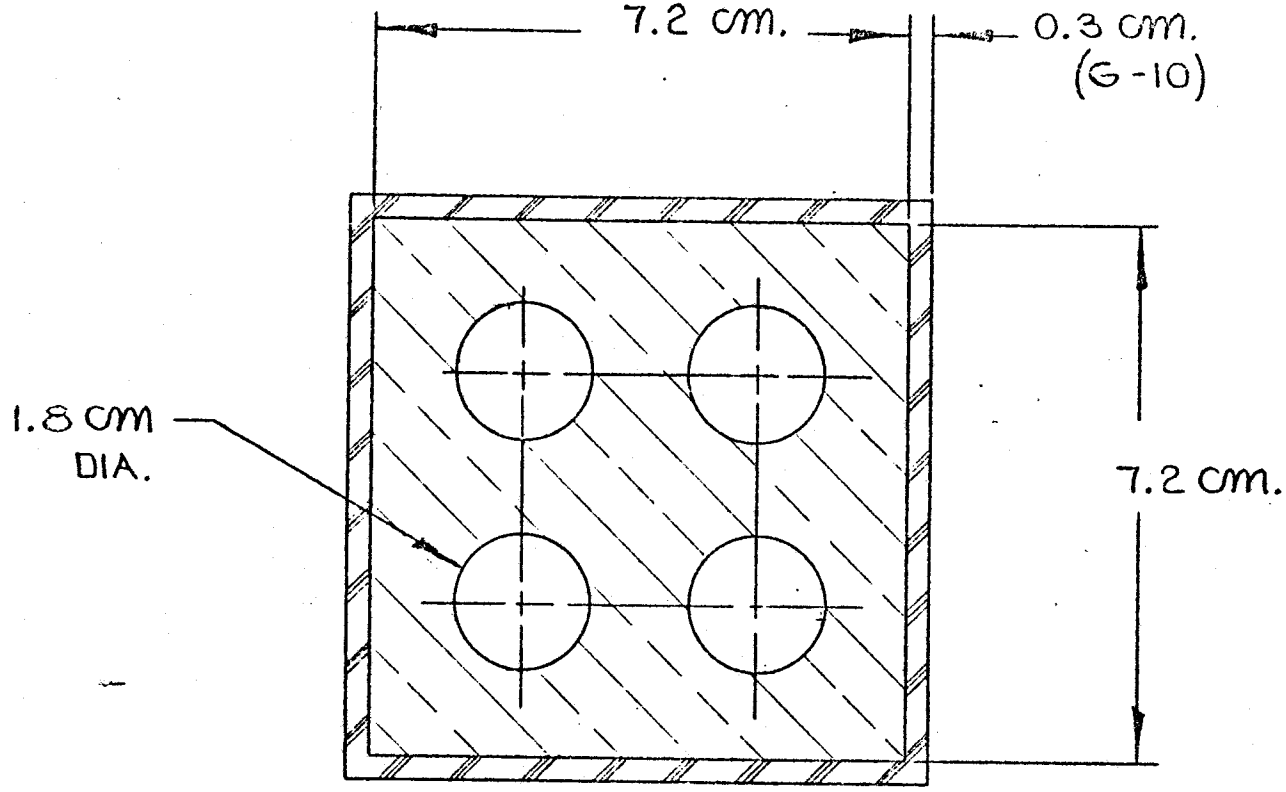

Figure 3.3.11 Cross Section of EF Coil Conductor (also used in OH 5,6 & 7)

7-7-82

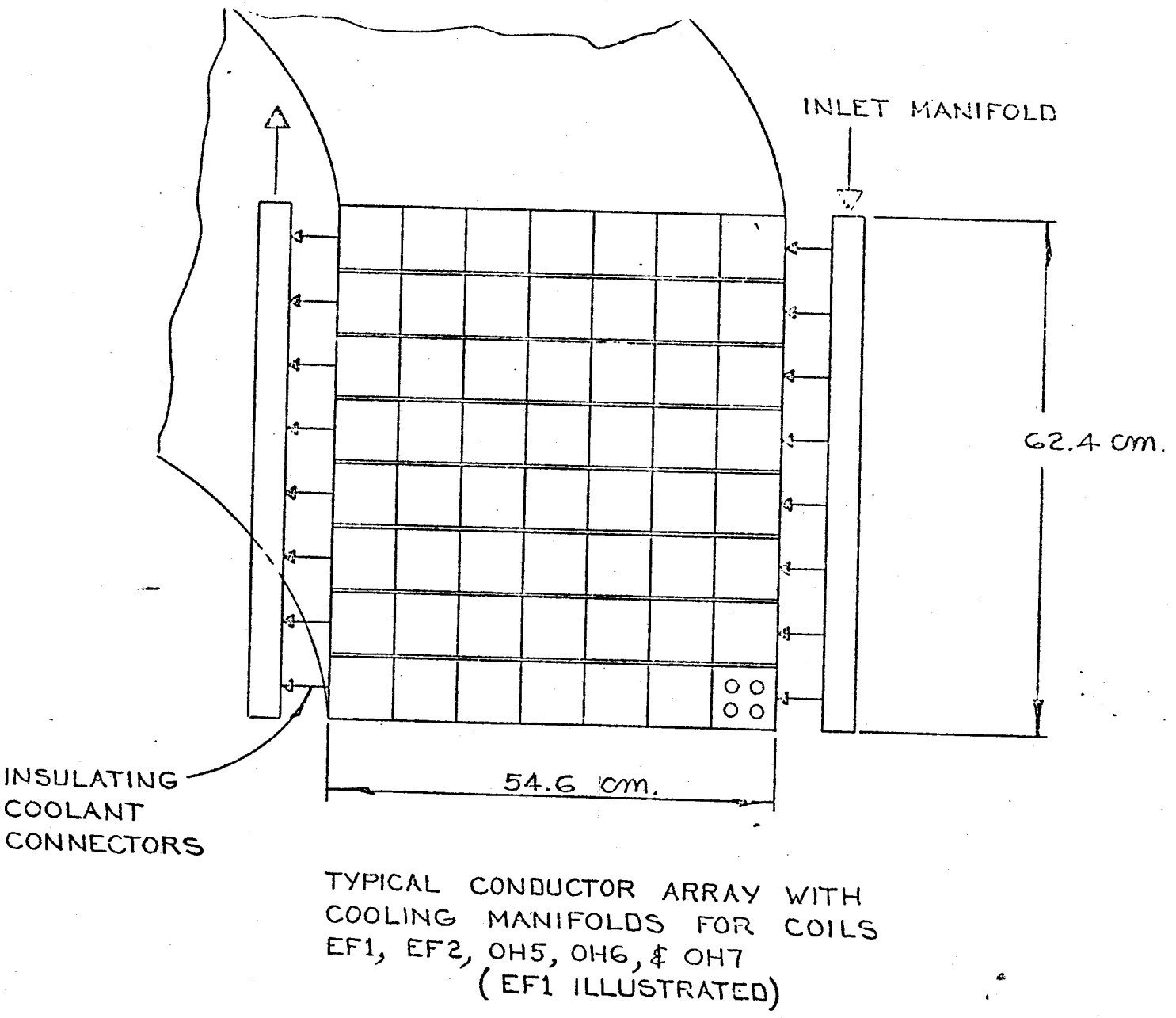

Figure 3.3.12 Arrangement of Conductors in EF1 Coil, Showing Manifolding and Coolant Flow Paths

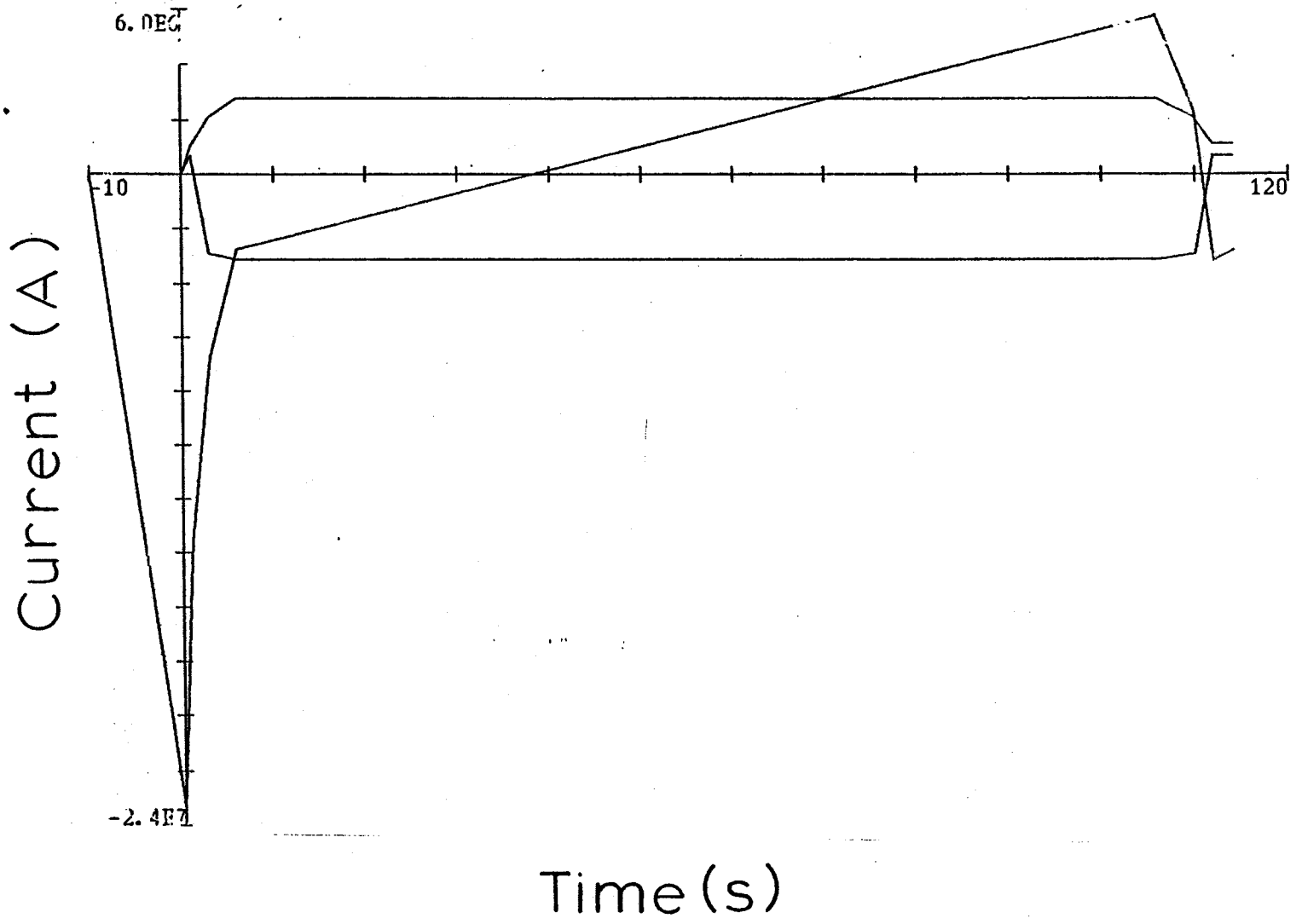

Figure 3.3.13 Typical Waveform of the Currents in the Main (I_1) and Shaping (I_2) Equilibirum Field Coils, and in the OH Transformer (I_{OH}).

3.4 The Ohmic System

The ohmic system in a resistive coil reactor can be made significantly different from that of a superconducting reactor, mainly because of the absence of peak field limitation in superconducting OH systems. However, peak resistive losses can be significant, implying large cooling requirements unless the ohmic transformer is not double swung. In this section, the characteristics of the system are described for fixed toroidal field coil and plasma requirements. The high performance case of $P_{wall} = 4.0$ MW/m^2 is analyzed because of the larger requirements.

3.4.1 Parametric Study of the OH Main Solenoid

The plasma requirements have been determined in section 2. The most important parameters are compiled in Table 3.4.1.

The plasma requires 45 V-s for the whole pulse. The EF system delivers approximately 11.5 V-s leaving 34 V-s to be generated by the ohmic heating transformer. Of this 34 V-s, 10 V-s are required for the 20-s flat top of the plasma. The ohmic transformer has to deliver 23 V-s during initiation and 10 V-s during burn.

There are two parameters in the OH system that can be made to vary: the bias, and the inner radius of the OH transformer. The bias is determined from power dissipation considerations during the burn of the plasma. Full double swing reduces the requirements during start-up but increases the power dissipation during burn. Also, of course, it considerably reduces the peak stresses. In order to analyze the tradeoffs, requirements of the OH transformer have been calculated as a function of the bias. Table 3.4.2 shows the requirements both at initiation, at the end of burn and the average dissipated power (necessary for cooling calculation). It is assumed that the transformer is at $T \approx 35$ C and that the inner radius of the OH transformer is $R_{1,\mathrm{OH}} = 0.40$ m.

It is clear from Table 3.4.2 that some bias is advantageous. The peak requirements at initiation are drastically reduced if

$$\Delta = \frac{B_{oh,\text{end of burn}}}{B_{oh,\text{prior to initiation}}} < 0.$$

However, if $\Delta \approx -1$, (double swing), the average resistive power of the magnet is increased (and so are the cooling requirements). More importantly, the stored energy at the end of the pulse is increased, and this requires larger power supplies for the shut-down of the plasma. $\Delta \approx -0.6$ is a compromise between the initiation requirements and the average and termination requirements.

Table 3.4.3 shows the tradeoffs between stored energy, peak field in the transformer, resistive power and peak stresses in the OH transformer as functions of $R_{1,OH}$, the inner radius of the transformer. As the inner radius of the transformer decreases, the stresses and dissipative power decrease at the expense of an increase in the stored energy (therefore inductive power) and field. Because the inductive power is significant, the inner radius of the OH transformer should be as large as possible. At peak field, the OH transformer would have about the same number of pulses as the TF coil, therefore, the peak stresses in these systems can be approximately the same. The inner radius of the transformer is then $R_{1,\text{OH}} = 0.40$ m.

Figure 3.3.10 shows a typical waveform of the ohmic transformer current when $\Delta = 0$ for the high performance case.

The total OH requirements for base case operation are reduced from those of high performance operation due to decreased plasma LI requirements (see Table 3.4.1). Table 3.4.4 shows the equivalent of Table 3.4.2 for the base case for a burn time of $\tau_{burn} = 300$ s. Note that the peak requirements in the base case are larger than those of the high performance operation due to the increased burn time.

3.4.2 Illustrative Desing of the Induction Coil System

The induction coils of FED-R2 must provide up to 35 V-s of flux swing in order to maintain ignited current drive for 100 seconds. To meet these various conditions induction coil system has been designed in which the flux swing is from a high forward field to zero or low reverse field and in which the induction coil can be cooled in a manner matching the condition.

The OH coil system is shown in Figure 3.4.1. It consists of seven coil pairs, each coil being mirrored in the median plane of the machine. The system consists of four drive coil pairs (OH 1,2,3 & 4 of Figure 3.4.1) and three guiding coil pairs (OH 5,6,7). The drive coils are cooled either by liquid nitrogen or by water and the guiding coils are water cooled. The flux swing is generated primarily by the drive coils. The guiding coils reduce the field everywhere in the plasma to very low values and to zero at three points. The general parameters of all the OH coils are given in Table 3.4.5.

The main drive coil, OH1, consists of a series of 50 pancake coils, each 5 cm wide and having 10 turns (see Figure 3.4.2). The coil is wound with hollow conductor which allows cooling by water or a cryogen (high pressure helium or liquid nitrogen). Because the OH system is bias is -.06, that is, the field falls from 18.7T to -11.2T during the pulse, the mean power dissipation is low.

Table 3.4.6 lists the global characteristics of the conductor system. Because the peak stored energy of the induction system is large, 620MJ, a long charge time must be used if the power source is not to be excessively large. However, the size of the power source is dictated by dissipation as well as stored energy and at room temperature, that is, 110 MW. (The average dissipation power over the pulse is, however, 18.3 MW.)

The average heat transfer rate from copper conductor to coolant (either water or cryogen) is low even though the peak rate is high. Thus the pumping requirements are modest.

The forces and stresses in the OH coils are of two kinds; self generated hoop tension and axial compressive stresses and inter-coil forces. These are listed in Table 3.4.7. There is a strong interaction between the OH and EF coils, particularly between EF2 and OH7 and EF1 and OH5. The former interaction has been computed. The major effect is the inwardly directed force on the OH coil (and of course the equal reaction on the EF coil). The forces do not however, produce severe hoop stresses. There is also an axial reaction which requires structural ties between the coils. In the matter of maintenance, coils OH7 and EF2 must be raised (or lowered) in order that a TF sector be removed. Because of the need to tie these coils together, they would be moved as a unit.

The stresses developed in coil OH1 are roughly as for an infinite coil because coils OH2,3 and 4 guide the field lines so that radial flux density in OH1 is low. Provided the interturn insulation in the pancakes of OH1 is thin (as assumed it is 1 mm) the hoop stress in the coil is only 152 MPa. However, if that insulation is thick or soft, the hoop stress will approach 306 MPa. Because the radial stress is low the von Mises stress is close to 152 MPa also.

References

[1] MONTGOMERY, D.B., The ALCATOR Project, Francis Bitter Mational Magnet Laboratory NML Report (September 1974)

[2] WEGGEL, C., HAMBURGER, W., MONTGOMERY, B., PIERCE, N. in *Proceedings of the Seventh Symposium on Engineering Problems of Fusion Research*, Knoxville, Tn (1977)

[3] WILLIAMS, J.E.C., BECKER, H.D., BOBROV, E.S., BROMBERG, L., COHN, D.R., DAVIN, J.M. and EREZ, E., MIT Plasma Fusion Center Report PFC/RR-81-24(1981)

[4] COHN, D.R., BROMBERG, L., WILLIAMS, J.E.C., BECKER, H., LECLAIRE, R. and YANG, T., *Proceedings of the Third Technical Committee Meeting and Workshop on Fusion Reactor Design and Technology*, Tokyo, Japan, October (1981)

[5] KALNAVARS, J. and JASSBY, D.L., *Proceedings of the Eighth Symposium on Engineering Problems of Fusion Research*, San Francisco, Calif. (1979); KALNAVARNS, J. and JASSBY, D.L. Princeton Plasma Physics Laboratory Report PPPL 1685 (1980)

[6] J.A. Holmes, Y-K. M. Peng, and S.J. Lynch, "Evolution of flux-conseving tokamak equilibria with preprogrammd cross sections," Jour Comput Phys, 36, 35-54, 1980

[7] BROMBERG, L., D.R. COHN, N. DIATCHENKO, R. LECLAIRE, J. MEYER, and J.E.C. WILLIAMS, to be published

TABLE 3.4.1

Plasma Inductive Requirements

	$P_{wall} = 1.0$ MW/m^2	$P_{wall} = 4.0$ MW/m^2
$(LI)_{plasma,max}$ (Weber)	25.2	35.7
Φ_{res} (Weber)	7.2	10.1
burn time (s)	100	100
T_{eo} (keV)	7.5	7.5
$\Phi_{EF,max}$ (Weber)	8.1	11.4
Φ_{OH} (Weber)	24.3	34.4

TABLE 3.4.2

Characteristics of the Ohmic heating Magnet

as a function of

the bias in the OH System

$$\Delta = \frac{B_{oh,end\ of\ burn}}{B_{oh,prior\ to\ initiation}}$$

Δ	0.0	-0.15	-0.3	-0.45	-0.6	-0.75	-0.9
$\sigma_{oh,init}$ (Pa)	5.36E+8	4.05E+8	3.17E+8	2.55E+8	2.09E+8	1.75E+8	1.48E+8
$I_{oh,init}$ (A)	4.75E+7	4.13E+7	3.66E+7	3.28E+7	2.97E+7	2.72E+7	2.5E+7
$B_{oh,init}$ (T)	29.9	26.0	23.0	20.6	18.7	17.1	15.7
$P_{oh,init}$ (W)	2.81E+8	2.13E+8	1.67E+8	1.34E+8	1.1E+8	9.19E+7	7.8E+7
$E_{oh,init}$ (M)	1.6E+9	1.21E+9	9.45E+8	7.6E+8	6.24E+8	5.21E+8	4.42E+8
$\sigma_{oh,final}$ (Pa)	0.0E+0	9.11E+6	2.85E+7	5.16E+7	7.53E+7	9.84E+7	1.2E+8
$I_{oh,final}$ (A)	0.0E+0	-6.2E+6	-1.1E+7	-1.47E+7	-1.78E+7	-2.04E+7	-2.25E+7
$B_{oh,final}$ (T)	0.0	-3.89	-6.89	-9.27	-11.2	-12.8	-14.1
$P_{oh,final}$ (W)	0.0E+0	4.79E+6	1.5E+7	2.71E+7	3.96E+7	5.17E+7	6.31E+7
$E_{oh,final}$(J)	0.0E+0	2.72E+7	8.5E+7	1.54E+8	2.25E+8	2.93E+8	3.58E+8
$P_{oh,average}$ (MW)	19.8	10.8	10.0	13.2	18.3	24.4	30.3

TABLE 3.4.3

Ohmic Heating System Characteristics vs $R_{1,OH}$

with $\Delta = -0.6$

$R_{1,OH}$ (m)	σ_{OH} (MPa)	$E_{OH,max}$ (MJ)	$I_{OH,max}$ (MA)	$P_{OH,res,max}$ (MW)	$B_{OH,max}$ (T)
71.5	634.	418.	19.2	302.	12.1
64.0	361.	46E.	21.2	175.	13.3
56.4	274.	507.	23.5	136.	14.8
48.9	234.	559.	26.1	119.	16.4
41.4	212.	613.	29.1	111.	18.3
33.9	199.	671.	32.5	108.	20.4
26.3	191.	728.	36.2	107.	22.8
18.8	184.	781.	40.4	108.	25.4

TABLE 3.4.4

Characteristics of the Ohmic heating Magnet

as a function of

$$\Delta = \frac{B_{oh,endofburn}}{B_{oh,priortoinitiation}}$$

for $P_{wall} = 1.\ \mathrm{MW/m^2}$

and $\tau_{burn} = 300\ \mathrm{s}$

Δ	0.0	-0.2	-0.4	-0.6	-0.8	-1.0
$\sigma_{oh,init}$ (MPa)	676.	470.	345.	264.	209.	169.
$I_{oh,init}$ (MA)	53.4	44.5	38.1	33.4	29.7	26.7
$B_{oh,init}$ (T)	33.6	28.0	24.0	21.0	18.6	16.8
$P_{oh,init}$ (MW)	355.	247.	181.	139.	110.	88.
$E_{oh,init}$ (GJ)	2.02	1.4	1.03	0.788	0.622	0.504
$\sigma_{oh,final}$ (MPa)	0.0	18.8	55.2	95.1	134.	169.
$I_{oh,final}$ (MA)	0.0	-8.9	-15.3	-20.	-23.7	-26.7
$B_{oh,final}$ (T)	0.0	-5.59	-9.59	-12.6	-14.9	-16.8
$P_{oh,final}$ (MW)	0.0	9.87	29.	50.	70.2	88.8
$E_{oh,final}$ (GJ)	0.0	0.056	0.165	0.284	0.398	0.504
$P_{oh,average}$ (MW)	41.5	17.4	12.0	14.5	20.2	27.2

TABLE 3.4.5

OH Coil System - Coil Parameters

(1) Coil #	(2) Amp Turns MA	turns	Inner Radius m	Outer Radius m	Z_1 Coordinate m	Z_2 Coordinate m	Peak Copper Current Density $kAcm^{-2}$	Peak Field Tesla
1	18.63	500	0.5	1.0	0	1.25	1.675	18.3
2	3.726	100	0.65	1.15	1.25	1.50	1.675	
3	3.726	100	.85	1.35	1.50	1.75	1.675	
4	3.726	100	1.05	1.55	1.75	2.0	1.675	
5	0.04	1	2.25	2.5	2.25	2.5	.894 (3)	
6	1.53	41	3.5	3.75	2.25	2.5	.894 (3)	
7	0.24	6	4.5	4.75	1.5	1.75	.894 (3)	1.26 (4)

(1) One half of a mirror image system.

(2) The system operates with all coils in series at a peak current of 37.26 *kA*. The amp-turns indicated are those computed to generate the required fields and flux. The product of turns and actual operating current differs slightly from values computed from plasma MHD requirements.

(3) Based on EF coil conductor.

(4) Field due to EF2 at peak current.

TABLE 3.4.6

OH Coil System - Global Parameters

Peak flux	33.5 V-s
Peak field strength	18.7 T
Peak current	37.26 kA
Inductance	1.39 H
Stored energy	968 MJ
Charging voltage	5.18 kV
Discharge voltage	25.9 kV

Water Cooling (coils 1,2,3,4)

Peak dissipation	105.8 MW
Average dissipation (110 secs)	12.2 MW
Average heat flux (coils 5,6,7)	4.4 Wcm^{-2}
Peak dissipation	14.3 MW
Average dissipation (110 secs)	1.5 MW

Liquid Nitrogen Cooling (coils 1,2,3,4)

Peak dissipation	18.3 MW
Average dissipation (110 secs)	2.1 MW
Average heat flux	0.8 Wcm^{-2}
Temperature at end of pulse, no cooling	87 K

TABLE 3.4.7

OH Coil System - Force and Stresses

OH1

Peak inner hoop tension (floating shell)	306 MPa
Peak inner hoop tension (radial support)	152 MPa
Pean radial pressure on insulation	4.6 MPa

OH7 forces due to peak current in EF 2:

Axial force	4.08 MN
Radial force	-7.79 MN

OH7 forces due to OH system at peak current:

Axial force	~0
Radial force	+0.19 MN

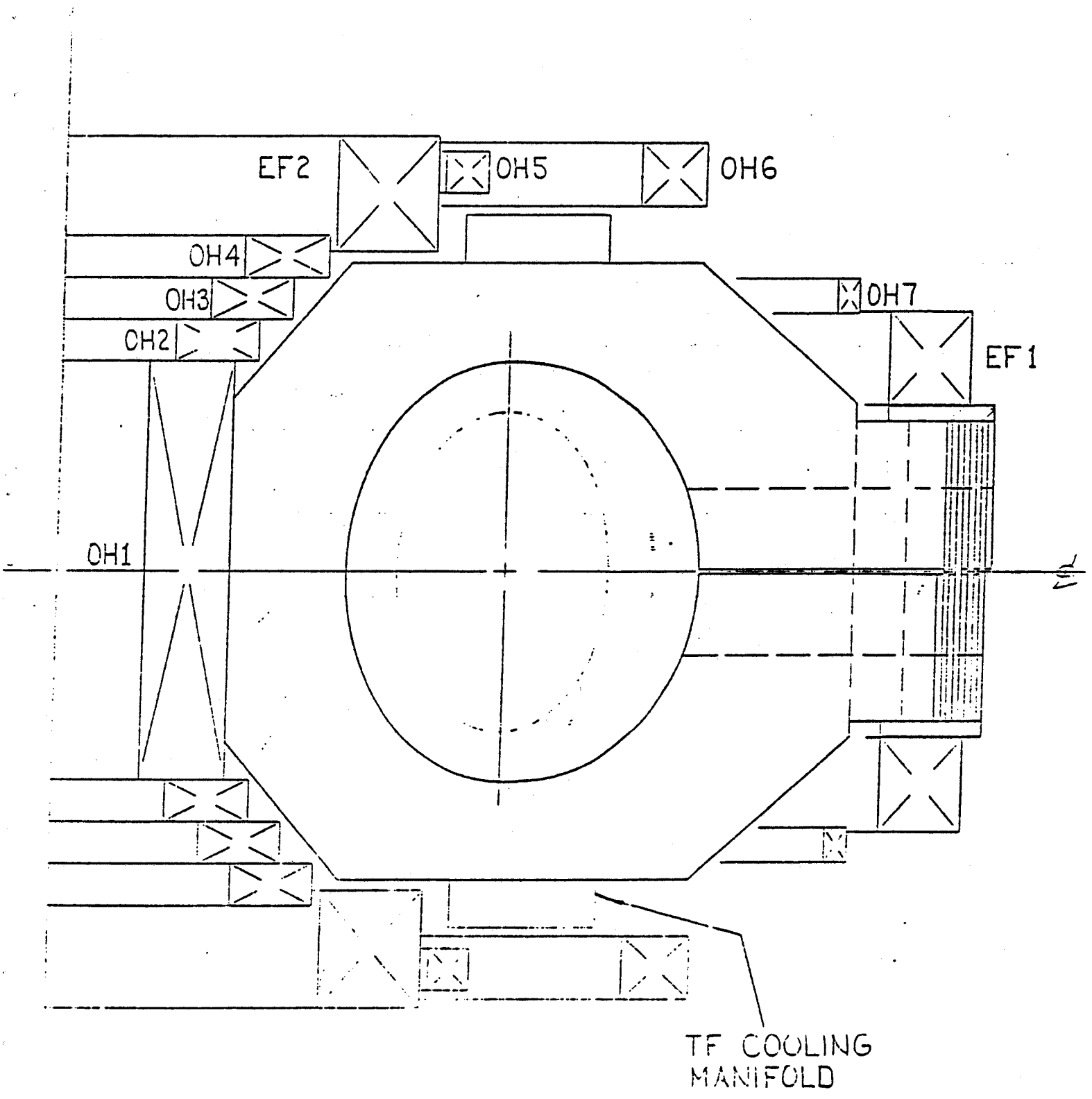

Figure 3.4.1 Positions of OH Coils 1,2,3 & 4 Relative to TF & EF Coils

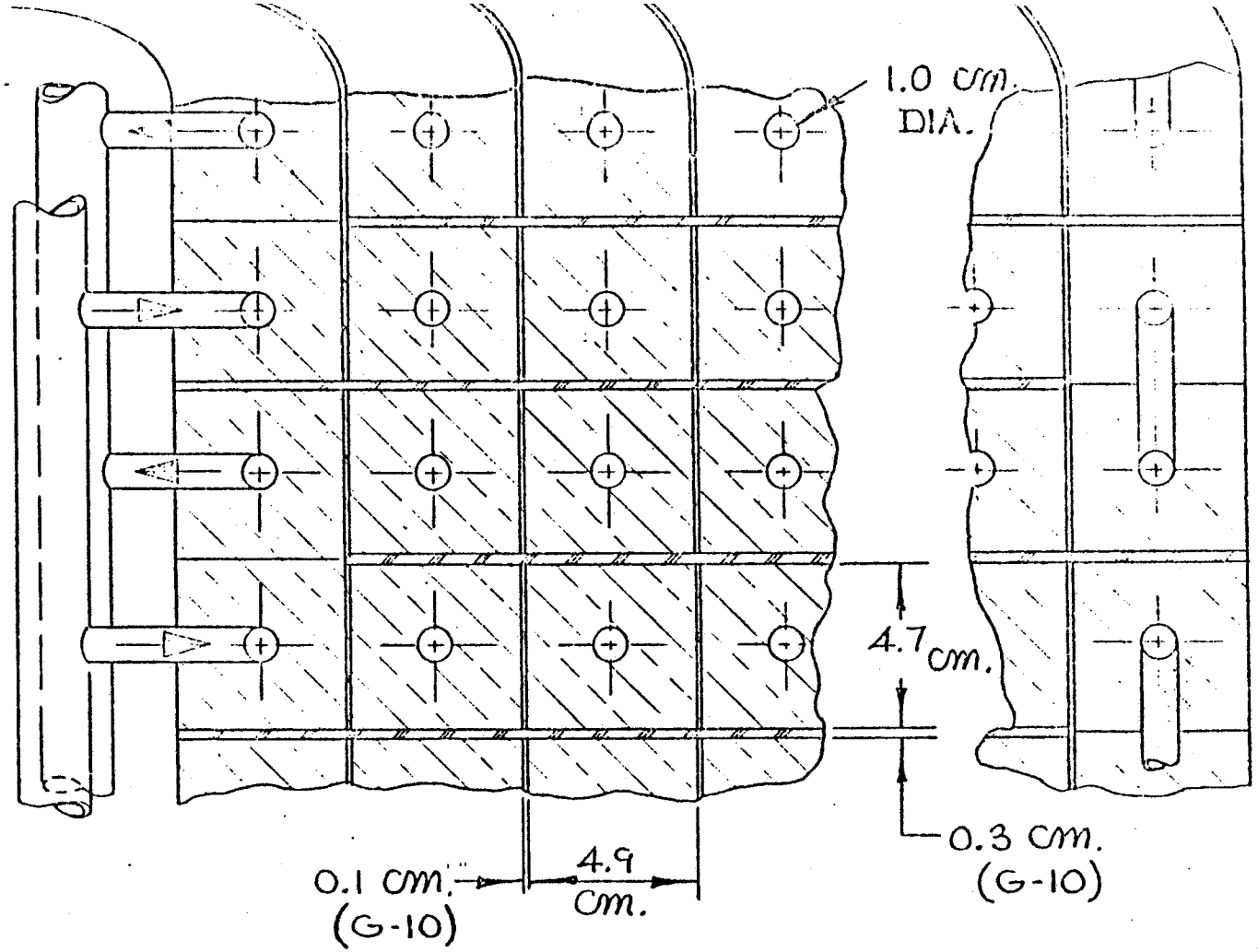

TYPICAL CONDUCTOR ARRAY WITH COOLING MANIFOLDS FOR COILS OH1, OH2, OH3, & OH4

Figure 3.4.2 Cross Section of OH Coil Showing Hydraulic & Electrical Paths - Note Manifolds Within Bore

4. MAGNET STRUCTURES ENGINEERING

4.1 Summary

The structures engineering effort on the FED-R2 magnet indicates adequate structural integrity. The critical regions are the throat and the zone around each port.

The activities involved examination of the following:

1. Identification of material structural design criteria and measured properties, (this section).
2. Stresses in the throat due to Lorentz forces (Section 5).
3. Load transfer between copper and reinforcing steel at neutral beam ports and within a turn (Section 5).
4. Constraint of torsion due to the Lorentz interaction between toroidal current and poloidal field (Section 5).
5. Thermal stresses in the throat due to joule heating in the copper (Section 5).

This section summarizes the magnet structural consideration and the materials data.

4.2 Introduction

4.2.1 Basic Structural Design Philosophy

The purpose of the structures engineering effort has been to generate a configuration that appears capable of satisfying the mechanical requirements of the magnet in a manner consistent with the physics goals. Problem areas were identified to which solutions have been found that meet the basic philosophy.

As a result of the design studies, it is possible to claim that the current configuration appears structurally feasible for the intended FED-R2 mission. (The design has not been optimized). Also, there are areas that will require further study during the detail design phase, such as the regions around the ports.

The design of the copper conductor in each plate is dictated primarily by electrical needs and the forces in the throat. The steel transmits vertical and radial forces between upper and lower magnet halves at the outer boundary and is THE primary support of the torsonal loading.

4.3.3 Design Constraints

The magnet structure must clear the vacuum vessel. It cannot encroach on the cylindrical space for the ohmic heating coil. The vertical dimensions offer relative freedom of choice, as does the outer radius. However, fabricability, handling and cost dictate the desire for as small a size as possible.

The sixteen ports restrict the space available for structural material at the outer boundary of the magnet. Similar restrictions exist at the 16 flanges that contain the ports. Support of the vacuum vessel also affects design details of those flanges as well as the 16 split closure flanges.

There are structural complications from the presence of the ports and the cross-over copper turns which cause deviations in the load paths from the top of the magnet to the bottom.

4.4 General Structural Requirements of the Magnet

The structural requirements arise from the physics performance demands on the system. The toroidal field at the radius of the compressed plasma dictates the magnitude of the inplane Lorentz forces and the poloidal field controls the torque to be applied to the TF coil. The plasma behavior generates the radiant flux spectrum and fluence. The pulse leads to temperature fields as a function of space and time: however, these have not been analyzed in detail.

The geometric constraints on the coil are reflected in the magnetic field distribution which, in turn, interacts with the current pattern to produce the Lorentz forces. Consequently, the TF coil serves the dual function of providing a magnetic field and resisting the forces produced by it.

The magnet structure must be capable of withstanding 1000 cycles at full field and 5000 cycles at 2/3 full field. There will be 10 cycles of poloidal field for each cycle of toroidal field. The minimum fatigue factor of safety shall be 4 based on life. The applied stresses shall include those induced by thermal gradients.

Survivability entails resistance of the structural materials to damage from an anticipated fluence of 10^{20} neutrons per square centimeter and 10^{11} rads of gamma radiation.

Fabrication of the magnet involves erection loads that must be withstood without compromising structural integrity. It also must be possible to perform maintenance by remote control for repair and general tuneup of the system.

4.5 Magnet Structure (See Section 5 for related figures)

The magnet is an array of 384 copper BITTER plates slit in the median plane at the outer boundary current path. Steel plates in that vicinity transmit vertical forces between upper and lower magnet halves between ports and adjacent to ports where the copper plates are split. Keys are inserted between plates to provide shearing capacity for that purpose. The circumferential stress at the outer boundary is too small in compression to generate frictional shear for load transfer.

The keys also transmit shears induced by poloidal loading on the magnet. Calculations indicate that virtually all torque is resisted by the outer leg.

Consideration was given to the use of outer boundary backing rings as in ALCATOR and ZEPHYR. That concept was set aside for this preliminary design, however, because of the difficult maintenance problem. The use of cement, for shear strength, also was considered and set aside on the grounds of uncertain reliability. However, it is retained as an assembly procedure.

Hardened copper plates would be welded to form each Bitter plate. The high von Mises stress in the coil (relative to the yield strength of copper at a weld), is expected to be circumvented by the arrangement shown in Figure 3.1.2. The copper plates would be keyed to the steel plates for load transfer as mentioned above.

The thin grp (glass reinforced plastic) insulator material prevents shorts and breakdowns between adjacent plates. Consequently, it is subjected to mechanical as well as electrical stresses. Only the mechanical behavior is discussed in this report. However, a preliminary study indicates that the insulator resistance will be satisfactory to the end of the design life of the magnet.

4.6 Materials Structural Design Criteria

FED-R2 is purely for research purposes. It will not be a prototype for a power producer. In that context, it was decided to base the structural reliability analysis on two criteria: the stress intensity shall not exceed the elastic limit at any location and there shall be a fatigue life safety factor of 4. In the absence of fracture mechanics data, it was not possible to conduct a meaningful crack growth analysis. However, the large reduction in area of cold worked oxygen-free copper is taken as an indication that crack growth from small flaws would not be a problem.

The philosophy has been translated into the following relations for allowable stress, the lowest value of which shall govern the design:

1. 3/4 of the 0.002-strain-offset yield strength for primary membrane loads on metallic components and 1/3 of the ultimate compression strength for grp composites.
2. The yield strength for primary bending or combined bending and membrane stress.
3. Two times the membrane allowable stress for combined membrane, bending and thermal stress. The damaging effect of nuclear radiation shall be included in selecting allowable stresses.
4. The cyclic stress (with $R = 0$) from the best available notched-plate fatigue data, for 4-times the anticipated number of operating cycles. Miner's criterion will be used for combined load levels with the cycle ratio sum equal to, or less than, 1/4 (A crack propagation criterion also should be used when sufficient data become available for copper and grp composites.)

4.7 Material Properties

The basic copper in TF coils is 60 percent cold worked oxygen free. At 100 F or 38 C, (a reasonable mean upper value for the expected temperature range), the yield tensile strength is 46 ksi (320 MPa) and the tensile ultimate is 50 ksi (345 MPa). Reduction in area is 75 percent. A representative notched fatigue curve is shown in Figure 4.1.

For a typical high strength stainless steel plate, the ultimate tensile strength is 160 ksi (1100 MPa) and the yield strength is 93 ksi (60 MPa). Actually, the applied stresses are well below those values so the steel is not a critical item.

Compression fatigue data for irradiated G-10CR sheets appear in Figure 4.2 from section 6. The dose is in excess of 10^{11} rads, equivalent. The ultimate compression strength at RT is typically 60 ksi (414 MPa) for irradiated G- 10CR.

4.8 Allowable Stress

On the basis of the design criteria and material properties, the allowable stresses of the magnet materials are also shown in Table 4.1.

Figure 4.1 - Notched Fatigue Curve Unirradiated Oxygen Free Copper, 60 Percent Cold Work

Maximum Stress Shown
Minimum Stress = 0

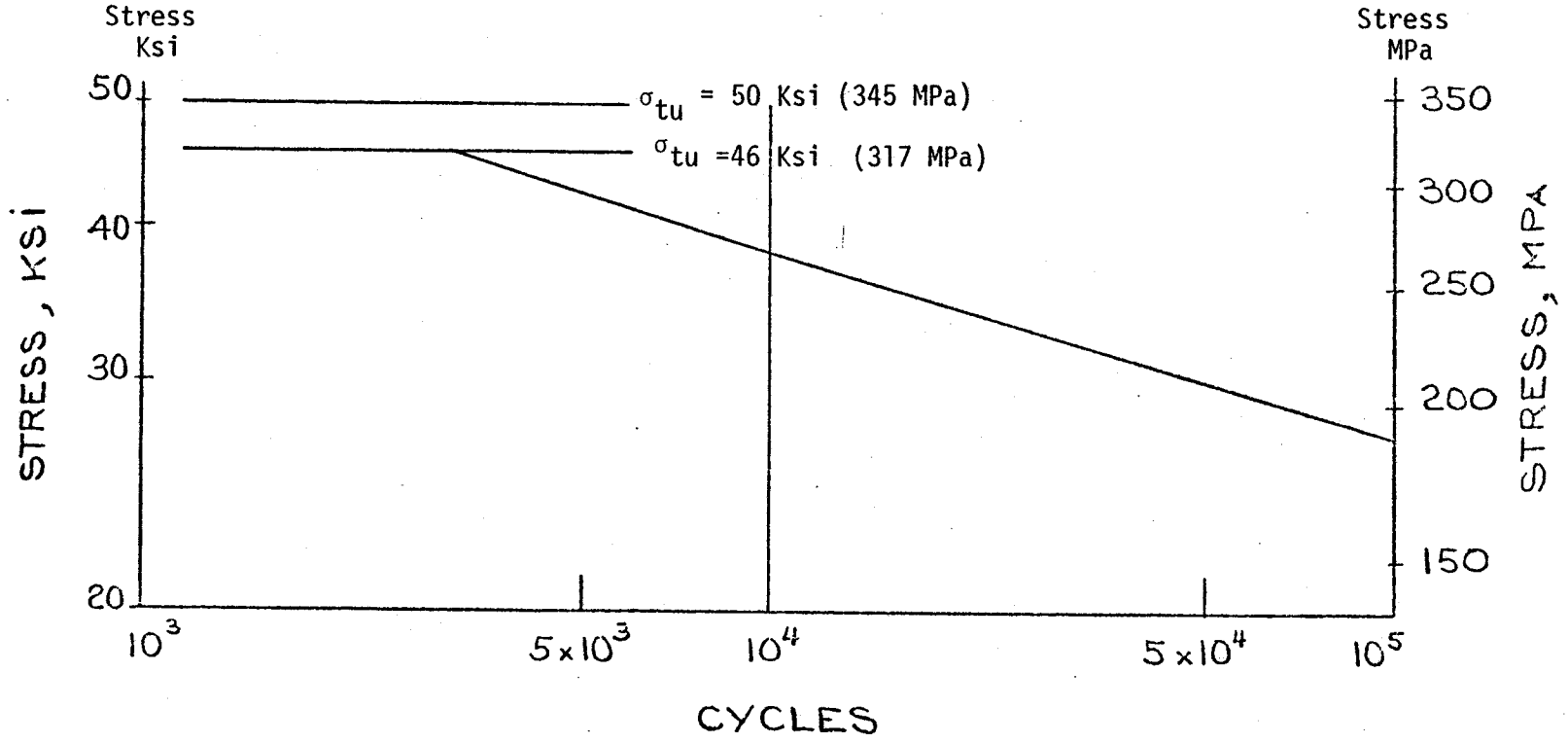

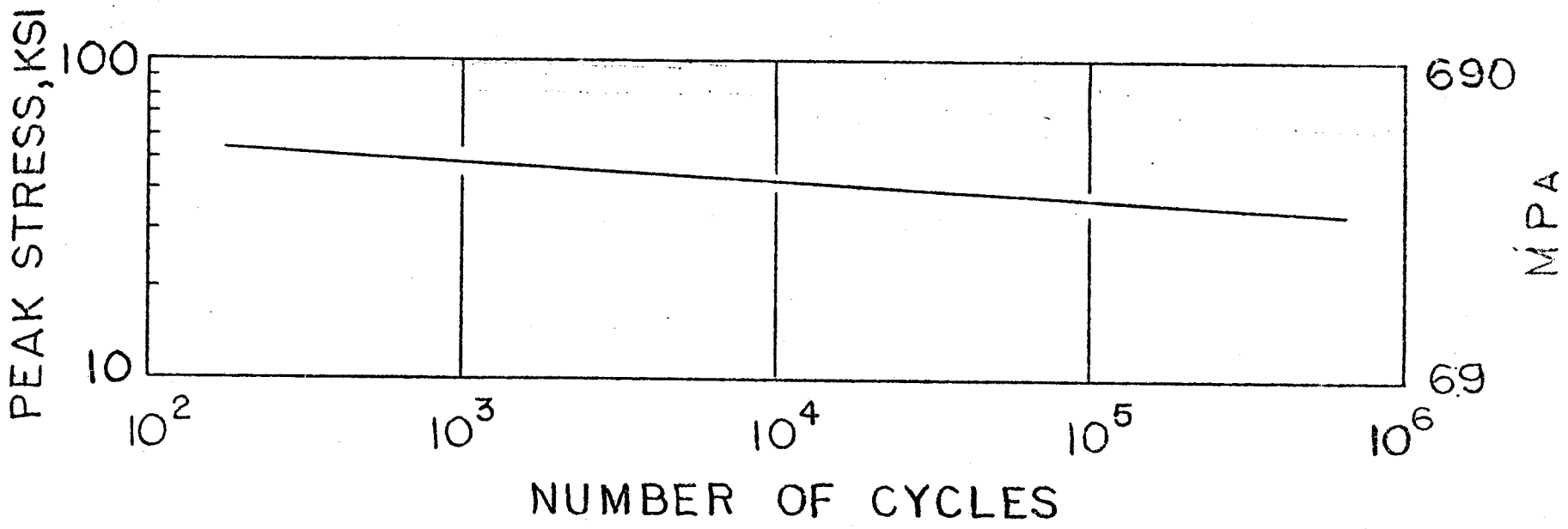

Figure 4.2 - Irradiated G-10 compression fatigue test data. Fluence = 10^{11} Rads Equivalent.

Table 4.1

Room Temperature Material Allowable Stress, MPa

Material	Membrane	Membrane + Bending	Fatigue
copper, 1/4 hard	240	320	NA
steel	480	640	figure 4.2
fiberglass, (polyimide + S glass)	138	NA	figure 6.2

5. STRESS ANALYSIS

5.1 Introduction

The final design of the FED-R2 is the result of extensive computerized structural optimization of the toroidal field magnet dimensions and materials. The parameters under variation included the major and minor radii of the plasma, inner and outer major radii of the magnet, the bore scrape-offs, plasma elongation, the height of the magnet and the amount of steel reinforcement. The analysis included evaluation of plasma parameters, power consumption, plasma heating and cooling of the resistive magnet.

It was decided that at the current stage of the design finite element analysis of the magnet structure is not justified. However, the thick shell theory computer codes developed at MIT and described in the Appendix provide sufficient analytical data for structural evaluation. Therefore, all the optimization studies as well as the final stress analysis were performed on the basis of that theory.

Described in the Appendix are the basic equations of the theory of thick orthothropic toroidal shells acted upon by in-plane and out-of-plane Lorentz forces and thermal loads, and the computer codes which implement the theory numerically.

5.2 Structural Assembly (See Section 4.5)

The outer limbs of the 384 1/4 hard copper plates are cut at the midplane of the magnet to provide for the current connections between adjacent plates. This reduces substantially the load carrying capacity of the plate in this region which is compensated by the stainless steel reinforcement inserted between adjacent copper plates. A schematic plan view of the assembly appears in Figure 5.1.

The stainless steel wedges play a significant role in the load carrying capacity of the magnet structure, against the in-plane and out-of-plane forces. The keys transmit the copper plate loads to the stainless steel wedges. For this purpose slots are machined in the copper and steel into which insulated hardened copper keys are inserted during assembly and electron-beam-welded in place.

The keys are pressed into the slots machined in the stainless steel wedges, extending by 8 mm on both faces of the wedge. All keys are 9 mm wide. The key length varies with the poloidal angle according to the varying width of the TF coil. Matching slots are machined on both sides of the copper plate, into which the keys are embedded. The slots in copper are 11 mm wide and 8 mm deep which provides room for insulation.

The keys secure the interaction of the copper plates and stainless steel wedges under the action of in-plane and torsional loads applied separately or simultaneously. The shear is induced by the transfer of in-plane Lorentz forces from the copper plates to the steel wedges. They act primarily normal to the poloidal meridian of the plate-wedge system. The torsional shears are induced by the interaction of the poloidal field with the current in the toroidal coils. Those shears act primarily along the poloidal meridian with a small component normal to the meridian.

As as result of that situation, the keys are long rectangles oriented normal to the poloidal meridian. The proportions of the sides reflect the relative magnitudes of the shears flowing along and normal to the meridian.

The keys resist the shear load accumulated over the pitch between keys. The key dimensions are controlled by bearing on the height of the organic insulation and by shear across the hardened copper bar.

There is a large poloidal variation in the magnitude of the in-plane Lorentz forces being transmitted from the copper plates to the stainless steel wedges. It is computed on the basis of the contribution of copper and steel to the structural resistance. At the inner tip of the stainless steel wedge this fraction is zero and is about

76% at the middle of the outer limb. The shear from the in-plane forces is resisted by the short poloidal edges of the keys. In order to minimize this bearing pressure on the insulation, the keys are arranged in two meridional rows as shown in Fig. 5.3.

In addition to the key slots, which contribute to the weakening of the copper and steel, there are also cooling channels on one side of the copper plate. All these singularities are taken into account in the analysis, to yield the effective cross-sections of the participating structural elements.

The magnet is assembled in 16 modules each of which consists of 24 Bitter plates and stainless steel reinforcing wedges. The modules are faced with closure flanges. The presence of the closure flanges and the sixteen rectangular neutral beam port windows was taken into account in the process of computation of the effective meridional, circumferential and shear moduli of the orthotropic material of the magnet structural model.

5.3 Structural Model of the Toroidal Magnet

Initial structural studies indicated that if the outer contour of a rectangular Bitter plate is modified by cropping the corners so that the outer contour is more consistent with the contour of the magnet bore, the stress situation in the throat of the magnet improved. In addition to that, by cutting off the corners of a rectangular plate, more room is created for positioning the ohmic heating coils and the equilibrium field coils, as shown in Figure 5.4, and the weight is reduced.

The vertical radial cross-section of the toroidal magnet and the thick toroidal shell model outline are shown in Figure 5.5. The inner and outer surfaces of the shell are generated by rotation of two eccentric ellipses (A and B) about the toroidal axis $R = 0$. The computer code generates all the geometric parameters of the

midsurface of the orthotropic toroidal shell of varying thickness. These parameters include the major toroidal radii, principal radii of curvature and thickness.

5.4 Stresses in the FED-R2 Toroidal Magnet

5.4.1 Magnet Parameters

The stress analysis was performed for the toroidal magnet with the following parameters:

Magnetic flux at the plasma center	7.1 T
Plasma major radius	2.64 m
Plasma minor radius	0.63 m
Plasma elongation	1.5
Plasma-TF Coil distances	
midplane inboard	0.40m
top	0.40m
midplane outboard	0.60m
Magnet inner major radius	0.80 m
Magnet outer major radius	4.85
Magnet height	3.67 m
Current in a Bitter plate	0.244 MA

5.4.2 In-plane Lorentz Load

The stresses generated in copper under the action of in-plane Lorentz forces are shown in Fig. 5.6-5.8. Figure 5.6 presents the primary membrane and bending stresses in both meridional and circumferential directions. The meridional membrane stress is everywhere tensile and has a maximum of 111 MPa in the throat. The circumferential membrane stress is compressive between the throat and the magnet crown and tensile with the maximum magnitude of 7.8 MPa between major radii of 2.66 and 3.68 m. The maximum membrane compression in the throat is 63 MPa.

There is a substantial meridional bending in the throat region. The maximum meridional bending stress on the plasma side of the throat is 76.5 MPa. There is also bending in the circumferential direction. The circumferential bending stress in the throat region is 48 MPA which decays rather rapidly to a small value of about 3-5 MPa at toroidal radii greater than the major radius of the crown.

Figure 5.7 shows the distribution of the combined membrane and bending stresses along the magnet meridian. The maximum meridional stress (188 MPa in tension) occurs in the inner fiber of the throat. The maximum circumferential value, at the outer fibers of the thoat, is 112 MPa in compression. The meridional combined stress in the outer fiber of the throat and the circumferential combined stress in the inner fiber of the throat are small compared to the above mentioned values.

The equivalent von Mises membrane and combined stresses are shown in Figure 5.8. The maximum membrane stress is 153 MPa and the maximum combined stress is 196 MPa. Both occur in the throat.

The static load factors of safety (FS) are summarized in Table 5.1. The steel stresses are small and are not reported.

All the stresses are given for the plate situated in the middle between two adjacent ports, and as the

detailed FEM analysis for the ZEPHYR reactor showed, are the highest.

TABLE 5.1

"bfStatic Load Factors of Safety in Magnet

(Throat Region is Critical)

1000 cycles

FS =(Allowable Stress)/(Applied Stress)

Material	Allowable Stress (MPa)	Applied Stress (MPa)	FS
Copper	320	196	1.6
Insulator	138	63	2.2

5.4.3 Out-of-Plane Loads

The out-of-plane loads are antisymmetric with respect to the midplane of the toroidal system, and result in torsion. The torsion is resisted by the shear stresses which are directed tangentially to the poloidal meridian at the copper-steel interface.

The structural model of the torsional behavior of the toroidal magnet takes into account the existence of such geometric and material singularities as the access ports, closure and port flanges, key slots and cooling channels, as well as the copper discontinuity in the middle of the outer limb.

It should be emphasized that the presence of the neutral beam ports substantially reduces the shear stiffness of the structure in this region where the shear stresses are the highest. This is due to the fact that at the midplane they are resisted by the cross-section of the stainless steel wedges and flanges only.

The distribution of shear stresses along the poloidal meridian as a function of the poloidal angle is presented in Fig. 5.9. As can be observed, the maximum shear stress of 23.8 MPa occurs at the midplane, on the plasma side of the outer limb. On the opposite side of the outer limb the maximum shear stress is 16.3 MPa. They hold within the poloidal angle range corresponding with half of the port height. Above the port ceiling the shear stress decays rapidly to an average of about 6 MPa, and reduces gradually from this level to zero at the crown of the magnet.

The shear stress levels presented in Fig. 5.9 were used as the basic values for key sizing.

5.4.4 Sizing of the Keys

As mentioned above, the keys are directed normal to the poloidal meridian. The height of the key is restricted by the thickness of the parallel-faced portion of the copper plate which is 3.5 cm in this design. The height of the keys was chosen to be 8 mm, which is also the depth of the slots in the copper plate. The width of the keys is 9 mm. The pitch between the keys varies in accordance with the level of torsional shear stresses in each particular region and with the fraction of the in-plane Lorentz load being transmitted from copper to steel. The distribution of the latter with respect to the poloidal angle is shown in Fig. 5.10. The key dimensions were chosen to keep the applied copper and insulation stresses below the allowable values shown in Section 4.

There are two meridional rows of keys which have the same cross-section. Corresponding to the stress levels there are four different areas in the outer limb with four different pitches between keys. These are summarized in Table 5.2.

TABLE 5.2

Key Data

Region	Poloidal Angle Range (deg)	Pitch (cm)	Key length in each meridional row(cm)
1	0—30	16	18
2	30—50	8	30
3	50—70	5	32
4	70—90	2.8	30

ORIENTATION coincides with the radius of curvature of the poloidal meridian.

Key width - 9 mm (TYP)

Key height - 8 mm (TYP)

Insulation thickness - 1 mm

5.5 Thermal Stress

Thermal stresses were calculated on the conservative assumption that a throat region two throat-thicknesses long would be 35C hotter than the remainder of the magnet. The magnet was modelled as two infinitely long cylinders, one on each side of the ring. Figure 5.11 depicts the configuration.

The computation was performed using ring-cylinder interaction theory. It indicated a toroidal bending stress of 117 MPa. This would cause no problem if the design criteria of Section 4 are assumed to apply to the combination of thermal and Lorentz stresses.

5.6 APPENDIX

Reprint 82-PVP-52, Presented at ASME Meeting in Florida.

ANALYSIS OF TOROIDAL MAGNET SYSTEMS ON THE BASIS OF THE REISSNER SHELL THEORY

E.S. Bobrov, J.H. Schultz
Francis Bitter National Magnet Laboratory
Plasma Fusion Center
Massachusetts Institute of Technology
Cambridge, Massachusetts 02139

ABSTRACT

A method for analyzing the structural behavior of toroidal magnet systems subjected to Lorentz forces both in and out of the winding planes, and thermal loads is considered in this paper. The toroidal coil assembly is treated as a finite thickness, orthotropic, rotationally symmetric shell of revolution acted upon by symmetrical and antisymmetrical loads. The equations based on Reissner's shell theory are derived, and numerical solutions are presented. The method is an efficient design tool for the analysis and shape selection of toroidal magnet systems and their structures, such as the in-plane and out-of-plane load support systems for closed magnetic confinement machines, e.g. tokamaks, stellarators, and bumpy tori.

NOMENCLATURE

B_t	toroidal magnetic field, T
B_v	vertical magnetic field, T
E_1, E_2, E_3	Young's moduli, N/m^2
F_z	vertical force, N
G_{12}, G_{13}, G_{23}	shear moduli, N/m^2
h	shell thickness, m
I	electric current, A
M_1, M_2, M_{12}, M_{21}	stress couples, Nm/m
N	number of toroidal turns
N_1, N_2, N_{12}, N_{21}	membrane stress resultants, N/m
Q_1, Q_2	transverse shear resultants, N/m
q_2, q_3	distributed shear and normal loads, N/m^2
r_1	toroidal radius, m
R_1, R_2	principal radii of curvature of middle surface, m
S	distance measured along the meridian, m
T, T_o, T_1	temperature increment and temperature resultants, °C
u,v,w	components of midsurface displacement, m
z	midsurface normal coordinate
α_1, α_2	coefficients of thermal expansion
β_1, β_2	angles of midsurface rotation
$\gamma_{12}, \gamma_{13}, \gamma_{23}$	shear strains
$\gamma_{13m}, \gamma_{23m}$	effective transverse shear strains
$\varepsilon_1, \varepsilon_2, \varepsilon_3$	axial strains
$\varepsilon_{1m}, \varepsilon_{2m}, \varepsilon_{12m}$	effective midsurface strains

Contributed by the Pressure Vessel & Piping Division of the ASME.

θ	tangent of angle of meridian
$\kappa_1, \kappa_2, \kappa_{12}$	effective midsurface curvature changes
μ_o	magnetic permiability of vacuum, H/m
$\nu_{12}, \nu_{13}, \nu_{23}$	Poisson's ratios
$\sigma_1, \sigma_2, \sigma_3$	axial stresses
$\tau_{12}, \tau_{13}, \tau_{23}$	shear stresses
ϕ	equatorial coordinate
Ω	Lagrangean multiplier function

INTRODUCTION

This paper presents equations of orthotropic, rotationally symmetric toroidal shells of finite thickness subjected to symmetrical and antisymmetrical loads, including thermal loads. These equations were derived using the approach developed by E. Reissner (1) that allows to take into account the effect of transverse stresses on the deformation of the middle surface of the shell and consistently omit terms which are small of order h^2/R^2.

The equations are used to model the structural behavior of discrete and continuous toroidal field (TF) magnet systems subjected to in-plane and out-of-plane Lorentz forces and experiencing orthotropic thermal expansion or contraction.

The utilization of the theory of orthotropic shells of finite thickness for the structural analysis of the TF magnet systems is found to be very efficient, particularly in the process of initial shape selection.

The earliest and the most popular TF coil configuration, known as the Princeton D shape, was first derived in (2) by considering the equilibrium of a plane filament in pure tension subjected to a distributed normal load inversely proportional to the toroidal radius. The inner leg of this coil is supported by a stiff cylinder to react the unbalanced centering force. As shown by several authors (3-5) substantial bending stresses are revealed by detailed analyses of TF magnet structures designed to follow the pure tension trajectory. Large bending stresses were also found in the compound-constant-tension coil configurations derived in (6). These bending stresses were partially explained by several factors, including the finite thickness of the coils in real tokamak structures(7), nonuniformity of the toroidal field due to the discrete character of coil placement(8) and the violation of the compatibility conditions at the joining points of different "pure tension" shapes (9). Almost no consideration was given to the effect of the intercoil structure (to support the out-of-plane loads) on the coil shapes.

An important contribution in the modelling of toroidal magnet systems was the membrane shell model developed by Gray et al (10) which took into consideration the circumferential stiffness of the magnet assembly. A bending free membrane shell shape was derived. It was substantially different from that of a constant tension filament. Unlike the significant shape deviations described in (11) and (12), the deviation from the D trajectory happens in the membrane shell consideration naturally, independent of reaction forces or finite thickness effects. Unfortunately, there is an inherent strain incompatibility at the crown of a toroidal shell in the solution to the linear membrane theory (13). This incompatibility introduces bending stresses in a shell with finite bending stiffness, as demonstrated below.

This analysis and design studies (14) call into question the entire approach of searching for an optimal shape to minimize bending stresses. The analysis presented in this paper shows that typical tokamak reactor designs (14) with sufficient structural case material to withstand tensile stresses have sufficient bending stiffness to react the bending stresses, which were found to be less than 50% of primary membrane stresses, for the two shapes considered. Furthermore, design studies (14) of high-cycle, inductively driven tokamaks showed that case thicknesses were dominated by pulsed out-of-plane loads. The possibility of low-cycle operation for all the major toroidal confinement systems requires a capability for the rapid scoping of complex interrelated structural and physics trade-offs which is substantially advanced by the inclusion of the out-of-plane load induced stresses in the model described below.

BASIC EQUATIONS

Following E. Reissner(1) we derived a basic set of equations of rotationally symmetric orthotropic shells of revolution of finite thickness. The equations take into account the effect of transverse stresses on the deformation of the middle surface of the shell and retain terms of order h/R in comparison with unity. This is essential with an h/R ratio greater than 1/20. In order to distinguish the structural response of toroidal coil systems to symmetrical (normal pressure due to the toroidal field, and temperature variation) and antisymmetrical (torsional shear due to the vertical field) loads, the equations are presented in two respective groups of which the first corresponds to the symmetrical load and the second to the antysimmetrical load.

Symmetrical Load

In this case the shell is subjected to a mechanical pressure caused by toroidal field B_t

$$q_3 = \frac{\mu_o N^2 I^2}{8\pi^2 r^2}, \tag{1}$$

and rotationally symmetric temperature distribution T(s,z). The temperature distribution in the shell is accounted for in the usual manner by means of the integrated temperature effect of the form

$$T_o(s) = \frac{1}{h}\int_{-\frac{h}{2}}^{\frac{h}{2}} T(s,z)dz \tag{2}$$

$$T_1(s) = \frac{12}{h^3}\int_{-\frac{h}{2}}^{\frac{h}{2}} zT(s,z)dz \tag{3}$$

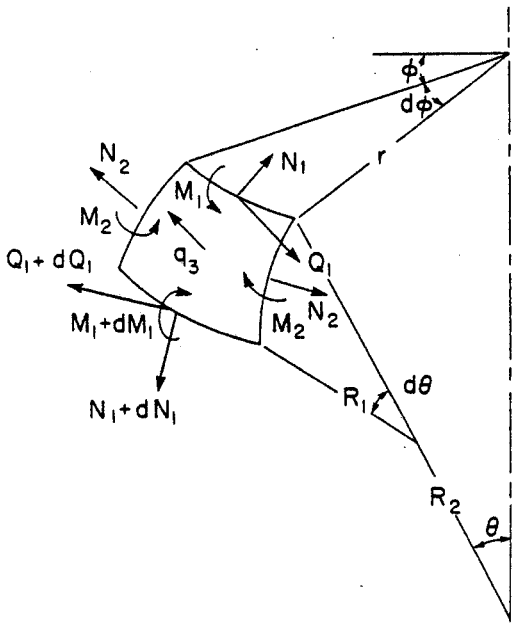

Fig. 1 Differential element of a shell of revolution under symmetric loading.

Equations of Equilibrium. Stress resultants and stress couples acting upon a differential element of the shell are in case of a symmetrical load as shown in Fig. 1. The equations of equilibrium in this case are

$$\frac{dN_1}{ds} + \frac{1}{r}\frac{dr}{ds}(N_1 - N_2) + \frac{Q_1}{R_1} = 0, \tag{4}$$

$$-\frac{N_1}{R_1} - \frac{N_2}{R_2} + \frac{dQ_1}{ds} + \frac{1}{r}\frac{dr}{ds}Q_1 = -q_3 \tag{5}$$

$$-Q_1 + \frac{dM_1}{ds} + \frac{1}{r}\frac{dr}{ds}(M_1 - M_2) = 0 \tag{6}$$

Stress-Strain and Strain-Displacement Relations. If the material of the shell is orthotropic, the following relations are true (15).

$$\epsilon_1 = \frac{1}{E_1}(\sigma_1 - \nu_{21}\sigma_2 - \nu_{31}\sigma_3) \tag{7}$$

$$\epsilon_2 = \frac{1}{E_2}(-\nu_{12}\sigma_1 + \sigma_2 - \nu_{32}\sigma_3) \tag{8}$$

$$\epsilon_3 = \frac{1}{E_3}(-\nu_{13}\sigma_1 - \nu_{23}\sigma_2 + \sigma_3) \tag{9}$$

$$\gamma_{13} = \frac{1}{G_{13}}\tau_{13} \tag{10}$$

and

$$\frac{\nu_{12}}{E_2} = \frac{\nu_{21}}{E_1}, \quad \frac{\nu_{13}}{E_3} = \frac{\nu_{31}}{E_1}, \quad \frac{\nu_{23}}{E_3} = \frac{\nu_{32}}{E_2} \tag{11}$$

The stress-strain relations for the shell are obtained by minimizing the strain energy expressed in terms of stress resultants and stress couples, with equilibrium equations (4)-(6) as side conditions, using Lagrangean multipliers.

$$\epsilon_{1m} = \alpha_1 T_o + \frac{N_1 - \nu_{21}N_2}{E_1 h} + \left(\frac{h}{R_1} - \frac{h}{R_2}\right)\frac{M_1}{E_1 h^2} + \frac{1}{E_3 h^2}\left[1.2\,\nu_{13}\frac{h}{R_1}M_1 + \left(\nu_{13}\frac{h}{R_2} + 0.2\,\nu_{23}\frac{h}{R_1}\right)M_2\right] \tag{12}$$

$$\epsilon_{2m} = \alpha_2 T_o + \frac{N_2 - \nu_{12}N_1}{E_2 h} + \left(\frac{h}{R_2} - \frac{h}{R_1}\right)\frac{M_2}{E_2 h^2} + \frac{1}{E_3 h^2}\left[\left(0.2\,\nu_{13}\frac{h}{R_2} + \nu_{23}\frac{h}{R_1}\right)M_1 + 1.2\,\nu_{23}\frac{h}{R_2}M_2\right] \tag{13}$$

$$\gamma_{13m} = \frac{1.2}{G_{13} h}Q_1 \tag{14}$$

$$\kappa_1 = \alpha_1 T_1 + \frac{12(M_1 - \nu_{21}M_2)}{E_1 h^3} + \left(\frac{h}{R_1} - \frac{h}{R_2}\right)\frac{N_1}{E_1 h^2} + \frac{1}{E_3 h^2}\left[1.2\,\nu_{13}\frac{h}{R_1}N_1 + \left(0.2\,\nu_{13}\frac{h}{R_2} + \nu_{23}\frac{h}{R_1}\right)N_2\right] \tag{15}$$

$$\kappa_2 = \alpha_2 T_1 + \frac{12(M_2 - \nu_{12}M_1)}{E_2 h^3} + \left(\frac{h}{R_2} - \frac{h}{R_1}\right)\frac{N^2}{E_2 h^2} + \frac{1}{E_3 h^2}\left[\left(\nu_{13}\frac{h}{R_2} + 0.2\,\nu_{23}\frac{h}{R_1}\right)N_1 + 1.2\,\nu_{23}\frac{h}{R_2}N_2\right] \tag{16}$$

The effective midsurface strains and midsurface curvature changes are expressed in terms of the effective midsurface linear and angular displacements u, w, and β_1

$$\epsilon_{1m} = \frac{du}{ds} + \frac{w}{R_1} \tag{17}$$

$$\epsilon_{2m} = \frac{1}{r}\frac{dr}{ds}u + \frac{w}{R_2} \tag{18}$$

$$\gamma_{13m} = \beta_1 + \frac{dw}{ds} - \frac{u}{R_1} \tag{19}$$

$$\kappa_1 = \frac{d\beta_1}{ds} \tag{20}$$

$$\kappa_2 = \frac{1}{r}\frac{dr}{ds}\beta_1 \tag{21}$$

Antisymmetrical Load

In this case the load applied to the midsurface of the shell is the distributed shear

$$q_2 = \frac{B_y NI}{2\pi r}\cos\theta \tag{22}$$

which is antisymmetric with respect to the equatorial plane $\theta = \pm \pi/2$.

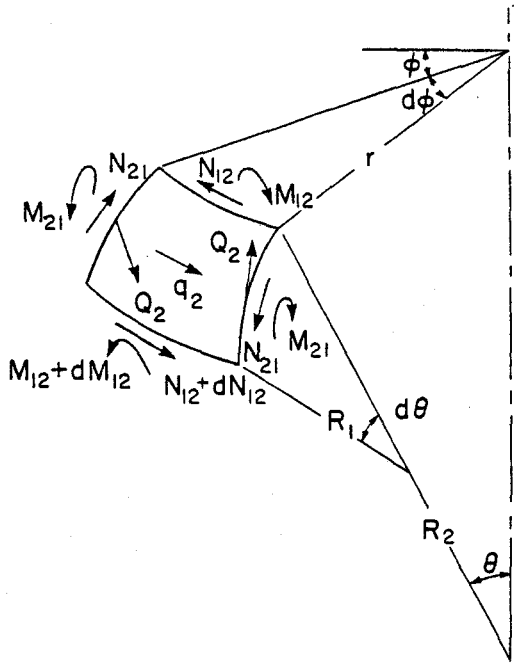

Fig. 2 Differential element of a shell of revolution under antisymmetric loading.

Equations of Equilibrium. In case of an antisymmetrical distributed shear load (22) only shear stress resultants and shear stress couples are generated in the shell as shown in Fig. 2. The equilibrium of the shell is described by the following four equations.

$$\frac{dN_{12}}{ds} + \frac{1}{r}\frac{dr}{ds}\left(N_{12} + N_{21}\right) + \frac{Q_2}{R_2} = -q_2 \tag{23}$$

$$\frac{dM_{12}}{ds} + \frac{1}{r}\frac{dr}{ds}\left(M_{12} + M_{21}\right) - Q_2 = 0 \tag{24}$$

$$N_{12} - N_{21} + \frac{M_{12}}{R_1} - \frac{M_{21}}{R_2} = 0 \tag{25}$$

$$M_{12} - M_{21} - \frac{h^2}{24}\left(\frac{1}{R_2} - \frac{1}{R_1}\right)\left(N_{12} + N_{21}\right) = 0 \tag{26}$$

Stress-Strain and Strain-Displacement Relations. The constitutive relationships (Hooke's law) if only shear strains and stresses are involved are expressed for an orthotropic material in the form

$$\gamma_{12} = \frac{1}{G_{12}}\tau_{12},\ \gamma_{23} = \frac{1}{G_{23}}\tau_{23} \tag{27}$$

Minimization of the shear strain energy expressed in terms of shear stress resultants N_{12}, N_{21}, Q_{23} and shear stress couples M_{12} and M_{21} yields three constitutive relationships

$$\epsilon_{12m} = \frac{1}{4G_{12}h}\left(N_{12} + N_{21}\right) \tag{28}$$

$$\gamma_{23m} = \frac{1.2}{G_{23}h}Q_2 \tag{29}$$

$$\kappa_{12} = \frac{3}{G_{12}h^3}\left(M_{12} + M_{21}\right) \tag{30}$$

Utilization of the four equilibrium equations (23) - (26) by means of the Lagrange multiplier method leads to expressions for the effective midsurface shear strain and curvature variations in terms of the effective midsurface linear displacement v and angular displacement β_2.

$$\epsilon_{12m} = \frac{1}{2}\left(\frac{dv}{ds} - \frac{1}{r}\frac{dr}{ds}v\right) + \frac{h^2}{24}\left(\frac{1}{R_1} - \frac{1}{R_2}\right)\Omega \tag{31}$$

$$\Omega = -\frac{1}{4}\left(\frac{1}{R_1} + \frac{1}{R_2}\right)\left(\frac{dv}{ds} + \frac{1}{4}\frac{dr}{ds}v\right) + \frac{1}{2}\left(\frac{d\beta_2}{ds} + \frac{1}{r}\frac{dr}{ds}\beta_2\right) \tag{32}$$

$$\kappa_{12} = \frac{1}{2}\left(\frac{d\beta_2}{ds} - \frac{1}{r}\frac{dr}{ds}\beta_2\right) + \frac{1}{4}\left(\frac{1}{R_2} - \frac{1}{R_1}\right)\left(\frac{dv}{ds} + \frac{1}{r}\frac{dr}{ds}v\right) \tag{33}$$

$$\gamma_{23m} = \beta_2 - \frac{v}{R_2} \tag{34}$$

NUMERICAL IMPLEMENTATION AND RESULTS

The solutions to the equations presented above, with appropriate boundary conditions give a complete description of the behavior of an orthotropic shell of revolution, of finite thickness.

In order to obtain the necessary quantities

$$\frac{1}{R_1},\ \frac{1}{R_2},\ \text{and}\ \frac{1}{r}\frac{dr}{ds},$$

which enter as coefficients into equations, the meridian of the shell should be described as a function of s or r, either analytically or in a tabulated form

The geometrical identities used to describe the shell of revolution are:

$$\frac{dr}{ds} = \cos\theta \tag{35}$$

$$\frac{1}{R_1} = \frac{d(\sin\theta)}{dr} \tag{36}$$

$$\frac{1}{R_2} = \frac{\sin\theta}{r} \tag{37}$$

A computer code for the finite difference solution of the two groups of equations corresponding to symmetrical and antisymmetrical loadings has been developed. In order to complete the analysis, the code requires the analytical or tabulated expression for the shape of the meridian in the form

$$\sin\theta = f(r) \tag{38}$$

along with the inner and outer toroidal radii, effective material physical properties, and the number of ampere-turns.

The meridian shapes presented here as examples are a circle and the "bending free" shell of Gray et al (10). Both shells have dimensions of the toroidal field coils in the Fusion Engineering Device (FED) described in (14), i.e., r_{in} = 2.14 m, r_{out} = 10.5 m, NI = 115 MAT, effective shell thickness h = 0.66 m and a coil case thickness 0.08 m. Figure 3 shows the meridians of the circular and "bending free" shells analyzed in this paper, along with that of a Princeton D.

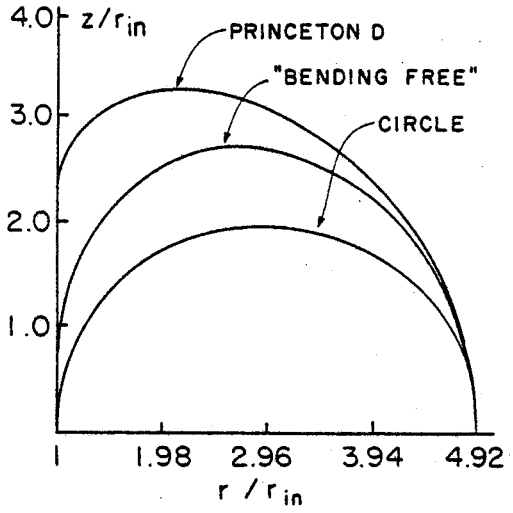

Fig. 3 Meridians of circular, "bending free", and Princeton D tori for FED aspect ratio.

The results of the analyses are presented in Fig. 4 and Fig. 5. Figure 4 shows the distribution of the effective meridional and circumferential membrane stresses in the coils and intercoil structures of both shapes. The effective meridional and circumferential bending stresses in the extreme fibers of the structural elements are as shown in Fig. 5. For the circular configuration the primary tensile stress at the inner leg at the equator is 151 MPa while the peak bending stress is 54 MPa. For the "bending free" configuration, the primary tensile stress in the inner leg at the equator is 139 MPa, while the peak bending stress is 66 MPa.

This demonstrates that if the finite thickness of the magnet structure is accounted for the "bending free" configuration proposed in (10) has bending stresses which are proportionally as large as the bending stresses in the circular configuration.

Since the total upward force on the upper half of the coil system must be

$$F_z = \frac{\mu_o (NI)^2}{4\pi} \ln \frac{r_{out}}{r_{in}} \qquad (39)$$

or 2122 MN, the theoretical minimum tension is 1061 MN in the inner leg, giving an average stress of 120 MPa in an ideal constant tension coil. Thus, the tensile stress in the inner leg at the equator for

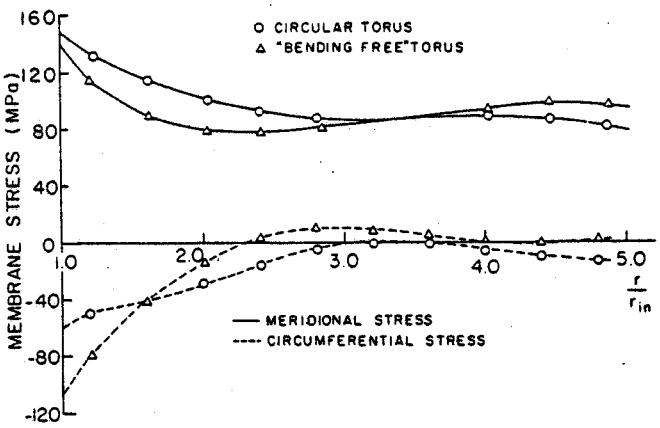

Fig. 4 Effective membrane stresses in circular and "bending free" coil structures with FED dimensions.

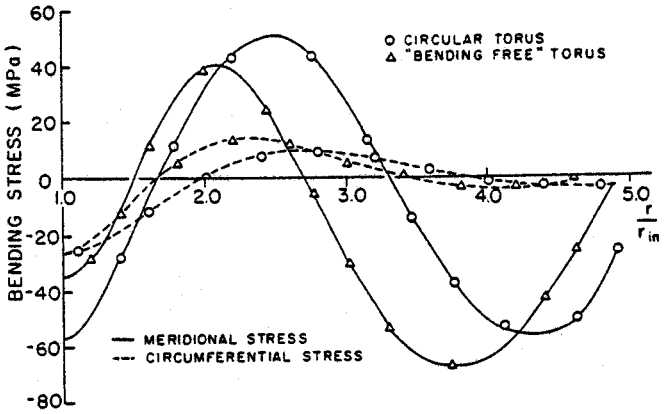

Fig. 5 Effective bending stresses in the extreme fibers of circular and "bending free" coil structures with FED dimensions.

circular coil is 1.26 times the theoretical minimum, while the tensile stress for the "bending free" configuration is 1.16 times the theoretical minimum. The primary stress in the "bending free" shape is 8.5% smaller than that in the circle, while the perimeter of the "bending free" configuration is 18% greater than that of a circle, implying that the circular configuration requires less mass for a given set of stress allowables.

CONCLUSIONS

An efficient method of analysis of toroidal magnet structures of arbitrary configuration, and subjected to electromechanical and thermal loads has been developed and numerically implemented.

It has been found that due to the finite thickness of realistic magnet structures and discontinuity of the displacement field present in the linear membrane theory the "bending free" shell configuration derived in (10) has bending stresses.

The whole concept of shape optimization based on minimization of bending stresses is called into

question. The design strategy of simply making the toroidal field coils circular or as small as possible, within the constraints of reactor assembly and maintenance can be recommended as an alternative. Reactor concepts with all external vertical field coils could be substantially reduced in weight and cost by using low profile coils.

ACKNOWLEDGMENTS

This work was supported by the Office of Fusion Energy, U.S. Department of Energy, under contract DOE/ET-51013-31. The Francis Bitter National Magnet Laboratory receives support from the National Science Foundation.

REFERENCES

1 Reissner, E., "On Some Problems in Shell Theory," Structural Mechanics, Proceedings of the First Symposium on Naval Structural Mechanics, Pergamon Press, New York, 1960, pp. 74-113.

2 File, J., Mills, R.G., and Sheffield, G.V., "Large Superconducting Magnet Designs for Fusion Reactors," IEEE Transactions of Nuclear Science, NS-18, 1971, pp. 277-282.

3 DeMichele, D.W., Darby, J.B., Jr., "Three-Dimensional Mechanical Stresses in Toroidal Magnets for Controlled Thermonuclear Reactors," Proceedings of the Fifth Symposium on Engineering Problems of Fusion Research, 1974, pp. 558-569.

4 Söll, M., "Comparison of Some Analytical and Numerical Calculated Parameters for Toroidal Field Coils," IPP 4/145, Nov. 1976, Max-Plank Institute for Plasma Physics, Munich, Federal Republic of Germany.

5 Diserans, N.J., "Stress Analysis Studies in Optimized 'D' Shaped Tokamak Magnet Designs," RL-75-117, July 1975, Rutherford Laboratory, Chilton, Didcot, Oxon, England.

6 Gralnick, S.L., and Tenney, F.H., "Analytic Solutions for Constant Tension Coil Shapes," Journal of Applied Physics, Vol. 47, No. 6, June 1976, pp. 2710-2715.

7 Weissenburger, D.W., Christensen, U.R., Bialek, J., "Pure Tension Shape of a Thick Torus," PPPL-1353, July 1977, Princeton Plasma Physics Laboratory, Princeton, N.J.

8 Moses, R.W., and Young, W.C., "Analytical Expressions for Magnetic Forces on Sectored Toroidal Coils," Proceedings of the Sixth Symposium on Engineering Problems of Fusion Research, 1976, pp. 917-921.

9 Gralnick, S.L., Ojalvo, I.U., Zatz, I.J., and Balderes, T., Nuclear Technology, Vol. 45, No. 10, October 1979, pp. 233-243.

10 Gray, W.H., Stoddart, W.C.T., Akin, J.E., "A Derivation of a Bending Free Todoidal Shell for Tokamak Fusion Reactors,"Journal of Applied Mechanics, Vol. 46, March 1979, pp. 120-124.

11 Welch, C.T., "Bending-Free Shapes for Toroidal Magnet Field Coils with Concentrated Symmetric Reactions," Proceedings of the Sixth Symposium on Engineering Problems of Fusion Research, 1976, pp. 410-913.

12 Ojalvo, I.U., and Zatz, I.J., "Structural Support Design Method for Minimizing In-Plane TF Coil Stresses," Proceedings of the Eighth Symposium on Engineering Problems of Fusion Research, 1980, pp. 1463-1468.

13 Flügge, W., Stresses in Shells, 2nd Ed., Springer-Verlag, Berlin, 1973.

14 Flanagan, C.A., Steiner, D., Smith, G.E., Fusion Engineering Design Center Staff, "Fusion Engineering Design Description," Vol. 1, ORNL/TM-7948/V1, December 1981, Oak Ridge National Laboratory, Oak Ridge, Tennessee.

15 Lekhnitski, S.G., Theory of Elasticity of Anisotropic Elastic Body, Holden-Day, San Francisco, California, 1963.

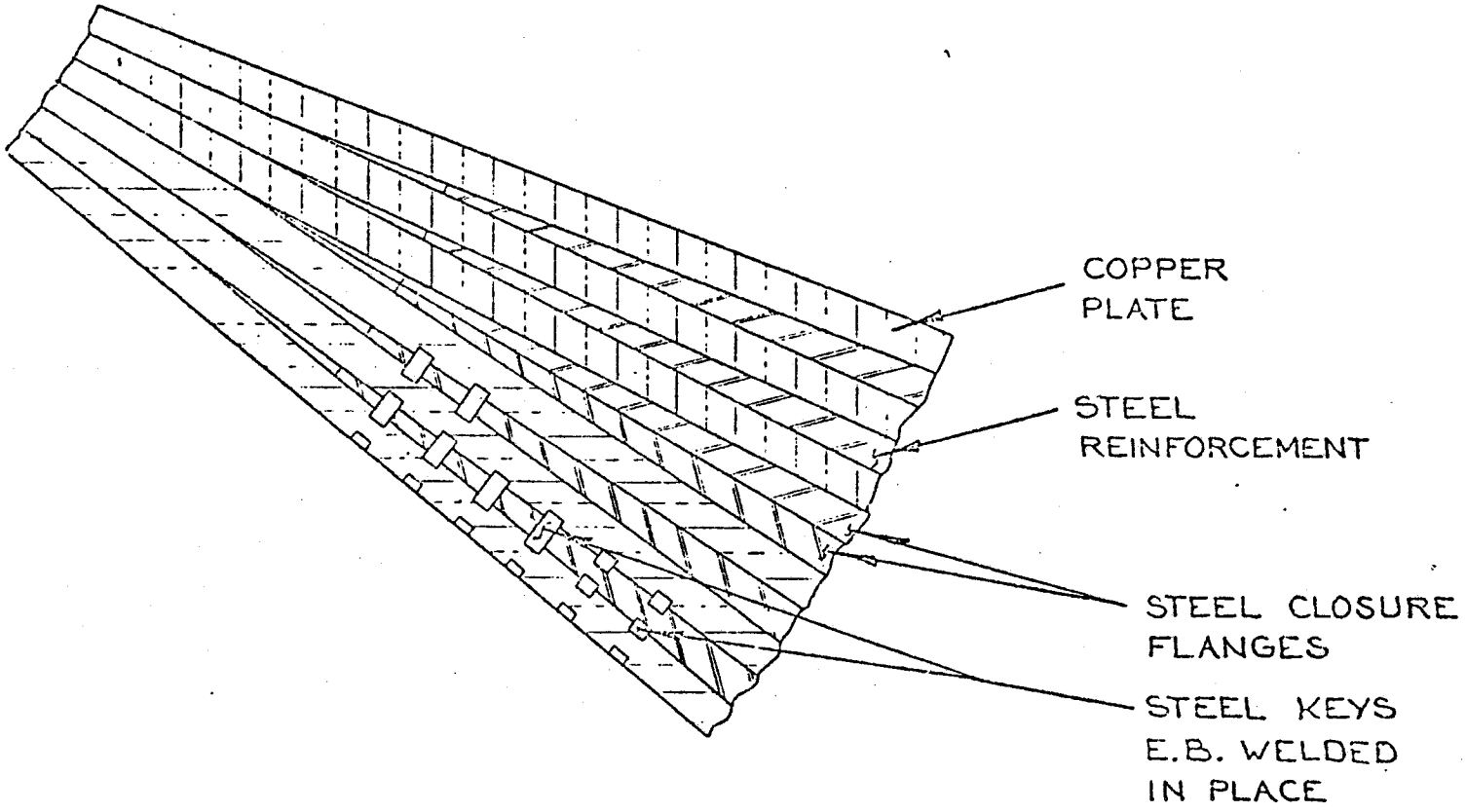

FIGURE 5.1 COPPER-INSULATION-STAINLESS STEEL ASSEMBLY WITH KEYS.

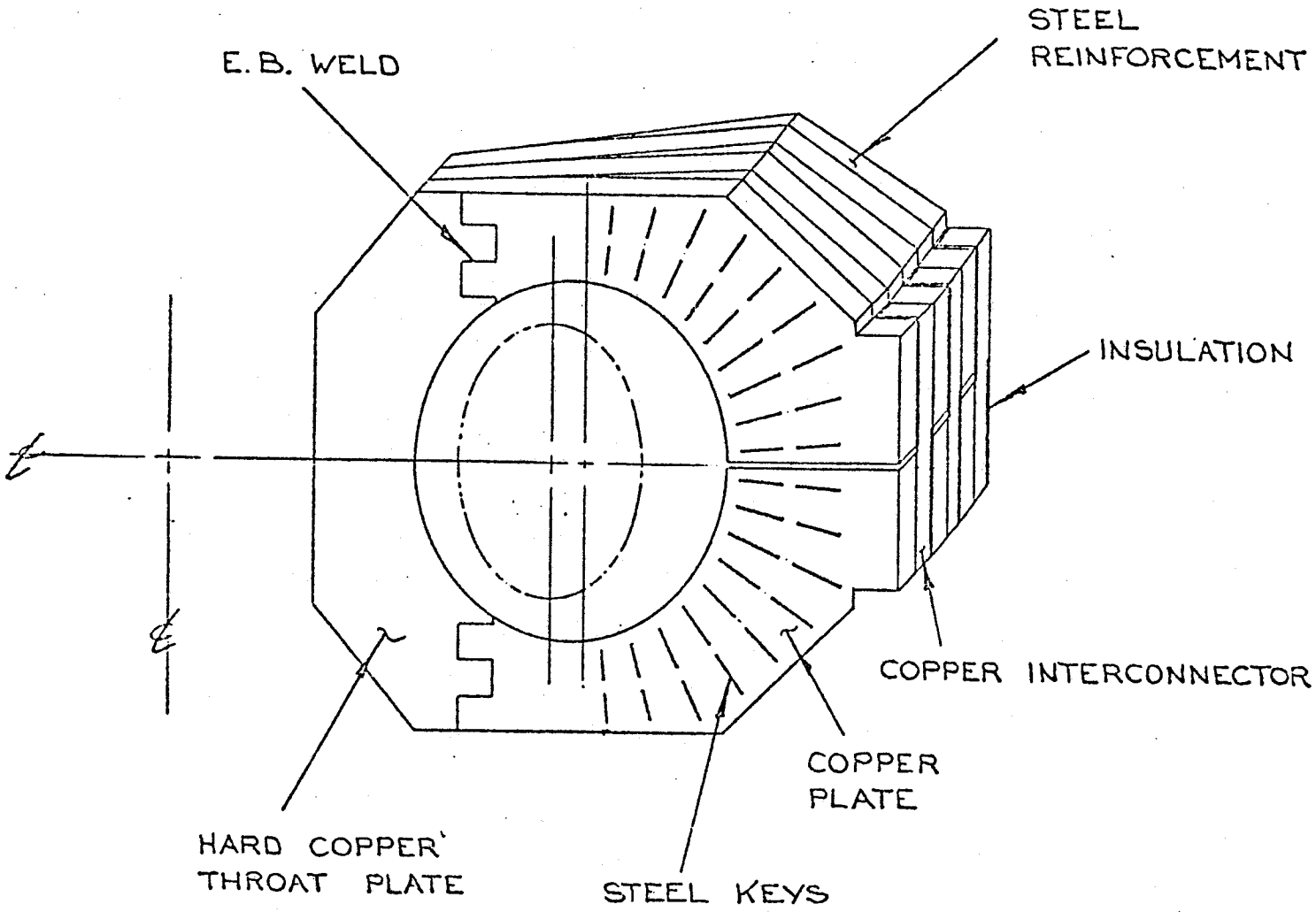

FIGURE 5.2 GENERAL VIEW OF THE KEY ARRANGEMENT.

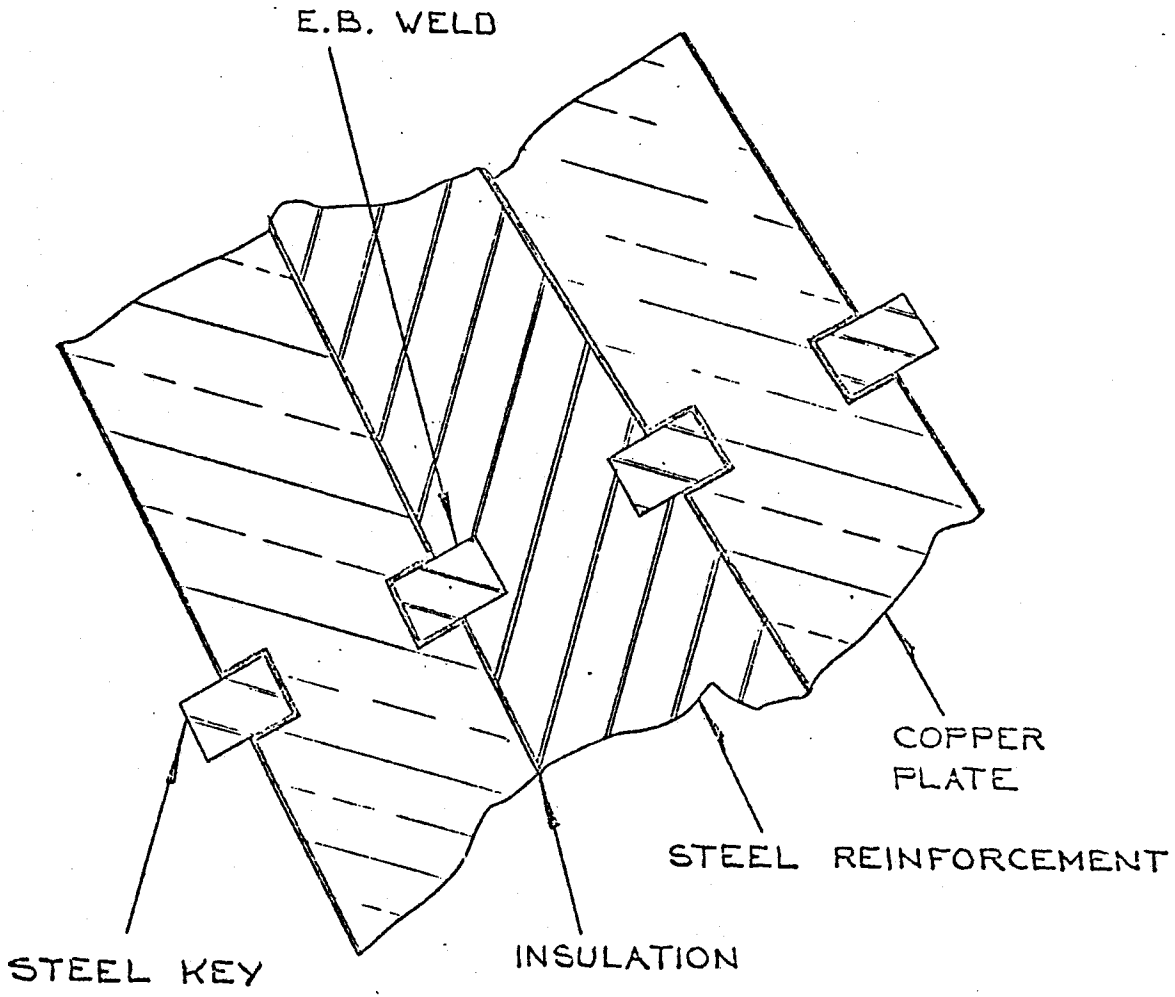

FIGURE 5.3 SCHEMATIC OF THE KEY POSITIONING ON THE PLATE SURFACE.

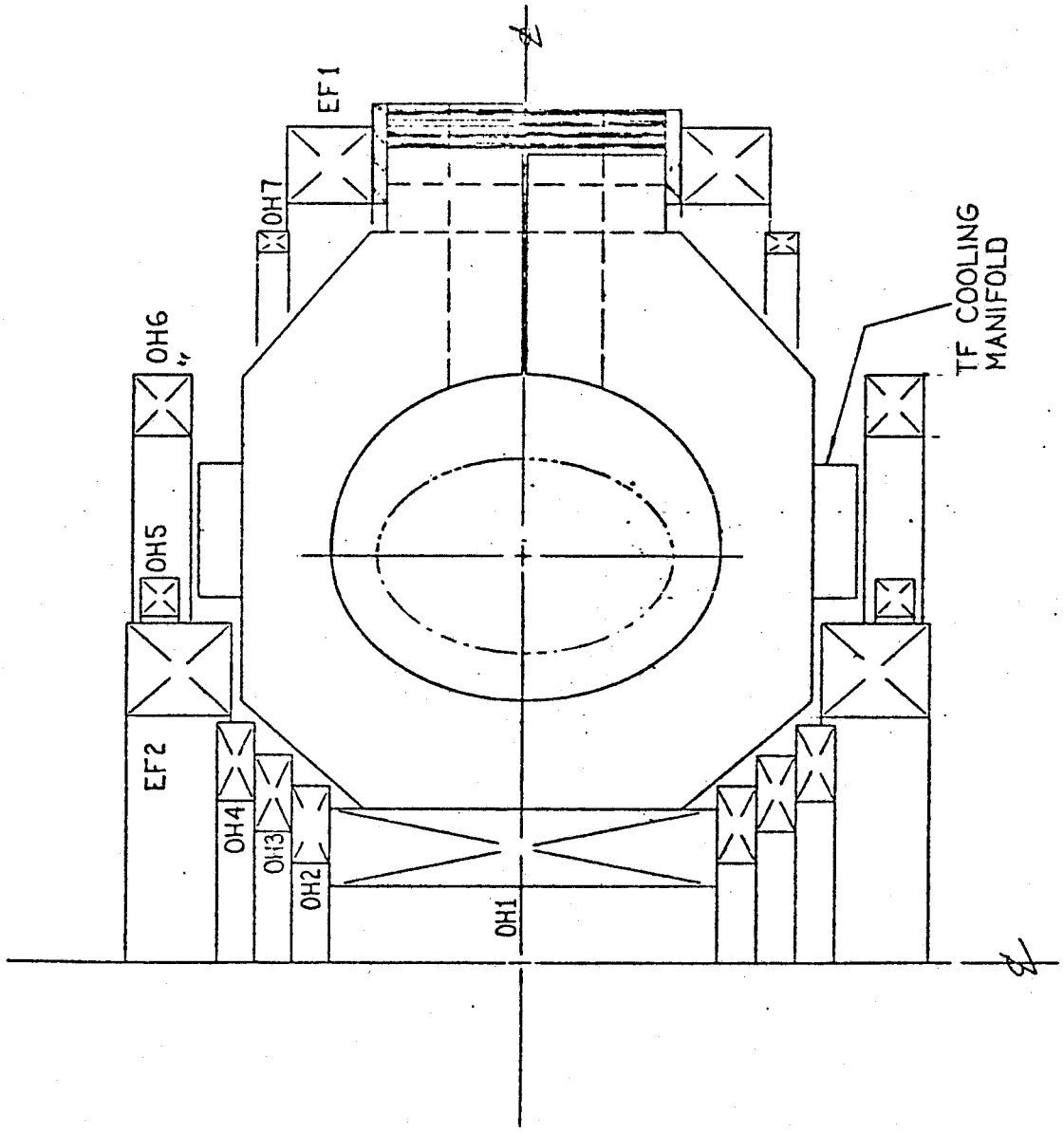

FIGURE 5.4 ELEVATION VIEW OF THE MAGNET SYSTEM.

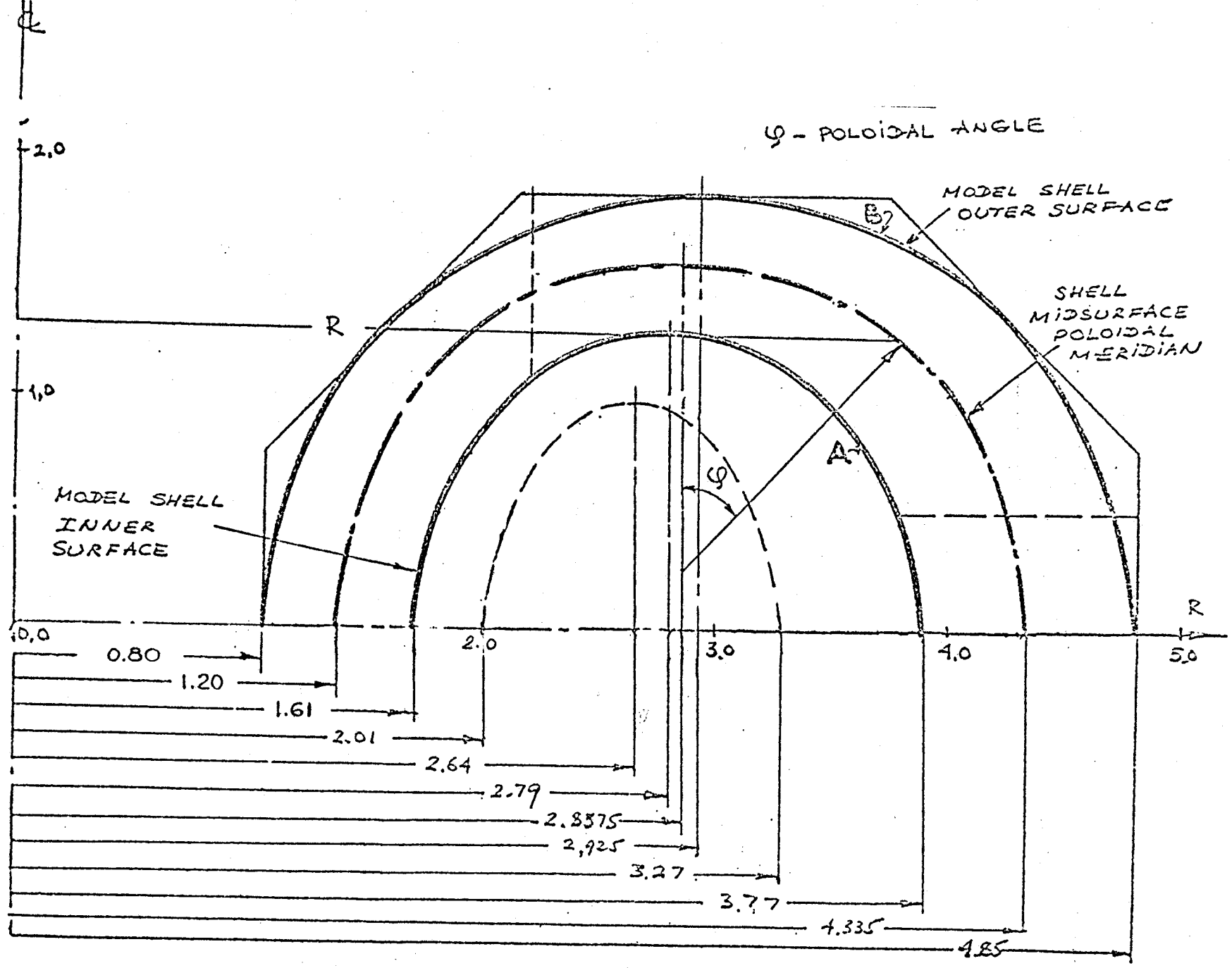

Figure 5.5 Toroidal Shell Structural Model

FIGURE 5.6

FEDR TOKAMAK. MEMBRANE AND BENDING STRESSES IN COPPER. BO=7.1 T, RP=2.64 M, H=3.67 M.

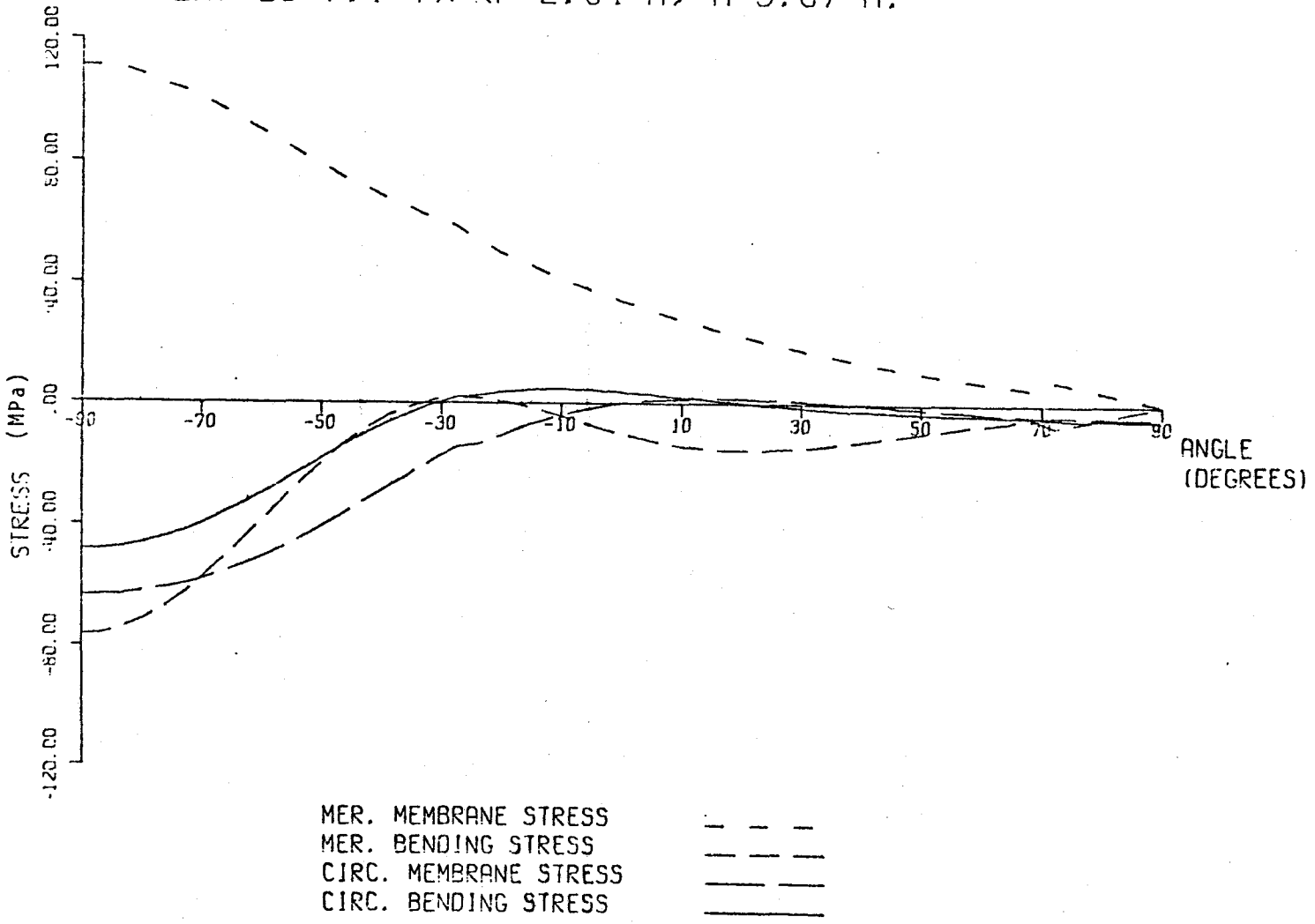

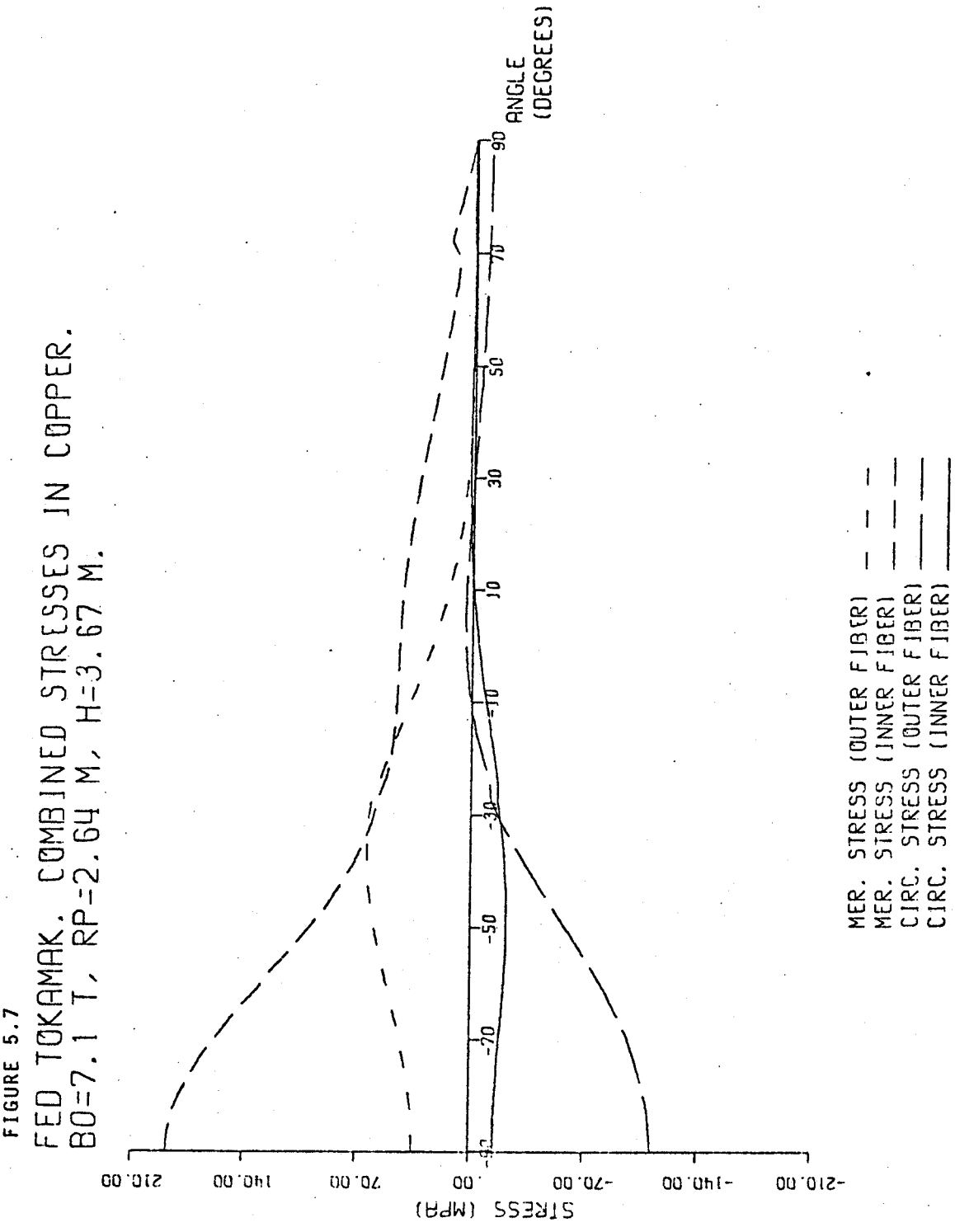
FIGURE 5.7
FED TOKAMAK. COMBINED STRESSES IN COPPER.
BO=7.1 T, RP=2.64 M, H=3.67 M.
ANGLE (DEGREES)
90
70
50
30
10
-10
-30
-50
-70
-90
STRESS (MPA)
210.00
140.00
70.00
.00
-70.00
-140.00
-210.00
MER. STRESS (OUTER FIBER)
MER. STRESS (INNER FIBER)
CIRC. STRESS (OUTER FIBER)
CIRC. STRESS (INNER FIBER)

FIGURE 5.8

FEDR TOKAMAK. VON MISES STRESSES IN COPPER.
BO=7.1 T, RP=2.64 M, H=3.67 M.

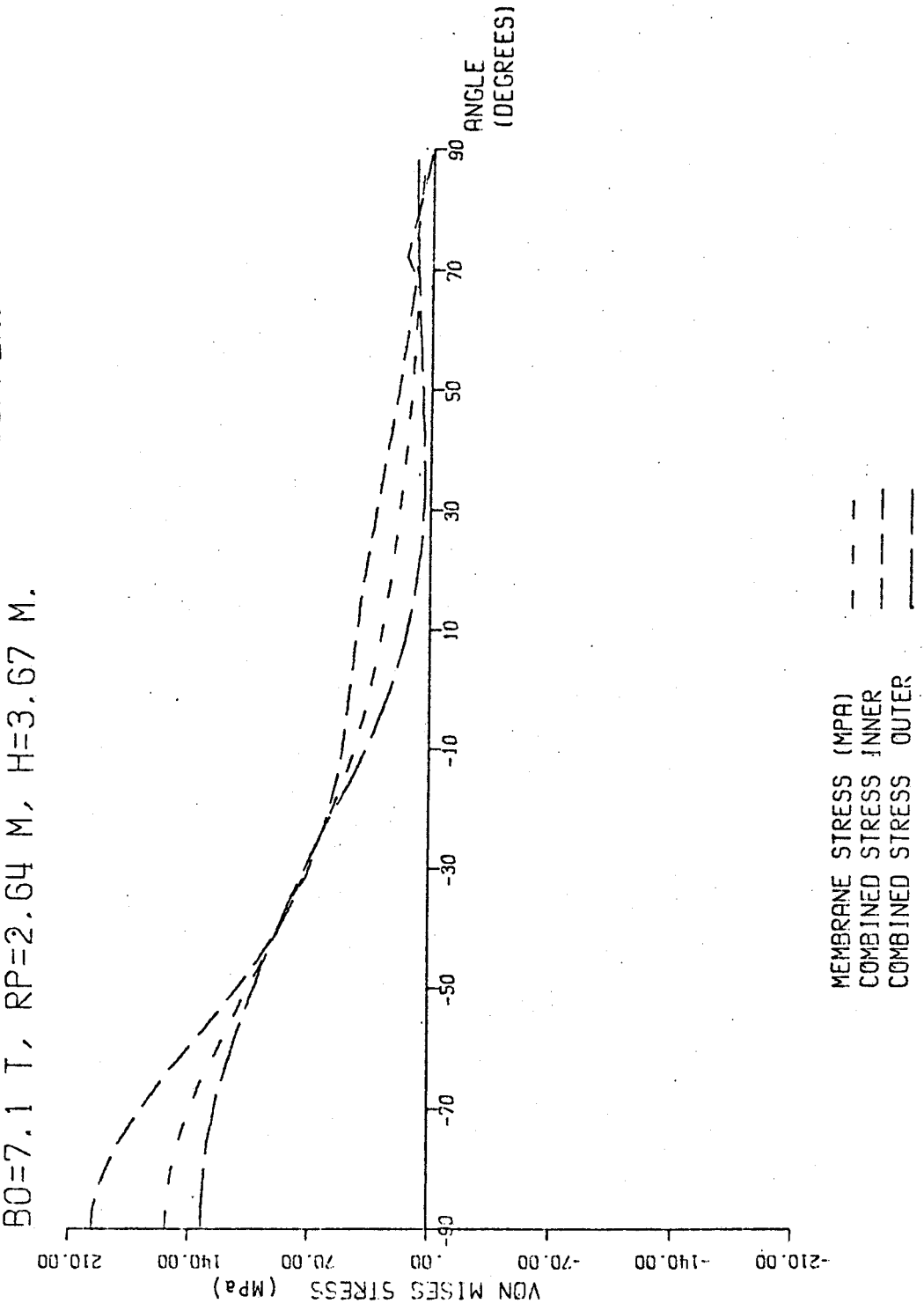

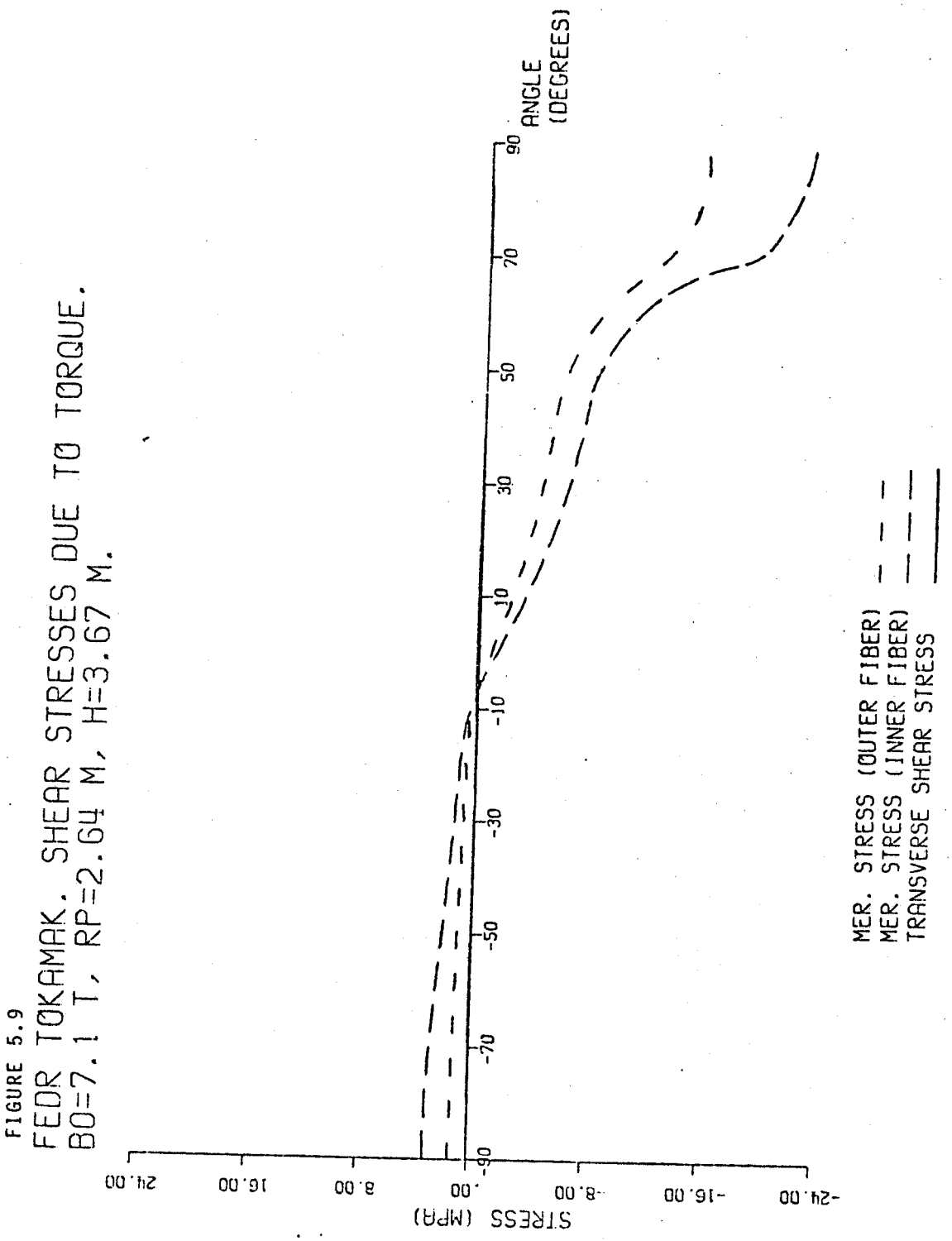
FIGURE 5.9
FEDR TOKAMAK. SHEAR STRESSES DUE TO TORQUE.
BO=7.1 T, RP=2.64 M, H=3.67 M.
ANGLE (DEGREES)
90
70
50
30
10
-10
-30
-50
-70
-90
STRESS (MPA)
24.00
16.00
8.00
.00
-8.00
-16.00
-24.00
MER. STRESS (OUTER FIBER)
MER. STRESS (INNER FIBER)
TRANSVERSE SHEAR STRESS

FIGURE 5.10 FEDR TOKAMAK. LOAD TO BE TRANSMITTED FROM COPPER TO STEEL.

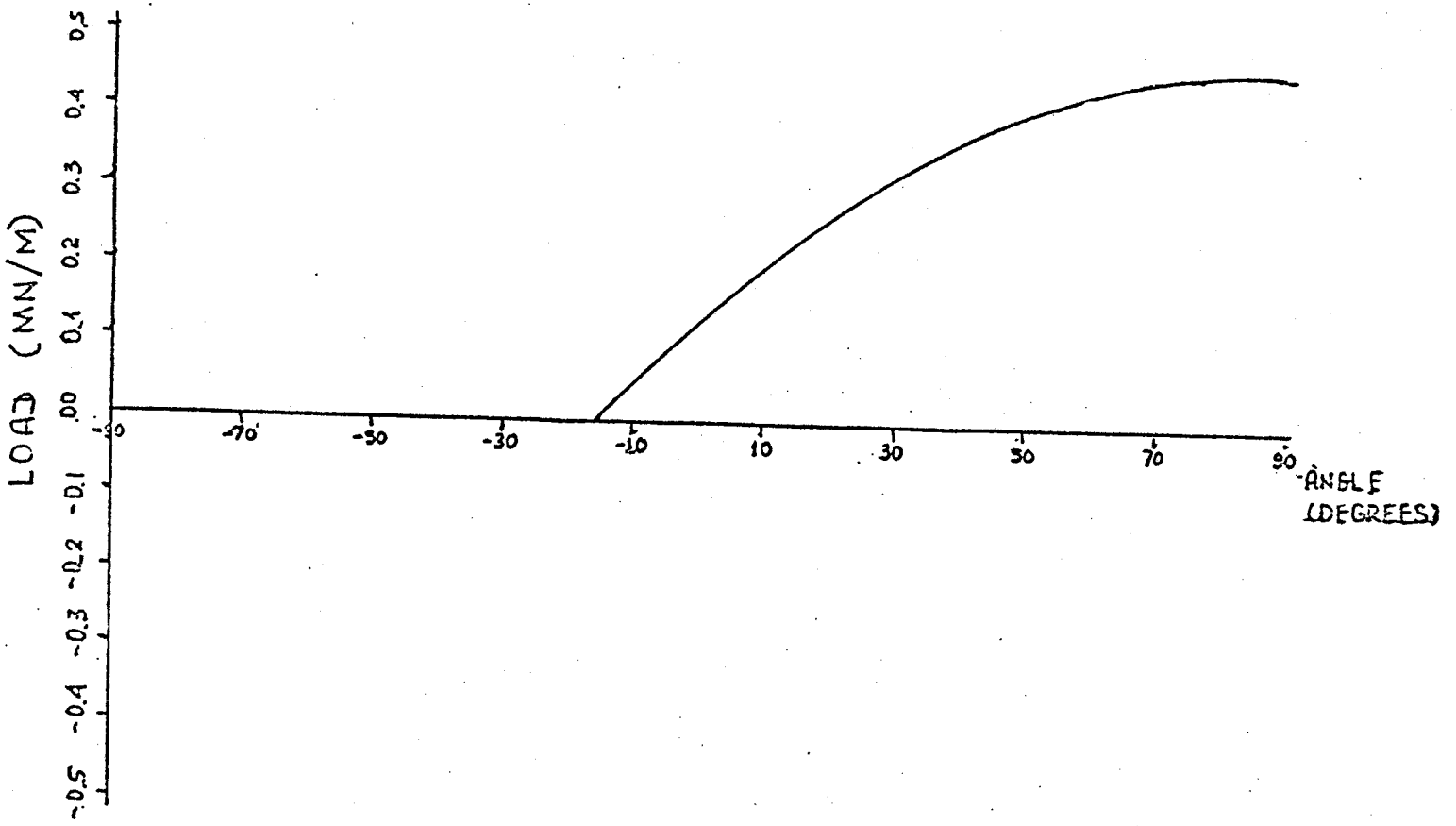

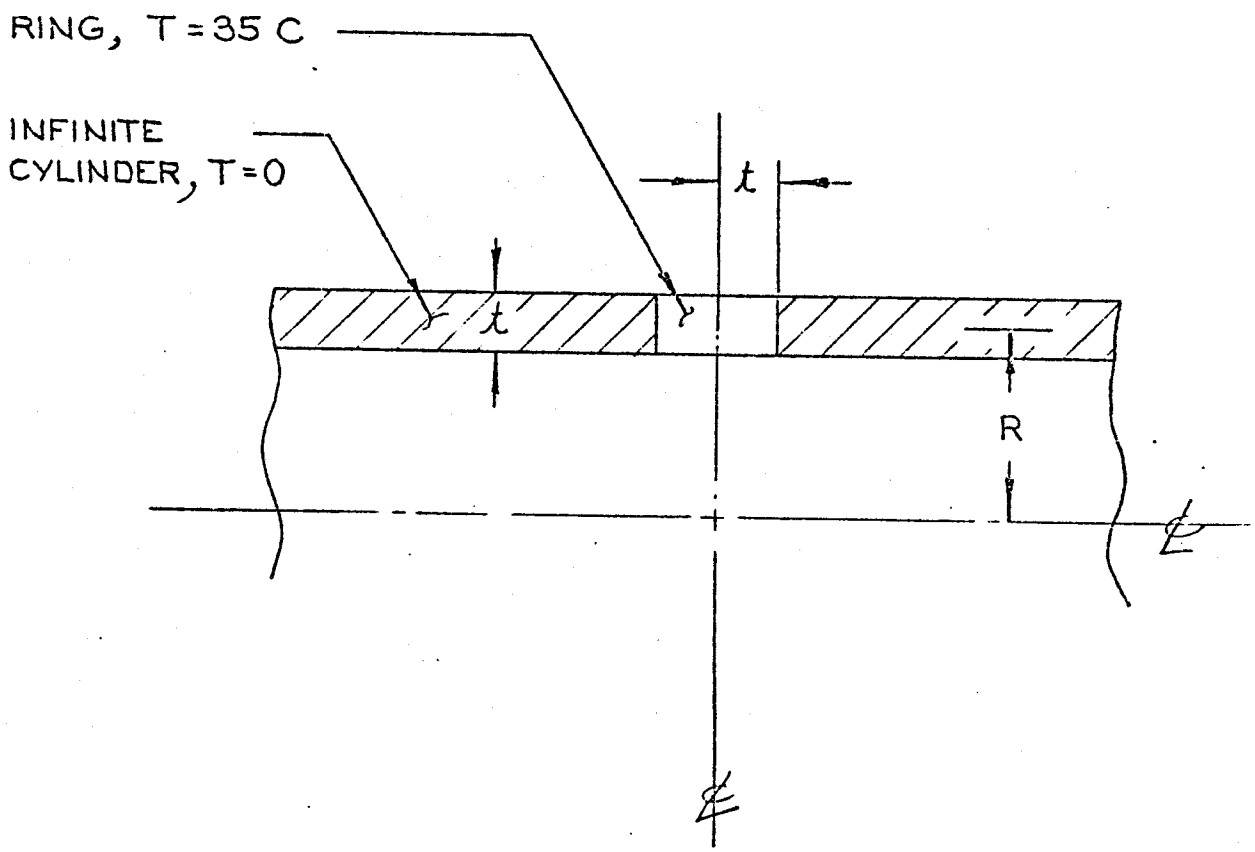

Figure 5.11 Thermal Stress Model

6. INSULATOR MATERIALS INVESTIGATIONS

6.1 Introduction

MIT has conducted an investigation into the survivability of organic insulators in connection with the design of the ITR magnet for which the anticipated fluence was 10^{11} rads equivalent. The method used to measure the properties of the insulator is shown in Figure 6.1. The results of the fatigue tests are shown in Figure 6.2. Work is continuing in that area on a new DOE contract for which higher dose levels will be applied to s-glass insulators with a matrix material considered to be the best for the ITR program (probably polyimide).

This section discusses the ITR project briefly and identifies the current candidate insulators. It also contains a brief critical review of the current status of insulation survivability and a description of the MIT program.

6.2 Insulator Testing Program

6.2.1 Introduction

This section is, for the most part, a reproduction of the paper presented at the ICEC Conference in Geneva on August 2, 1980 (Reference 1 .)

The term "radiation damage" as applied to structural behavior can be defined as the reduction in load-carrying ability resulting from exposure to radiation.. It has been observed that the radiation induced loss of strength of a material could depend upon the type of load to be resisted. Data in this paper indicate that the structural configuration could be of major importance.

The reactor magnet consists of large flat plates of copper and of steel separated by thin insulator sheets. The insulator must survive 10,000 cycles of 140 MPa pulsed pressure together with 8.4 MPa pulsed interlaminar shear stress and a lifetime radiation fluence of $10^{20} n/cm^2$. (equivalent to 10^{11} rads).

Most of the existing test data on insulator radiation survivability have been obtained from static flexural and compression tests on rods. It may be apparent that those results would not apply to thin sheets under cyclic compressive load. Preliminary studies on unirradiated insulators indicated that a 1/2-millimeter-thick fiberglass composite with an organic matrix might withstand the ITR environment. Consequently, a program of irradiation and test was carried out to explore that possibility.

6.3 Rationale

The failure mode in a compressed thin sheet of brittle material is different from that of a rod. The stress distribution in a rod is uniaxial and failure usually occurs on the familiar diagonal shear plane, more or less at 45 degrees to the rod axis. The thin sheet also would be under uniaxial compression if a pure pressure were to be applied. However, the insulators of FED-R2 and ITR are compressed between large flat plates. As a result, there is friction-induced restraint in the plane of the sheet similar to the behavior studied by Bridgman. The diagonal shear failure planes cannot form easily. Observations reveal that the insulator specimens are reduced to powder by extensive compressive cycling, in support of that hypothesis.

Failure of G-10 and similar grp materials may begin by crushing at the intersections of the cloth warp and fill fibers. Tendency for the cloth to spread would be resisted by friction from the metal plates retarding breakage until the fibers begin to crush between intersections. The matrix material would help to support the

fibers during the process. The onset of failure has been observed to be accompanied by rapid degradation of stiffness.

Development of a quantitative theoretical explanation would require more extensive study. Until that time, the above rationale has been adopted as part of the basis for believing that materials like grp can withstand the FED fluence at the design compression stress for the required number of cycles.

6.4 Failure Criterion

It is a simple matter to observe failure in compressed brittle rods. A break occurs and the testing machine load drops suddenly to zero. In thin sheets, however, the failure is not so obvious. This is particularly true of fatigue loading.

It was noticed, during exploratory tests on unirradiated specimens, that the stiffness appeared to increase by a few percent up to approximately 5,000 to 10,000 cycles after which the stiffness reduced by several percent during each successive interval of 10,000 cycles. The same phenomenon was observed during the INEL tests on irradiated specimens except that the degradation in stiffness occurred in a few hundred cycles. Subsequent examination showed that at least one disk in a stack of five had been reduced to powder.

It was decided to define failure in thin sheets as the rapid reduction of stiffness. The relevant data were chosen as the stress level and the number of cycles at which that rapid reduction occurred.

6.5 Initial Tests

Experiments were carried out with sheets of fiber-reinforced plastics and one common inorganic electrical insulator. Unirradiated specimens of G-7, G-10 and micaglass were subjected to compression fatigue at RT. Both G-7 and G-10 are commercial E-glass reinforced plastics. The matrix system of G-7 is silicone while that of G-10 is epoxy. The test fixture and loading scheme are shown in Fig. 6.1.

The initial test results appear in Table 6.1. The grp survived pressures twice as high as in ITR for the required 10,000 cycles. The micaglass, however, did not survive under pressures 50 percent greater than in FED-R2. The 1 Hz frequency was chosen as a practical compromise between the low FED-R2 cycle and the need for shorter test times to collect data from several samples.

Additional tests (Table 6.5) were performed on unirradiated specimens selected from the composite formulations described below. Those results also indicated high potential for survival.

6.2.5 INEL Tests on Irradiated Specimens

Disks were cut from thin sheets of G-7, G-10 and G-1 CR. They were irradiated in the Advanced Test Reactor at Idaho National Engineering Laboratory. The nuclear flux was calculated from a standard code used at INEL and is stated to be within 20 percent of actual values. The total fluence was $1.6 \times 10^{19} n/\text{cm}^2$ for neutron energies greater than 0.1 Mev, $10^{20} n/\text{cm}^2$ for the total neutron spectrum and 3.8×10^{11} rads of gamma radiation. That dose is somewhat higher than the fluence expected in FED-R2.

The specimen temperature was reported to be 320 K. All specimens were found to be highly radioactive after months of cooldown. Consequently, testing was conducted in a hot cell.

The compression fatigue tests were conducted in the same manner as for the unirradiated samples (Figure 4.2). The results appear in Table 6.2. In addition the G-10 data are plotted on the graph of Figure 6.2. All tests were stopped arbitrarily at 200,000 cycles if no failure had been observed.

It is clear that the observed strengths are much greater than reported previously for rods irradiated at 4.9 K for which G-10 CR static compression values of about 69 MPa were obtained. The INEL results also exceed the FED requirements. The stress level of 345 MPa is more than twice the FED requirement. Furthermore, 200,000 cycles corresponds to 20 times the required life.

6.7 MIT Tests

The INEL tests were considered to support the rationale that G-10 might survive the ITR environment. It was important to obtain independent data as a further check. It also was decided to broaden the scope of the program by including other potential candidate insulators.

A search of the literature showed that epoxy and polyimide resins with fiberglass reinforcement could be considered as candidate insulators for ITR. Among epoxy resins, glycidyl amines were concluded to be more radiation resistant. S-glass appears to provide a more useful reinforcement than E-glass for radiation resistant insulators. The MIT test results are shown in Table 6.3 and Figure 6.2.

6.8 Conclusions

Evidence has been obtained at RT to support the rationale that thin sheet grp can withstand the ITR and FED-R2 radiation and compression loading environment. It remains to conduct combined interlaminar shear and compression tests during irradiation at 77 K before the survivability of organic insulators can be established reliably for use in high fluence environments at other temperatures.

6.9 Critical Review of Status of Insulator Survivability

The following is a brief critical review of the state of knowledge on organic insulator survivability in a radiation environment. It is the basis for the planned MIT program.

No theory exists for relating structural survivability to radiation dosage. Existing insulator test data generally do not represent conditions to be expected in fusion reactors (Table 1.). (Much early data were developed for particle accelerators.)

Loads have not been applied in-situ. Test temperatures (and, for the most part, irradiation temperatures) have not been at 4 K, with few exceptions. Few shear tests have been performed and no combined load data were found.

Test reports were vague or incomplete with regard to irradiation spectra and dose levels. Rads and n/cm^2 were intermixed. The effect of gamma/neutron ratios has not been studied. Most reports contain little discussion of failure criteria or failure modes.

Contradictory claims exist. Some claims are unsupported by data. As an example, boron-free glass was claimed to be effective but test data show damage under moderate irradiation levels.

The range of survivability behavior is large. Some materials degrade over several decades of dose level, some fall off in one decade and some decay within a certain dose range and regain strength at higher levels.

Properties vary with matrix material and reinforcement, sometimes by orders of magnitude. Activation levels also vary widely following dosage.

Data (References 1 and 2, for example) indicate that polyimide and S-glass provide the best composite tested to date. This conclusion is based on the fact that Coltman et al tested rods in compression, yet both results agree qualitatively. Furthermore, there is an indication of good survivability for that type of composite.

6.10 Appendix

MIT Materials Irradiation Test Programs

The MIT program is designed to close the gap between the fusion reactor and materials testing environments in order to obtain a more accurate assessment of organic insulator survivability.

6.10.1 FY'82 Program

The test specimens matrix materials will be TGPAP + OCA epoxy and Kerimid 601 polyimide. The reinforcements will be S and S2 glasses. At least 50 specimens of each combination would be irradiated at 4 K in the IPNS at Argonne. Selected combinations will be irradiated at 77 K in either the ETR at INEL or in TRIGA at Penn State, depending upon availability of the facilities.

Following irradiation, each group of specimens will be removed from the source, mounted in a testing machine, cooled to 77 K and subjected to cyclic loading at several peak stress levels to permit acquisition of a fatigue curve. Measurements of dielectric strength and electrical conductivity would be made after selected cycle numbers.

In parallel with the above activity, design details will be developed for an inpile test cell capable of operating at 77 K. The details will include the piping and refrigeration systems required for controlled operation at 77 K.

The final phase of the project will include consideration of shipment of selected specimens to the RTNS at Livermore for 14 MEV RT irradiation and subsequent testing at 77 K. If time and funding permit, this phase will be implemented. Otherwise, it will be deferred to FY'83.

6.10.2 FY'83 Program

The program would construct the inpile loading device to be designed in FY'82, followed by inpile testing at 77 K of four insulator compositions consisting of organic matrices and fiberglass reinforcements. The results will be compared with data from 77 K out-of-pile testing of insulators irradiated at RT and 77 K. The belief has been expressed (but not established by testing) that inpile loading could be more damaging to organic insulators than out-of-pile loading after irradiation.

The loading device and associated cooling equipment will be constructed to fit into either TRIGA at Penn State or into the ETR at INEL. The choice will be made in FY'82. At least one set of samples will be loaded inpile at 77 K in the test fixture which applies force to the flat faces of several insulator samples in series and which will include a means of conducting electrical tests. A set will consist of one of each combination of an epoxy or polyimide matrix reinforced by S or S2 fiberglass.

Results of the tests will be compared to existing data and to the FY'82 tests to be conducted on control samples irradiated at 77 K and 4 K but tested out-of-pile.

The experience gained in fabricating and operating the 77 K inpile loader will be used to design a facility for 4 K inpile loading.

6.10.3 FY'84 Program

During FY'84 the 4 K inpile tester will be constructed and tests will be conducted to meet the basic goal of the 3-year project, which is to simulate the FED environment (as closely as possible) which candidate insulators must survive. The data from the program will be compared to evaluate insulator mechanical and electrical survivability in an fusion reactor.

TABLE 6.1

Results of Compression Fatigue Tests of

Unirradiated Samples at RT

(5 Specimens of Each Type Tested in Stack Shown in Figure 6.1)

INITIAL TESTS

Material	Thickness (mm)	Max. Applied Stress (MPa)	Number of Cycles
		207	10,000 S
G-7	0.3	276	10,000 S
		207	100,000 F
G-10	0.50	310	60,000 S
Mica-Glass	0.50	207	10,000 F

S = Survived, F = Failed

TABLE 6.2

Results of INEL Compression

Fatigue Tests on Irradiated Insulators

Total Flutence = 3.8×10^{11} Rads, Equivalent

For all Specimens D = 11.1 mm

Material	Thickness (mm)	Temperature	Max. Appliedk Stress (MPa)	Number of Cycles
G-7	0.30	RT	207	10,000 F*
G-11	4.00	RT	207	10,000 F
			207	200,000 S
			241	200,000 S
		RT	276	21,900 F
			310	3,570
G-10	0.50		345	460 F
			207	20,000 S
		77 K	241	40,000 S
			276	36,000 S
			310	30,000 S
			345	30,000 S

*Paired disks broke, singles survived.

TABLE 6.3

Additional Compression Test Results

Total Fluence = 3.2×10^{10} Rads, Equivalent

Material Matrix System	Reinf.	Thickness (mm)	Max. Applied Stress (MPa)	Number of Cycles
Kerimid 601	S	0.50	310	60,000
TGPAP + DCA	S2	0.50	310	60,000
DGEBA + DDS	S2	0.50	310	60,000
TGPAP + DDM	E	0.46	310	60,000
TGPAP + DDM	S2	0.48	310	60,000
TGPAP + DDS	S2	0.50	310	60,000

Tests were halted arbitrarily at indicated number of cycles. All specimens survived.

TABLE 6.4

Comparison of Insulator Performance and Test Environment

FUSION REACTOR INSULATOR ENVIRONMENT

ALL CONDITIONS ACT TOGETHER

1. Nuclear radiation flux.
2. Lorentz (and preload) normal pressures, interlaminar shears and inplane bending plus membrane loads.
3. 10^3 to 10^6 cycles. Static load duration - months.
4. Liquid helium temperature (constant) for some. Pulse, starting at LN_2 temperature, for others.
5. Low gamma/neutron ratios.
6. 14 MeV spike at high fluence.

INSULATOR TEST CONDITIONS

ALL TESTING DONE AFTER APPLICATION OF TOTAL FLUENCE

1. Mostly RT irradiation, some cryogenic.
2. Mostly static, some cyclic, little creep testing, no combined load tests.
3. Most testing at RT, some at 77 K, some at 4 K.
4. High gamma/neutron ratios.
5. 14 MeV spike applied separately from other irradiation, at low fluence.

REFERENCES AND BIBLIOGRAPHY

1 E.A. Erez and H. Becker, "Radiation Damage in Thin Sheet Fiberglass Insulators", ICMC, Geneva, August 1980.

2 R.R. Coltman, Jr., "Organic Insulators and the Copper Stabilizer for Fusion Reactor Magnets", Int'l Conf. on Neutron Irradiation Effects, ANL, November 9-12, 1981.

3 Anon, **"Handbook on Materials for Superconducting Machinery"**, 1979.

4 S. Timoshenko, **"Theory of Elasticity"**, McGraw-Hill, 1934.

5 C.R. Brinkman, R.E. Korth and J.M. Beeston, "Influence of Irradiation on the Creep/Fatigue Behavior of Several Austentric Stainless Steels and Incoloy 800 at 700 C," ASTM STP 529, 1973.

6 G.E. Korth and R.E. Schmunk, "Low-Cycle Fatigue of Three Irradiated and Unirradiated Alloys," 9th Int. Symposium on Effects of Irradiation on Structural Materials.

7 Anon, **"Radiation Effect Design Handbook,"** Section 3. Electrical Insulation Materials and Capacitors. NASA CR 1787, July 1971.

8 E. Laurant, "Radiation Damage Test on Epoxies for Coil Insulation," NAL, EN-110, July 1969.

9 D. Evans, J.T. Morgan, R. Sheldon, G.B. Stapleton, "Post-Irradiation Mechanical Properties of Epoxy Resin/Glass Composites," RHEL/R200, Chilton, Bershire, England, 1970.

10 M.M. Von de Voorde, "Selection Guide to Organic Materials for Nuclear Engineering," CERN 72-7, May 1972.

11 G.R. Imel, P.V. Kelsey and E.H. Ottewitte, "The Effect of Radiation on TFTR Coil Materials," 1st Conference on Fusion Reactor Materials, January 1979.

12 R.R. Coltman, Jr., C.A. Klabunde, R.M. Kernohan and C.J. Long, "Radiation Effects on Organic Insulators for Superconducting Magnets," ORNL/TM-7077, November 1979.

13 H. Brechna, "Effect of Nuclear Radiation on Organic Materials; Specifically Magnet Insulations in High-Energy Accelerators," SLAC Report No. 40, 1965.

14 K. Shirasishi, Ed. "Report of Group Materials," IAEA Workshop on INTOR, June 1979.

15 P.W. Bridgman, "The Physics of High Pressure," G. Bell, London, 1931.

16 R.D. Hay and E.J. Rapperport, "A Review of Electrical Insulation in Superconducting Magnets for Fusion Reactors," MEA Report, 21 April 1976.

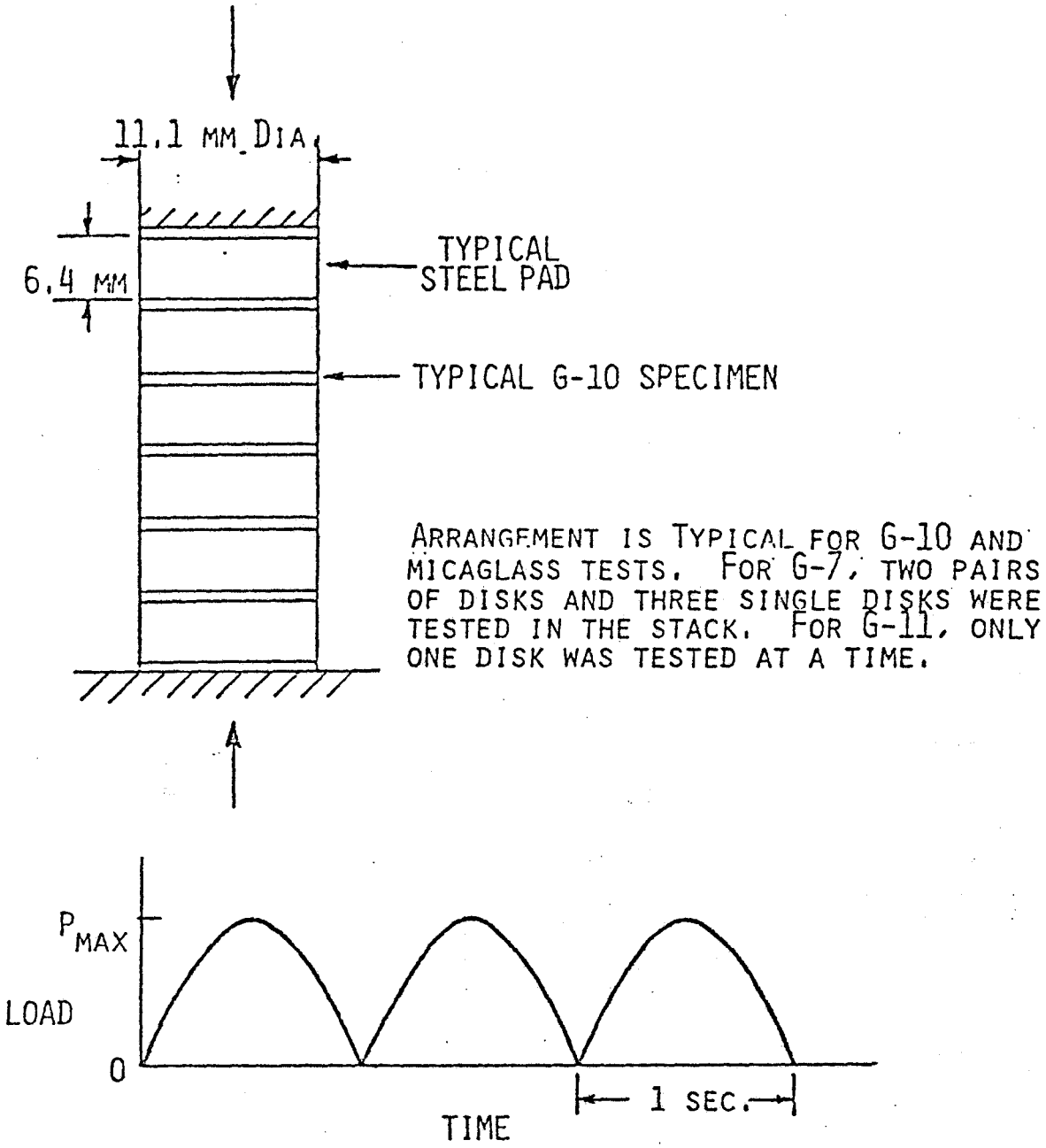

FIGURE 6.1 TEST FIXTURE SCHEMATIC AND LOADING CYCLE

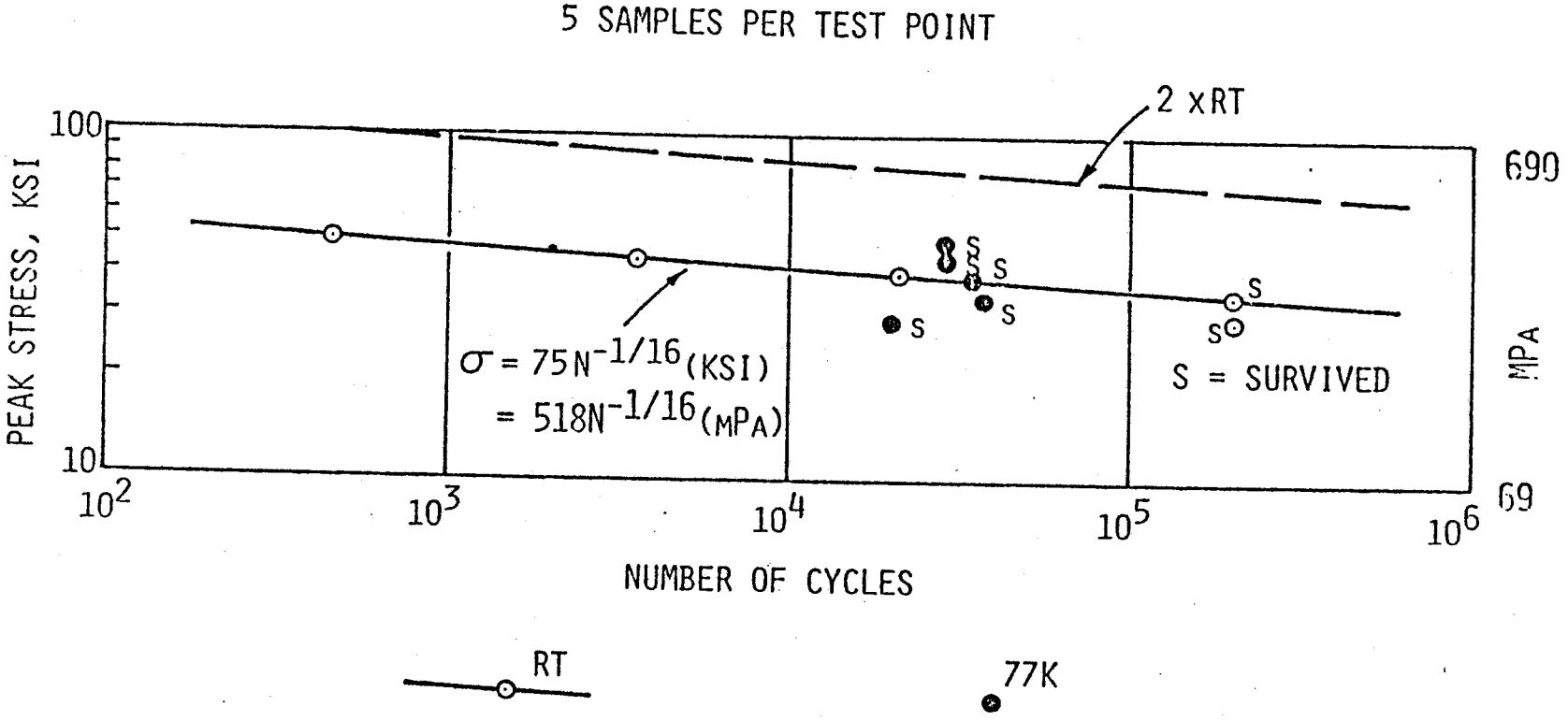

FIGURE 6.2 IRRADIATED G-10 COMPRESSION FATIGUE TEST DATA

7.1 REMOTELY CONTROLLED MAINTENANCE (RCM)

Introduction

The need for RCM has prompted the choice of several features in the magnet, such as the decision to avoid girth rings at the outer boundaries. Beyond these choices, however, no effort was devoted to design of details for ease of RCM. However, it will be an integral aspect of the detail design phase since experience has shown that after the fact design of RCM features can result in an almost unworkable system.

A brief discussion is presented to highlight some of the foreseen maintenance problems and to reveal how RCM has been borne in mind in developing the current design.

Maintenance Problems and Solutions

For estimating purposes, the magnet was assumed to be a solid copper cylinder 5.37 m in diameter and 3.7 m high. The weight would be approximately 1600 metric tons (MT) or 100 MT per module but this is somewhat overestimated. It has been assumed that the modularization of the TF magnet would allow a 100 Tonne module to be removed complete with its blanket shield and vacuum chamber. Figure 7.1 shows a top view of the machine with one of its modules removed. The separation of adjacent modules would involve the cutting of the external weld between two pairs of closure flanges and the circumferential expansion of the remaining 15 modules by approximately 10 mm in order to free the keys interleaved between the two flanges.

Because there are no girth rings, extraction of the module is now impeded only by the EF1 and OH7 poloidal coils, by connections to the port, if any, and by cooling and other service connections to the TF coil. The poloidal coils must be raised (or lowered, depending on the position of the coils) to clear the cooling

manifolds on top and on the bottom of the TF coils. The poloidal coils are linked together (see Section 3) and the larger coil, EF1, is clamped in position to extensions of the steel TF reinforcement plates. The forces tending to drive those poloidal coils toward the equatorial plane and to deflect them radially are taken by the TF coil. This allows a relatively simple mechanism much as a toggle, to hold them in position. For purposes of RCM, the toggle is greatly preferred over the nut and bolt. However, the EF1 coil serves other purposes which require different methods of fixing. Some of the vertical force on the copper conductor around the port is taken by the EF1 coil. For those occasions when the TF is active and the EF inactive, clamps must be placed from the top EF1 coil to the bottom EF1 coil to provide the necessary reaction.

During assembly of a module there is no inherent structural mechanism to constrain it to a compact circumferential shape. It is envisaged therefore, that B stage epoxy will be used during assembly to bond components together to achieve such compaction. The components of a module are clamped in a $22\frac{1}{2}^{\circ}$ fixture under high circumferential pressure while the B stage resin is cured at about 100C. During operation of the TF coil under irradiation, deterioration of this resin bond will progress from regions closest to the blanket outwards toward the outside of the coil. However, it is expected that sufficient bond strength will be retained so that, even at full life of the TF coil, a module being removed from it will be held together against the relatively small forces trying to separate the component plates and sheets.

After removal of a module from the TF coil, further disassembly, should it be necessary, is carried out in a hot cell adjacent to the reactor hall. This further assembly could consist of the following operations:

(1) Cutting the weld between the inside edge of a closure flange and the vacuum vessel or shield assembly. This will expose the face of the shield modules to allow them to be removed.

(2) Removal of shield modules (other than test modules) which must be in the form of toroidal prisms of

length equal to a half module is performed by withdrawing the unit in a circumferential direction after disconnection of coolant and other services. Cooling connections to the shield modules would be through steel reinforcement or through the port openings. In the former case the connections would be close to the closure flange so that they could be accessed immediately after the closure flange is removed. If the latter arrangement is applied, then connections would be at the top or bottom of the ports so as to leave ample height for test modules or plasma access.

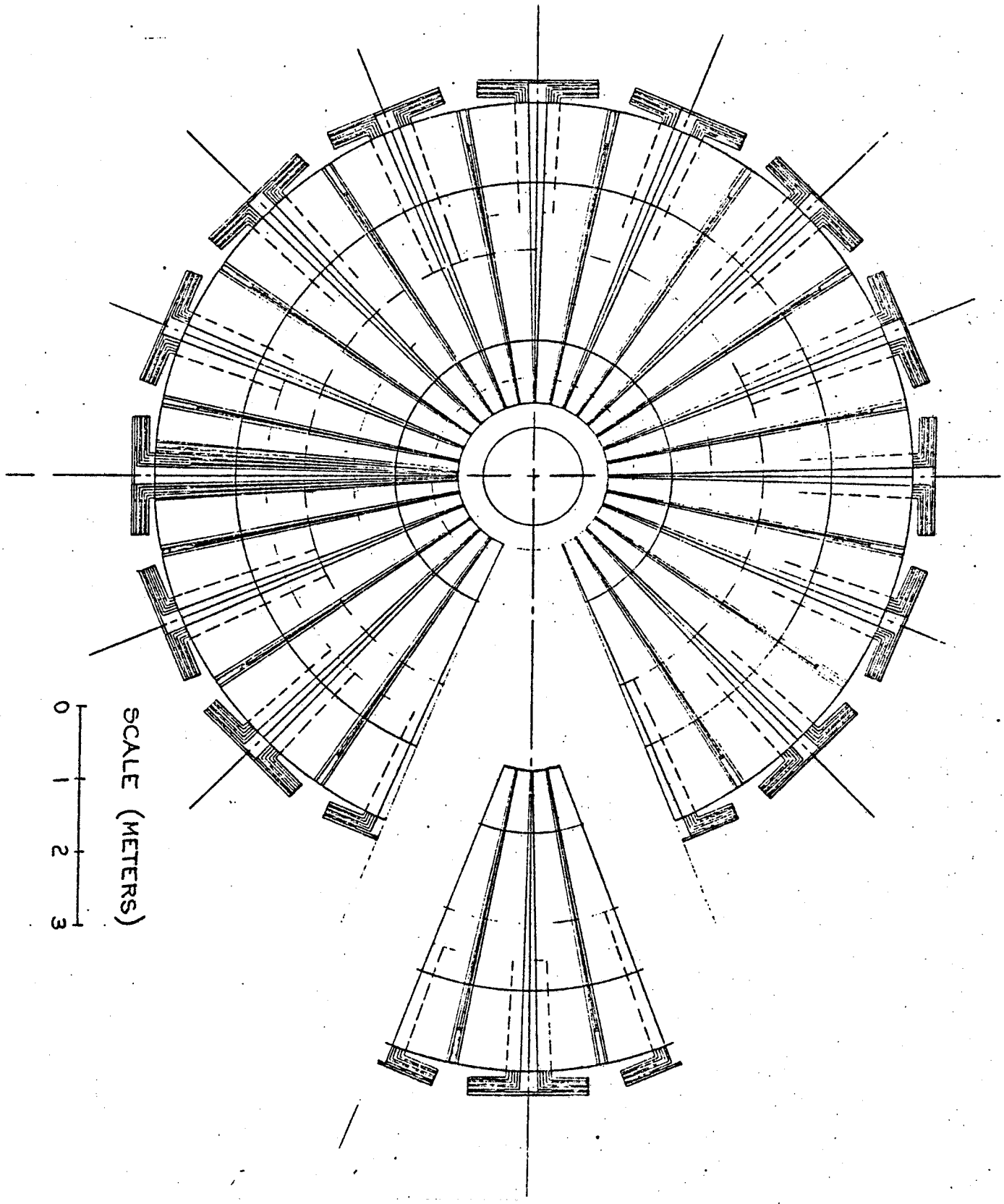

Figure 7.1 Top View of FED-R2 with Separated Module

APPENDIX A

Elongation Tradeoffs

In this appendix, the effect of plasma elongation is considered. It is varied by holding the engineering of the magnet constant and allowing the neutron wall loading to vary. This is done to study whether, in a resistive coil reactor, a larger near-circular plasma would be more advantageous than a smaller, elongated plasma. After this is completed, two versions (one with b/a = 1.5 and the other with b/a = 1.2) with similar plasma physics, engineering and wall loading are compared side by side.

Elongation has the following consequences on the machine engineering:

- Increases stresses in the throat because of increased tensile loads and increased bending
- Increases the resistive power
- Increases the stored energy in the EF system
- Increases the requirements for the OH transformer
- Increases the complication in the poloidal and toroidal field system because of the presence of the shaping coils
- Requires more complex plasma positioning control system because of the vertical instability.

On the other hand, elongation allows reduction of plasma requirements, because of the increase in β_T with elongation. It also increases wall area and volume resulting in an increase in fusion power. Simultaneous increase in plasma beta (β_T) and wall loading result in a net (but relatively small) increase in wall loading.

These tradeoffs are analyzed in this appendix. It is assumed that the scaling of β_T with elongation is

$$\beta_T \sim \kappa$$

where $\kappa = b/a$.

Because the peak stresses in the toroidal field coil and in the OH coil are large, it has been decided to keep the von Mises stresses in the throat of the magnet and in the OH system constant. As elongation requires large ohmic drive due to large LI and resistive drive, it is important in these calculations to keep the OH stresses constant and as large as possible (see section 3.4). (Decreased OH requirements result in larger available cross sectional area for the TF coil, and therefore, larger peak field operation). The stresses are calculated by the method of toroidal shells used in section 5. The simplified calculation used for the constant elongation used in the parameters in section 2 is not accurate because it ignores the horizontal forces that result in toroidal moments.

Table A.1 shows the main machine parameters as the plasma elongation is reduced for fixed a and R. The magnetic field increases slowly with decreasing elongation but not fast enough to balance the reduction in plasma β_T. The magnetic field is allowed to increase with decreasing elongation because of reduced tensile load in the throat, increased throat area due to reduced OH inductive requirements and decreased bending in the throat. Table A.1 is derived assuming that the stresses in the OH system are constant,that the stresses in the throat of the TF coil are constant (calculated in the same way as is done in section 5) and that the plasma major and minor radii are fixed. The wall loading has not decreased as fast as the margin of ignition MI due to the fact that the wall area is decreasing with decreasing elongation. The most noticeable effect of decreased elongation is in the energy stored in the magnet, that increases from 3.6 GJ for $\kappa = 1.5$ to 4.5 GJ for $\kappa = 1$. Also shown in Talbe A.1 are the dimensions of the TF plate.

The greatest advantage of decreased elongation is the reduction in the complexity of the vertical field system. The properties of the vertical field system are shown in Table A.2. An elongation of $\kappa \approx 1.2$ is approximately the optimum, because in this case there is no need for shaping coils. (Shaping coils are required for circular plasmas with high β_T.) The energy in the EF coils, the resistive power, the A-turns all decrease significantly as the elongation decreases from $\kappa = 1.5$ to $\kappa = 1.2$, but more slowly as the elongation is decreased further. Note that the current in the shaping coil, I_2, is small for the case $\kappa = 1.2$. These advantages in the vertical field systems are achieved with a small loss in wall loading and decreased margin of ignition MI (shown in Table A.1).

The loss in wall loading and margin of ignition MI can be compensated by increasing the machine size. Table A.3 shows the main parameters of the base case of FED-R2 with elongation of 1.5 and that of a machine with close to natural elongation of 1.2. Note that in this case, the stored energy and the resistive power of the machine have significantly increased in the case of $\kappa = 1.2$ vs the case of $\kappa = 1.5$. More surprisingly, the shear stresses in the outer leg of the magnet that resist the torsion have increased with decreased elongation. This latter effect is due to the increase in the field to allow simultaneous increases in MI and P_{wall} so that these values are equal to those for $\kappa = 1.5$.

Table A.4 shows the main parameters of the equilibrium field system of the designs of Table A.3. The reduction in the resistive power of the EF system balances partially the increases in the TF coil. The machines have the same neutron wall loadings, same margin of ignition and the same von Mises stresses in the throat of the magnet and in the ohmic heating transformer.

Figure A.1 schematically shows the machine designs described in Table A.3 with the corresponding equilibrium field coils. Although the machine design with $b/a = 1.2$ is somewhat larger, the advantages obtained

with the decreased elongation should be considered. If the problem of controlling the vertical position of the plasma is of concern, then the attractiveness of relatively small elongation is enhanced. Also, if the increase in toroidal beta (β_T) with elongation does not occur, then the near circular plasmas are definitely more attractive than the elongated plasmas for FED-R2.

TABLE A.1

TF Coil for Designs with Varying Elongation

for Fixed a and R

$\kappa = b/a$	1.5	1.2	1.0
MI	1.83	1.48	1.28
A	4.19	4.19	4.19
B (T)	7.16	7.60	8.03
I (MA)	4.57	3.75	3.21
P_{wall} (MW/m^2)	4.0	2.90	2.29
P_f (GW)	0.40	0.26	0.18
W_{TF} (ktonnes)	1.48	1.42	1.39
E_{TF} (GJ)	3.6	3.9	4.47
P_{TF} (MW)	227.	237.	247.
τ (MPa)	23.8	23.1	22.5
plate sizes (m^2)	4.35×3.47	4.4×3.15	4.48×2.97

TABLE A.2

EF Coil for Designs with Varying Elongation

for Fixed a and R

E_{EF} (MJ)	309.18	124.62	105.05
P_{EF} (MW)	76.23	35.75	40.58
W_{EF} (tonnes)	171.57	102.88	94.50
MA_{EF} (MA- turns)	12.23	5.16	6.45
I_1 (MA)	2.92	2.08	1.62
I_2 (MA)	-3.18	-0.49	1.60
R_1 (m)	5.14	5.22	5.27
R_2 (m)	1.94	1.80	1.87
z_1 (m)	1.30	1.06	0.91
z_2 (m)	2.06	1.76	1.74
j_1 (MA/m^2)	10.0	10.0	10.0
j_2 (MA/m^2)	15.0	15.0	15.0

TABLE A.3

TF Coil for $P_{wall} = 4$ MW/m^2

and $MI \sim 1.9$

MI	1.83	1.88
P_{wall} (MW/m^2)	4.0	4.0
$\kappa = b/a$	1.5	1.2
A	4.19	4.66
R (m)	2.64	2.7
a (m)	0.63	0.58
B (T)	7.16	8.86
I (MA)	4.57	3.59
P_f (GW)	0.402	0.339
W_{TF} (ktonnes)	1.48	1.46
E_{TF} (GJ)	3.6	5.7
P_{TF} (MW)	227.	297.
τ (MPa)	23.8	31.7
plate sizes (m^2)	4.35 $\times$ 3.47	4.4 $\times$ 3.15

TABLE A.4

EF Coil for $P_{wall} = 4\ \mathrm{MW/m^2}$

and $MI \sim 1.9$

I_1 (MA)	2.93	2.29
I_2 (MA)	-3.19	-0.544
R_1 (m)	5.14	5.27
R_2 (m)	1.94	1.92
z_1 (m)	1.31	1.02
z_2 (m)	2.07	1.77
j_1 (MA/m^2)	10.0	10.0
j_2 (MA/m^2)	15.0	15.0
E_{EF} (MJ)	309.	152.
P_{EF} (MW)	76.2	39.9
W_{EF} (tonnes)	172.	114.
MA_{EF} (MA turns)	12.2	5.66

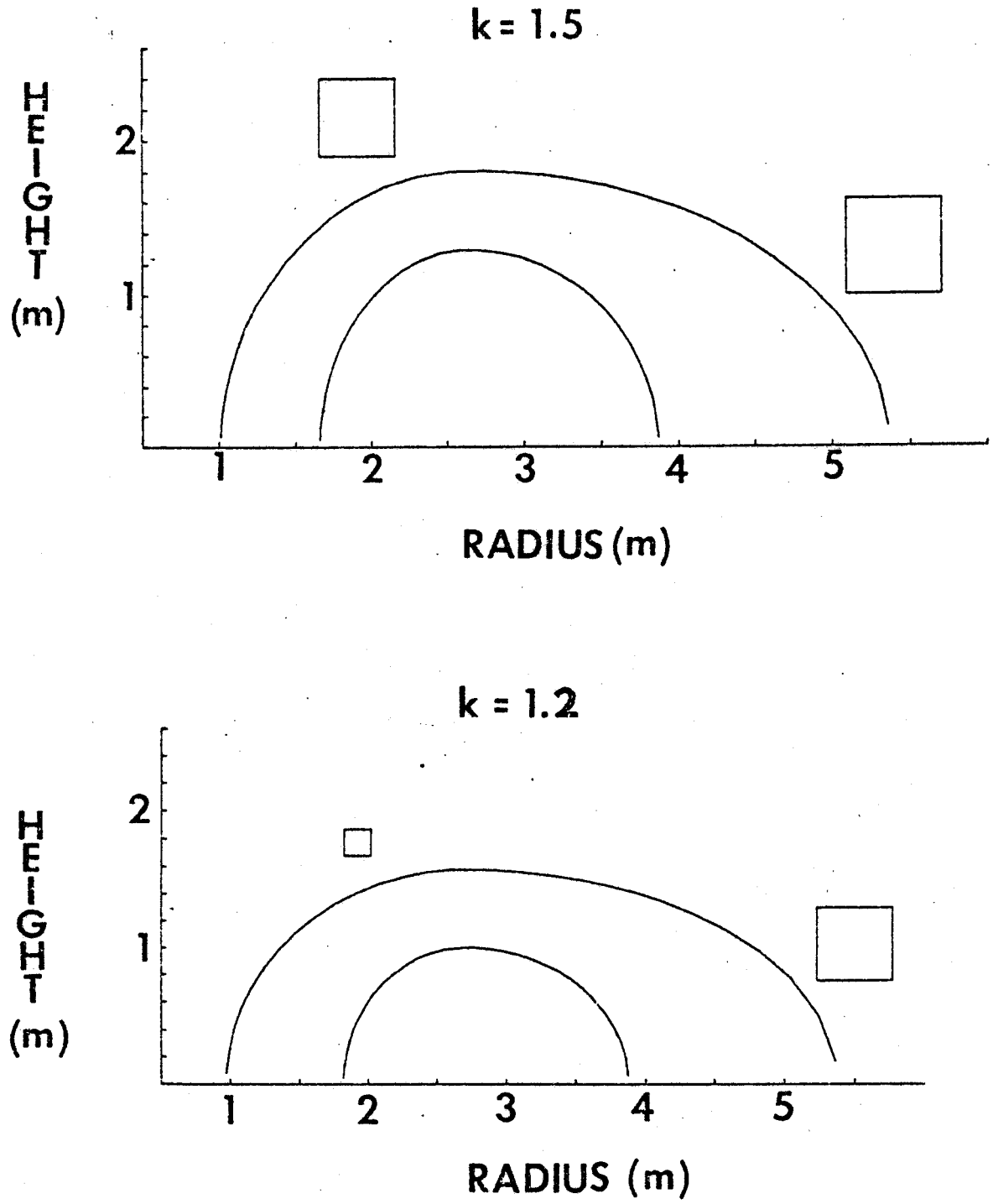

Figure A.1 Schematic Countours of the Toroidal Field Coils and their Respective Equilibrium Field Systems for $\kappa = 1.2$ and $\kappa = 1.5$.

APPENDIX B

Heating of the Plasma

In this section, heating of the plasma is discussed. The preferred method of heating is ICRF at the second harmonic. In this section, special attention is given to the diverse plasma scenario in the two cases of operation. The same sources can be utilized if in the high performance case, tritium is heated at $2\omega_{ct}$, while deuterium is heated in the base case at $2\omega_{cd}$.

A 1-D slab model with a full-wave treatment is first used to determine the spatial behavior of ICRF and the importance of mode conversion. Then a 1-D cylindrical model using a WKB treatment is incorporated into a time-dependent fluid code to determine the amount of RF power needed. Both models assume a local RF dispersion relation. The full 3 X 3 hot plasma dispersion tensor is used to determine complex $k_\perp$ given real ω and $k_\parallel$ (fixed in radius) for both the fast magnetosonic and Ion Bernstein waves.

In the time-independent 1-D slab model the plasma is divided into many (up to 10,000) thin, uniform slabs lying in the yz plane with B_o in the z direction. The local dispersion relation is solved in each slab for four modes, a fast wave ($\pm k_{\parallel F}$) and an Ion Bernstein wave ($\pm k_{\parallel I.B.}$) which propagate in both directions. In each slab the RF wave field is the linear combination of the individual mode fields,

$$E = \sum_{i=1}^{4} E_m e^{ik_{\parallel m} r}, \quad B = \mu_{i=1}^{4} B_m e_{\parallel m}^{ik} r \tag{1}$$

The amplitude coefficients E_m and B_m are calculated from the total tangential E and B fields, which are continuous across a slab interface. The boundary conditions for the two plasma edge slabs are determined by the launching conditions. For FED-R2, we assumed that a fast wave is launched from the low field side. To find

the electric and magnetic fields, a large (4800 $\times$ 4800 for 1200 slabs) set of complex equations is numerically solved using a band matrix solver. For accurate solutions $k_{\|}\Delta x << 1$, where Δx is the slab width. Since $k_{\perp}$ for the Ion Bernstein wave becomes large near the plasma edge, only the central 100 cm of plasma width ($0 \leq r \leq 50$ cm) is used in the analysis. We have not examined the antenna-plasma coupling problem yet. However, our region of analysis is wide enough to contain all of the ion and most of the electron heating zones.

After solving for the E and B fields, we can calculate the total radial Poynting flux

$$P = \frac{-c}{8\pi} Re(E \times H^*) \tag{2}$$

The change in P from the low to high field side gives an estimate of the amount of RF power absorbed per radial pass.

To calculate the amount of RF power absorbed by each species, we use the weak damping formula

$$P^s_{RF} = \omega E^* \cdot \left(\sum_m k^A_{m,s} \cdot E_m\right). \tag{3}$$

where K^A is the anti-hermitian part of the dielectric tensor, m the mode, and s the species.

In Table B.1 we list the assumed FED-R2 parameters assumed for the calculations.

Table B.2 shows preliminary results of heating in FED-R2 with ICRF in both operating cases. In the base case using primarily second harmonic deuterium heating (f = 77 MHz) the single pass absorption is about $\approx$ 100%. Less than half of the energy is absorbed in the high performance case with 2- harmonic heating of tritium (f = 77 MHz). It may be desirable to tune the frequency of the radiation so that in both the base case and the high performance case the deuterium is heated at twice its gyrofrequency. However, this may entail problems with the launching structure (either antennas or waveguides), in which case tritium heating, though it

has less damping per pass than deuterium heating, may be preferred.

Figure B.1 shows the RF dispersion relation for both the fast and Ion Bernstein waves when $f = 77$ MHz with parabolic squared density and temperature profiles ($T_{io} = 11keV, T_{es} = 9keV$). At the time the RF is turned off the hotter plasma temperatures produce nearly 100% absorption in one radial pass.

Figure B.2 and B.3 show the power deposition profiles on the ions (deuterium) and electrons for the base case operation. The deposition profiles are peaked on axis. Figure B.4 shows the Poynting flux. Note that about all the power has been absorbed in a single pass.

The temperatures are such that these figures corresponds to the maximum in the required heating.

Figure B.5 shows the heating contours of constant power required to keep $d\beta_T/dt = 0.3\%/S$ as a function of the product na and the plasma β_T. The profiles shown in Figures B.2 and B.3 were assumed. Note that $\approx$ 13 MW of heating is all that is required. This is because of the strong peak absorption of the incident power.

Our 1-D slab calculations show that mode conversion does not seem to play an important role. Over 98% of the total RF heating results from the incident fast wave. In addition, since the fast wave wavelength is large compared to the scale length of plasma parameter changes, a WKB treatment of fast wave heating should be accurate.

We conclude that for a 50–50 D-T FED-R2 plasma, 20 MW of ICRF power for 500 ms with f ~ 77 MHz (corresponding to second harmonic deuterium and third harmonic tritium heating) would be needed, assuming Alcator scaling. The absorption is peaked toward the center with the ions receiving more than 75% of the incident power. The absorption is quite strong with more than 94% of the incident fast wave power absorbed in one radial pass at the high temperature. Mode conversion should not play a significant role. Over 98% of the RF heating comes from the incident fast wave launched from the low field side.

TABLE B.1

FED Parameters Assumed for ICRF Calculations

R_o(cm)	244
a(cm)	63
$n_D(0) = n_T(0)$(cm)	4×10^{14}
n_D(edge) = n_T(edge)(cm)	1×10^{13}
B_o(kG)	5.1 — 7.1
RF Parameters	
$\bar{P}_{RF}$(MW)	20
$k_{\|\|}$(cm^{-1})	0.3
Frequency (MHz)	72-77

TABLE B.2

B_T	5.1			7.2
f (MHz)	77			72
ion heated	D			T
T_{io}	6	11	17	11
T_{eo}	5	9	15	9
% of energy to ion	79	76	73	50
% of energy to electrons	20	22	24	50
single-pass absorption	90	~100	~100	35
mode of heating	$2\omega_{cD}$	$2\omega_{cD}$	$2\omega_{cD}$	$2\omega_{cT}$

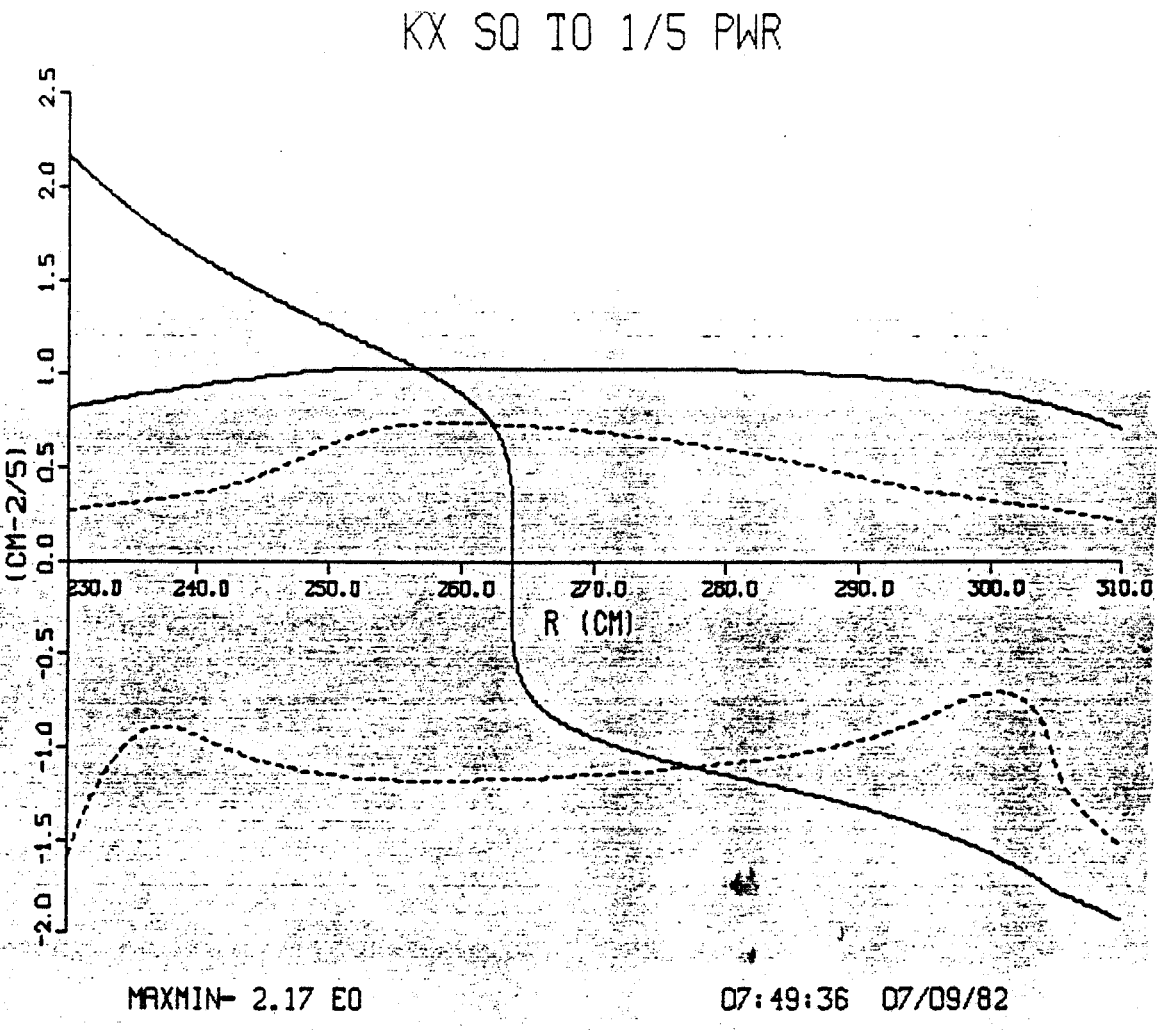

Figure B.1 Dispersion Relation for the Fast and Ion Bernstein Waves for $f = 77$ MHz

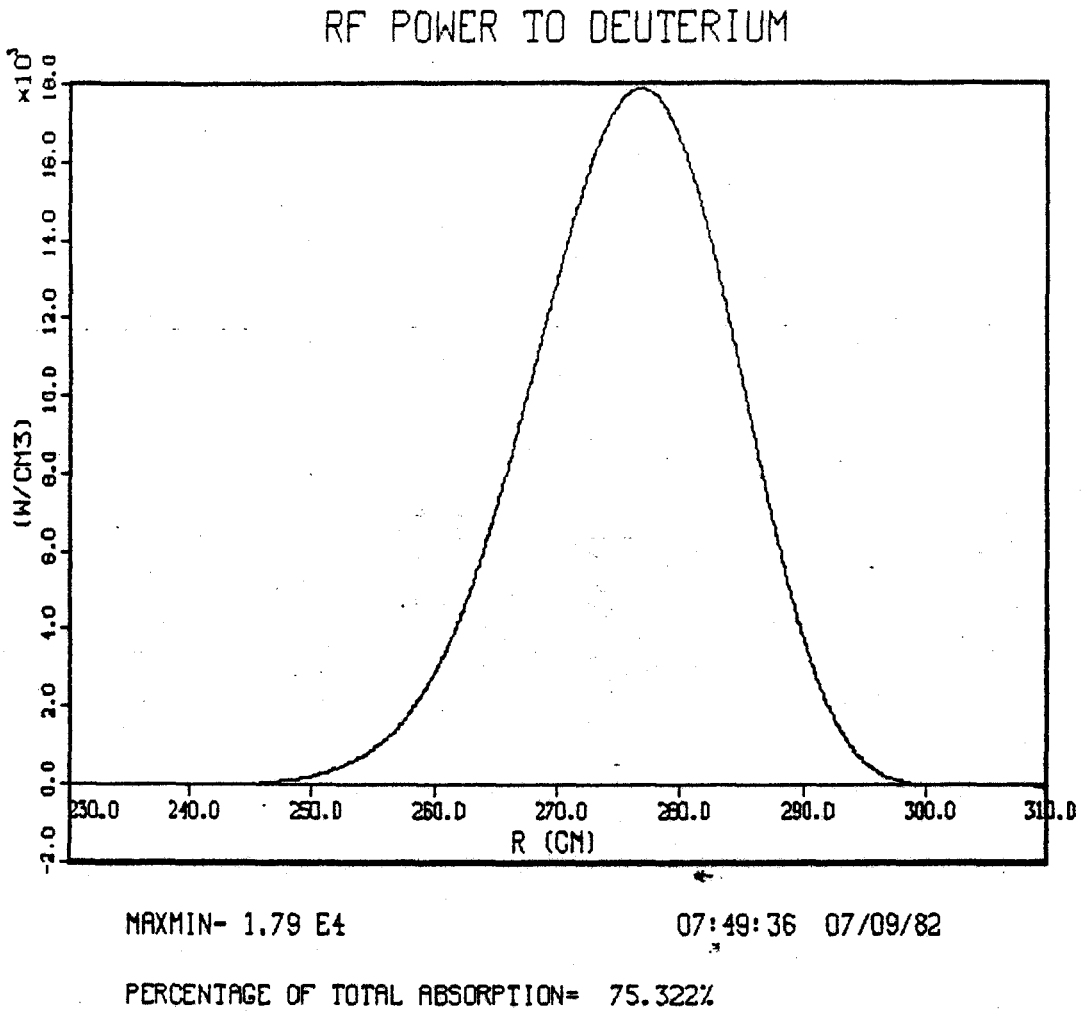

Figure B.2 RF Power to Deuterium for Base Case Operation

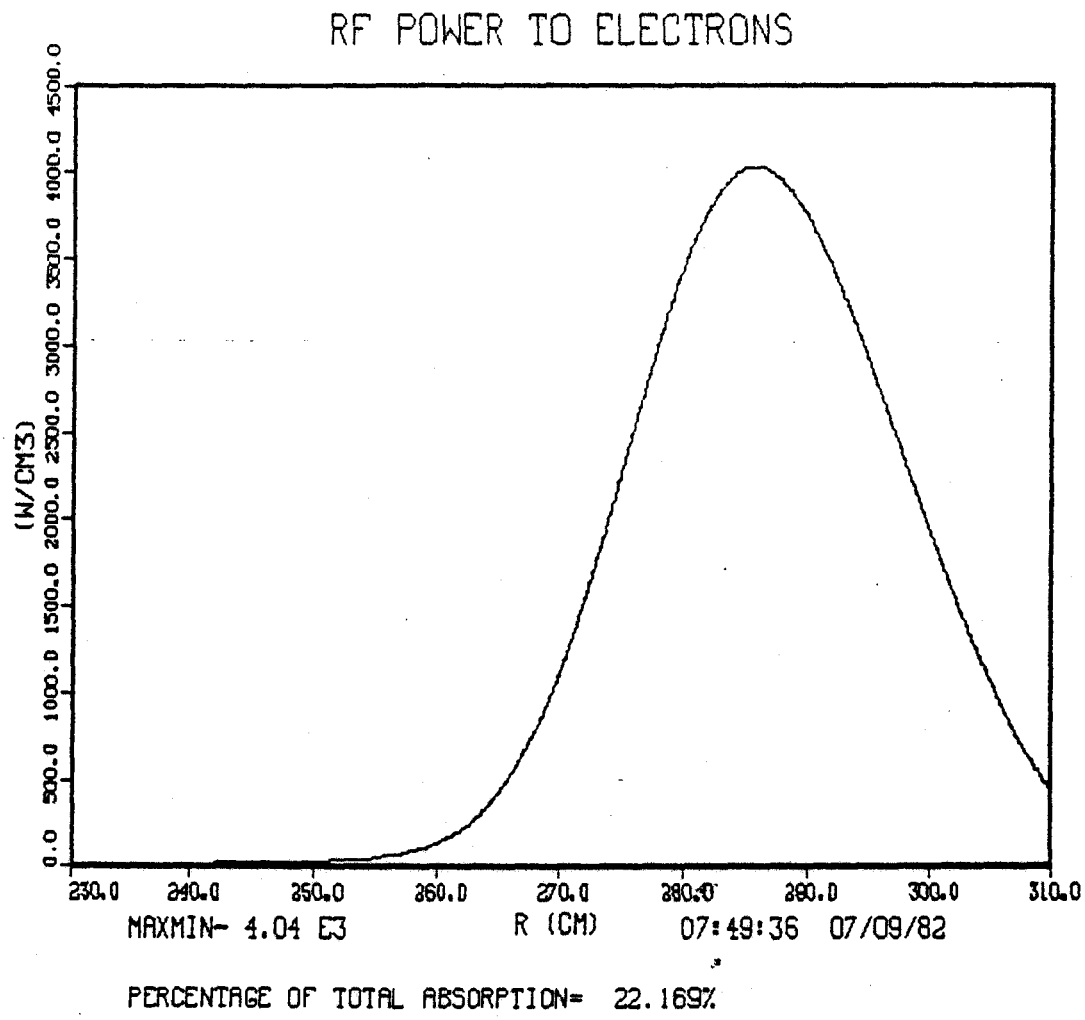

Figure B.3 RF Power to Electrons for Base Case Operation

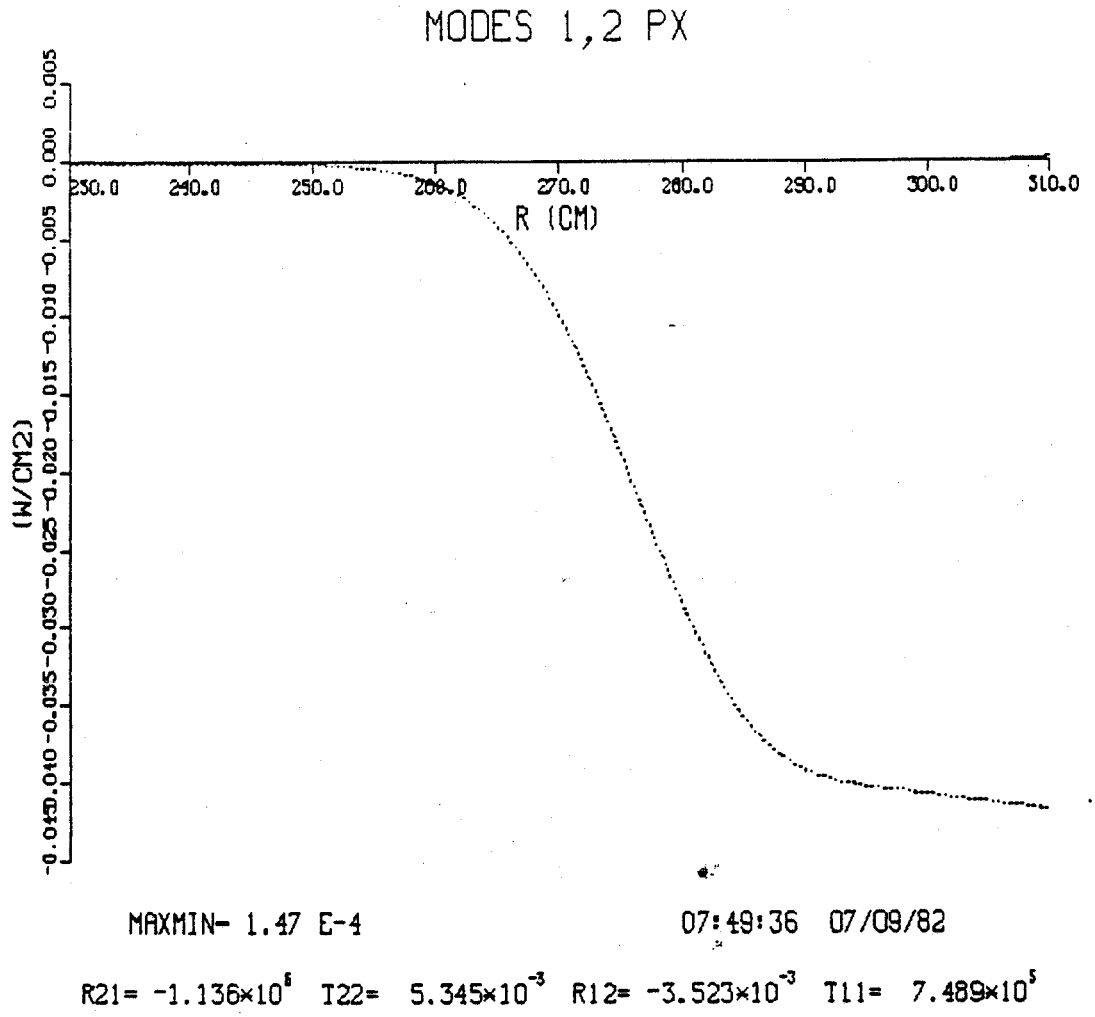

Figure B.4 Poynting Flux for Base Case Operation

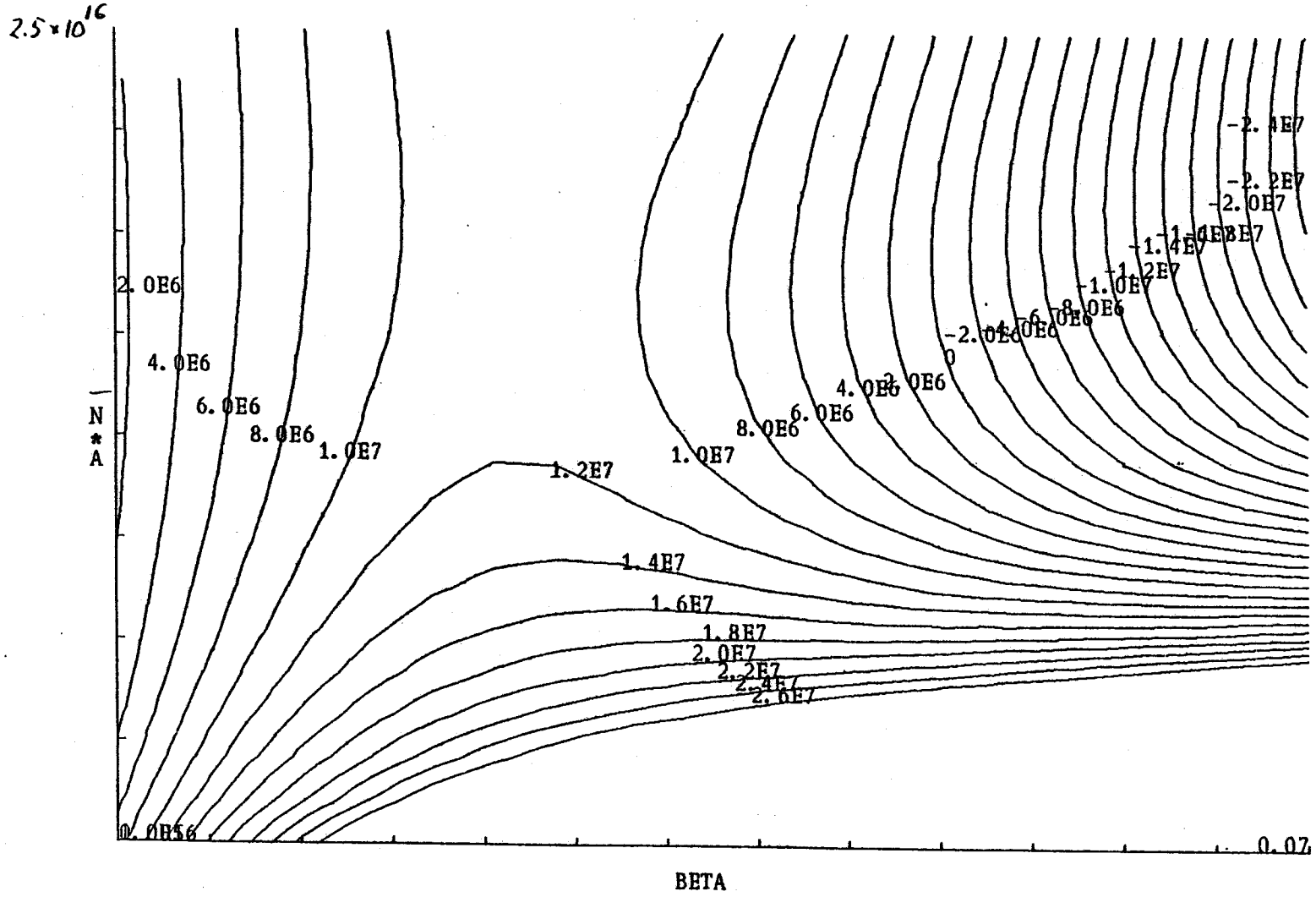

Figure B.5 Contours of Constant RF Power Required to Maintain $d\beta/dt = .3\%/s$ vs na and β

APPENDIX C

COST OF THE MACHINE

In this Appendix, the cost of the machine is discussed. Two methods have been used to derive an approximate figure to the cost. The first one uses the costing routine used by the Fusion Design Center, which adds the cost of the components [1,2]. The second cost is derived by extrapolating from TFTR costs [3]. As the machine has resistive coil magnets and has main dimensions close to those of TFTR, this is a valid method.

The study presented in this report concentrated on the magnetics aspects of the machine. The toroidal field system was given the largest attention, with some work also being performed for the poloidal field systems (OH and EF systems). There are other systems that affect the overall feasability of the machine design, such as the pumping scheme (limiter pumping), heating structures (antennas or waveguides for launching the RF), first wall design (cooling, effects of disruptions). The requirements that these systems impose upon the magnet and main concept can not be completely determined until appropriate design studies are performed. However, the main concept would probably not be very much affected by them, although the main envelope of the machine might have to be increased.

With this caveat in mind, Table C.1 shows the cost of the machine as determined by the code of the Fusion Engineering Design Center [1]. There are numbers that are scaled directly from the FED design [2], such as the pumping systems, the first wall and the I & C (Instrumentation and Control). The total direct cost of the machine amounts to ~ 469 M. Table C.2 shows the cost of the respective systems for the baseline FED [2]. It is seen that the total direct cost is reduced by a factor of about 2.2 from that of the baseline FED design. Large reductions in cost are possible in the magnet system (due to the much smaller tokamak and to the use of copper

coils), in the heating systems (due to the smaller major radius of the machine) and in the facilities (due to the smaller nuclear island and to the modularization scheme, which decreases the cost of the hot cell).

Table C.3 shows the approximate cost for TFTR. Shown are hardware outlays from 1976 through 1982. Not included are EDIA. The total direct cost of TFTR is 235M. FED-R2 and TFTR are of similar size. The weight of the FED-R2 magnet is larger than TFTR, but the coils are easier to manufacture. The 54M estimate from Table C.1 was scaled from Alcator C cost by scaling by the weight ratio. Most of the items in Table C.1 scale from Table C.3 due to larger requirements and/or goals. The cooling system, the torus, the electrical system and the plasma heating scale from TFTR by about a factor of 2 due to larger requirements. As the buildings requirements are the same (due to similar sizes), the facilities (buildings) are about the same. The larger cost in FED-R2 may be due to increased requirements due to remote handling (costs for remote handling are included under "remote maintenance"). Because of different requirements, the costs of the remote maintenance equipment and tritium systems cannot be scaled from TFTR, and the numbers obtained from the Fusion Engineering Design Center cost code have been used.

The largest gap in cost appears in the Instrumentation and Control and Diagnostics. It is 67M in Table C.1 vs. 43M for TFTR. The requirements of I&C for TFTR and FED-R2 are similar, and the large discrepancy in cost of the I&C and diagnostics systems can not be explained by the large additional use of tritium in FED-R2.

Table C.4 shows a revised cost analysis for FED-R2 with the Instrumentation and Control System used for TFTR. The cost of the remote maintenance and the cost of the facilities have been estimated by PPPL [4] for a machine (LITE) similar to FED-R2. The total direct cost is 385M. The cost of FED-R2 is, then, less than twice that of TFTR. It should be stressed that although the costs of TFTR are well determined, the cost of the different systems (or the scaling of the cost from the TFTR cost) for FED-R2 are not as well determined.

References

[1] REID, L., Fusion Engineering Desing Center, Oak Ridge, private communication

[2] FLANAGAN, C.A., STEINER, D., SMITH, G.E. and Fusion Engineering Design Center Staff, ORNL/TM-7948

[3] Princeton Univertsity Plasma Physics Laboratory, "Tokamak Fusion Test Reactor Cost/Schedule Performance Report Through May 1982", May 1982

[4] STEWARD, L., Princeton Plasma Physics Laboratory, private communication

Table C.1

Direct Costs for FED-R-2

(Fusion Engineering Design Center Costing Routine)

Magnet system	54
Torus	16
Cooling System	20
Tritium and Fuel Handling	46
Plasma Heating (RF)(30MW)	50
Electrical Systems	67
Vacuum Pumping	1
Instrumentation and Control†	67
Remote Maintenance and Equipment	60
Facilities	88
Total Direct Cost	469

† Includes Diagnostics

Table C.2

Direct Costs for Baseline FED

FEDC Costing Routine

Magnet System	312
Torus	162
Cooling Systems	38
Tritium and Fuel Handling	54
Plasma Heating (RF) (50MW)	89
Electrical Systems	99
Vacuum Pumping	24
Instrumentation and Control†	67
Remote Maintenance and Equipment	60
Facilities	139
Total Direct Cost	1044

† Includes Diagnostics

Table C.3

Direct Costs for TFTR

Magnet System and Structure	46
Torus	11
Cooling Systems	5
Tritium and Fuel Handling	5
RF Systems	≈ 0
Neutral Beam Systems	24
Electrical Systems	32
Vacuum Pumping	2
Instrumentation and Control	25
Diagnostics	18
Remote Maintenance and Equipment	1
Facility Construction	66
Total	235

Table C.4

Cost Estimate for FED-R2 Scaled from TFTR

Magnet System and Structure	54[a]
Torus	16[b]
Cooling System	20[b]
Tritium and Fuel Handling	46[b]
Plasma Heating (30MW)	50[b]
Electrical Systems	67[b]
Vacuum Pumping	1[b]
Instrumentation and Control	25[c]
Diagnostics	18[c]
Remote Maintenance Equipment	28[d]
Facilities	57[d]
Total	382

[a] Based on weight scaling from Alcator

[b] From Table C.I

[c] From Table C.3

[d] From Calculations for LITE performed by PPPL using TFTR costs as a base.